National Library
of Canada

Acquisitions and
Bibliographic Services Branch

395 Wellington Street
Ottawa, Ontario
K1A 0N4

Bibliothèque nationale
du Canada

Direction des acquisitions et
des services bibliographiques

395, rue Wellington
Ottawa (Ontario)
K1A 0N4

Your file Votre référence

Our file Notre référence

NOTICE

The quality of this microform is heavily dependent upon the quality of the original thesis submitted for microfilming. Every effort has been made to ensure the highest quality of reproduction possible.

If pages are missing, contact the university which granted the degree.

Some pages may have indistinct print especially if the original pages were typed with a poor typewriter ribbon or if the university sent us an inferior photocopy.

Reproduction in full or in part of this microform is governed by the Canadian Copyright Act, R.S.C. 1970, c. C-30, and subsequent amendments.

AVIS

La qualité de cette microforme dépend grandement de la qualité de la thèse soumise au microfilmage. Nous avons tout fait pour assurer une qualité supérieure de reproduction.

S'il manque des pages, veuillez communiquer avec l'université qui a conféré le grade.

La qualité d'impression de certaines pages peut laisser à désirer, surtout si les pages originales ont été dactylographiées à l'aide d'un ruban usé ou si l'université nous a fait parvenir une photocopie de qualité inférieure.

La reproduction, même partielle, de cette microforme est soumise à la Loi canadienne sur le droit d'auteur, SRC 1970, c. C-30, et ses amendements subséquents.

Canada

VISCOELASTIC FLOWS AROUND SPHERES

by

Hailemariam Atsbha
B.A.Sc. Chemical Engineering

A Thesis
Submitted to the School of Graduate Studies
in Partial Fulfilment of the Requirements for
the Degree of Master of Applied Science

in

Chemical Engineering
University of Ottawa

ISBN 0-315-82587-1

UNIVERSITÉ D'OTTAWA
UNIVERSITY OF OTTAWA

Abstract

The present thesis is concerned with the flow of viscoelastic liquids in channels and around spheres contained in cylinders. A general-purpose program based on the finite element method has been used that solves for the conservation equations in two-dimensional planar and axisymmetric geometries. The constitutive models include the Newtonian fluid and integral viscoelastic models, such as the Maxwell and Oldroyd-B, based on the theory of linear viscoelasticity, as well as a highly non-linear K-BKZ model. The latter is able to correctly predict such fundamental properties of polymeric liquids as shear and elongational viscosities and normal stresses measured in shear flows.

Problems that have been tackled are the Poiseuille flow between parallel plates and in tubes, where all models give excellent results checked against analytical solutions for a range of elasticity levels determined by a dimensionless Weissenberg number (Ws). Then the benchmark problem of flow around a sphere contained in a tube with a 2:1 diameter ratio is tackled using the Newtonian and integral Maxwell models. Results were obtained up to a limiting Weissenberg number Ws=0.3, beyond which no convergence could be achieved. The drag coefficient on the sphere shows a monotonic decrease with increasing Ws, from 5.9522 for Ws=0 to 5.4935 for Ws=0.3. These results are in good agreement with previous ones published in the literature. Non-zero second normal stress differences decrease the drag even further. This is a novel finding not reported earlier.

The unbounded flow around spheres was simulated using a 50:1 diameter

ratio. The K-BKZ integral model was used, which fitted experimental data for shear and elongational viscosities and normal stresses for a model polymer solution known as M1 (polyisobutylene in polybutene). The simulations converged for values of Ws up to 0.3 and gave an almost constant drag coefficient (K), close to the Newtonian value of 1.0626, which is in agreement with previous experiments reported in the literature for low Ws numbers (Ws<0.1). However, in the range around Ws=0.3, the experimental drag goes through a minimum of 0.95 and then it increases rapidly to reach values of 1.35 at Ws=1.4. Numerical simulations for high Ws numbers based on the Newtonian flow field also showed a minimum followed by a rapid increase of the drag coefficient with Ws, but they produced higher values (up to 18 %) than the experimental ones. These findings suggest that slip on the sphere surface may be occurring at moderate to high Ws numbers, which has the effect of lowering the drag calculated on the sphere.

Acknowledgements

In presenting this thesis, I wish to express my sincere appreciation to Dr. E. Mitsoulis, my supervisor, for his constant guidance, inspiration and encouragement throughout the course of this study. I also wish to thank Dr. Dionissios G. Kiriakidis for his constant encouragement and assistance in many ways. To G. Barakos is due my appreciation for many valuable discussions.

Furthermore, I am greatful to the Department of Chemical Engineering, University of Ottawa, for the financial support in the form of assistanship.

Finally, I owe my gratitude to my parents and family for their constant encouragement, which was indispensable in completing this study.

Contents

List of Figures

List of Tables

Nomenclature

a	relaxation modulus, Pa
$\bar{\bar{C}}_t$	Cauchy-Green tensor
$\bar{\bar{C}}_t^{-1}$	Finger strain tensor
D	characteristic diameter, m
D_∞	Stokes' drag force, N
e	error
$\{F\}$	global load vector
F_D	drag force on a sphere, N
F_N	normal component of the drag force, N
F_T	tangential component of the drag force, N
g	acceleration due to gravity, m/s^2
H	characteristic height, m
$\bar{\bar{I}}$	identity tensor
$\bar{\bar{I}}_c$	first invariant of the Cauchy-Green tensor
$\bar{\bar{I}}_{c^{-1}}$	first invariant of the inverse Cauchy-Green tensor
$[K]$	global stiffness matrix
L	characteristic length, m
	length, m

L_d	axial distance downstream from the centre of the sphere, m
L_u	axial distance upstream from the centre of the sphere, m
M	linear time-memory function, Pa/s
N	number of relaxation times or relaxation moduli
	number of iterations
	Newtonian
N_1	first normal stress difference, Pa
N_2	second normal stress difference, Pa
o	origin
P	pressure, Pa
P_{cl}	pressure at the centerline, Pa
P_w	pressure at the wall, Pa
r	radial global coordinate, m
	radius, m
	position vector
R	sphere radius, m
R_c	cylinder radius, m
s	magnitude of axial distance from the centre of the sphere, m
	relative time difference, s
t	present time, s
t'	past time relative to the present, s
t_o	characteristic material time, s
T_o	reference temperature, K

$\bar{T}$	surface traction, Pa/m
U	characteristic velocity, m/s
UCM	upper-convected Maxwell
$\bar{u}$	velocity vector normal to the direction of flow at the present state, m/s
$\bar{v}$	velocity vector in direction of flow at the present state, m/s
$\bar{v}$	velocity vector, m/s
$V.E.$	viscoelastic
x	axial global coordinate, m
$\bar{x}$	position vector of the present state, m
$\bar{x}'$	position vector of the past state relative to the present, m
y	transverse global coordinate, m
z	axial global coordinate, m

Greek Letters

α	shear material parameter for the K-BKZ model
β	elongational material parameter for the K-BKZ model
	angle between z-axis and F_D for the integration of the drag force, deg
$\bar{\bar{\dot{\gamma}}}$	rate-of-strain tensor, s^{-1}
$\dot{\gamma}$	shear rate, s^{-1}
$\dot{\gamma}_a$	surface-average shear rate, s^{-1}
ΔP	pressure drop, Pa
$\dot{\epsilon}$	elongational rate, s^{-1}

η_o	zero-shear rate viscosity, $Pa.s$
η_E	elongational viscosity, $Pa.s$
$\bar{\eta}_E$	normalized elongational viscosity
η_S	steady-state shear viscosity, $Pa.s$
$\bar{\eta}_S$	normalized steady-state shear viscosity
θ	azimuthal global coordinate, deg
θ	normal stress ratio τ_{22}/τ_{11}
λ	relaxation time for the Maxwell model, s
λ_1	relaxation time for the Oldroyd-B model, s
λ_2	retardation time for the Oldroyd-B model, s
μ	Newtonian constant viscosity, $Pa.s$
μ_m	molecular contribution to the viscosity, $Pa.s$
μ_s	solvent contribution to the viscosity, $Pa.s$
ρ	density, kgm^{-3}
$\bar{\bar{\tau}}$	extra stress, Pa
τ	shear stress, Pa
τ_{rz}	shear stress, Pa
τ_{xy}	shear stress, Pa
τ_w	shear stress at the wall, Pa
Φ	non-linear strain-memory function, s
χ	position vector
ψ	stream function, m^3/s
Ψ_1	first normal stress coefficient, $Pa.s^2$

Ψ_2	second normal stress coefficient, $Pa.s^2$

Subscripts

a	average
c	cylinder
cl	centerline
d	downstream
D	drag
E	elongational
i	present iteration
ij	components of a tensor
$limit$	limiting value
m	molecular
max	maximum value
min	minimum value
n, N	normal to a surface
r	r-direction
R	ratio
s	solvent
t, T	tangential to a surface
u	upstream
w	wall
x	x-direction
y	y-direction

z	z-direction
θ	θ-direction
∞	unbounded

Superscripts

$'$	past state relative to the present
$^{-1}$	the inverse of a matrix
*	dimensionless quantity

Overscripts

$\bar{}$	characteristic value
	vector
$=$	matrix, tensor
$\dot{}$	rate

Dimensionless Groups

De	Deborah Number = $\lambda\dot{\gamma}_a$ (Eq. 2.32)
K	Drag coefficient = F_D/D_∞ (Eq. 2.37)
P^*	normalized pressure = PR/η_oV (Eq.2.35)
Re	Reynolds Number = ρVD/η_o (Eq. 2.30)
S_R	Recoverable stress ratio = $N_1/2\tau_w$ (Eq. 2.33)
Ws	Weissenberg Number = λV/R (Eq. 2.31)
τ^*	normalized stress = τR/η_oV (Eq.2.35)

Mathematical Symbols

Δ	increment
∂	differential operator
∇	vector differential operator
$\frac{D}{Dt}$	substantial derivative
$\sum_i$	summation over i
$\{\}$	column vector
$[\ ]$	matrix
$\|\ \|$	magnitude
$\|\|\|\|$	norm of a vector
Adj	Adjoint of a matrix
det	determinant of a matrix

Chapter 1

Introduction

1.1 Viscoelastic Material Flow around Spheres

For many years scientists and engineers have considered systems with relatively simple geometry for the application of fluid mechanics. Complex problems are solved only at the expense of considerable effort, usually with the help of high-speed computers.

Many engineering flow problems fall into one of two broad categories: *flow in channels* and *flow around submerged objects* (Bird et al., 1960). Flow in channels includes pumping of oils in pipes, flow of water in open channels, extrusion of plastics through dies, and flow of fluids through filters. Flow around submerged objects includes the motion of air around an airplane wing, motion of fluids around particles undergoing sedimentation, and flow across tube banks in a heat exchanger. In the case of flow in channels, the general concern is obtaining a relationship between the pressure drop and the volume rate of flow. In problems of flow around submerged objects, one generally wants to know the relation between the velocity of the approaching fluid and the drag force. This velocity-drag relationship gives rise to the definition of friction and drag

correction factors.

For unbounded Newtonian creeping flow around submerged objects, the total force acting on the surface is a combination of the buoyant force, form drag and friction drag. The buoyant force arises due to fluid density and the force of gravity. The form drag and friction drag arise due to the viscosity of the fluid and its approaching velocity. These forces are the components of the well-known Stokes law valid at low Reynolds numbers ($Re < 0.1$) (Stokes, 1850; Lamb, 1945). At higher Reynolds numbers, the Stokes law is not valid and the friction factor must be introduced.

The creeping flow of non-Newtonian fluids past spherical particles has received a great deal of attention in recent years. Much of this interest stems from the knowledge that this system is a simplification of many real engineering problems and may provide some insight into some industrial applications. Further interest has been generated by the possibility of measuring the steady shear viscosity by observing the fall of precision spheres through the fluid of interest; the apparatus required is very simple (Bush, 1983). This is easily applied to Newtonian fluids since the theory is well understood. In non-Newtonian cases, the problem is considerably more complicated, and the final analysis depends on the particular model of non-Newtonian behaviour chosen. The ever increasing activities in this area have been best evidenced by the eight international workshops on numerical simulation of viscoelastic flows.

Non-Newtonian behaviour has many facets. Among them are the shear-rate dependence of the shear viscosity, the presence of normal stresses in viscometric

flows, high resistance to elongational deformation giving rise to high elongational viscosity, and memory effects associated with the elasticity of the material (Mitsoulis, 1990). When these fluids are subjected to the flow around spheres, they are expected to behave differently from Newtonian fluids. By computing the drag force on the sphere and comparing it with the Newtonian Stokes drag, one can easily discern the effect of viscoelasticity. Also, by comparing the numerical drag results against experimental results, the particular constitutive equation chosen can be evaluated. The knowledge of the drag force associated with the type of fluid at different elasticity levels is an important step forward towards many engineering applications, especially for polymer solutions as lubricants or friction-enhancing substances.

In the last fifteen years, the rapid development of computers has allowed the numerical solution of many complicated problems with a variety of sophisticated methods such as the numerical method of finite elements (FEM). The main advantages of this method are:

(a) its ability to easily handle complex geometries and boundary conditions;

(b) its flexibility to solve many different types of problems with only slight modifications of the same computer program.

The question of a powerful numerical method seems more or less to have been settled with the application of FEM in flow problems. One shortcoming of the method seems to be its rather involved formulation which requires a good understanding of variational principles, matrix algebra and computer programming skills. However, computer programs can become user-friendly with

appropriate pre-processing of input data and post-processing output data, which greatly simplify the numerical simulations for a series of parametric studies. In that form then, the computer programs can be used by a non-expert on the numerical method itself.

1.2 Review of Numerical Simulation of Viscoelastic Material Flow around Spheres

The numerical simulation of viscoelastic material flows has been the subject of research in recent years especially for polymer solutions and melts. A literature survey of the theoretical studies conducted on the problem of non-Newtonian unbounded fluid flow past a rigid sphere is given by Dairenieh et al. (1985).

Up to a decade ago, most of the reported theoretical studies of the creeping flow of non-Newtonian fluids over a sphere can be classified into: (1) perturbation methods (Leslie, 1961; Caswell et al., 1962; Giesekus, 1963); (2) variational methods (Hill et al., 1956; Astarita, 1977; Cho et al., 1983) and (3) finite difference methods (Adachi et al., 1977). Two basic problems have been considered at length in the literature. Firstly, the effect of elasticity and shear thinning on the drag and, secondly, how the presence of elasticity affects the streamline pattern relative to the Newtonian streamline pattern. Perturbation methods were easily used to solve flows of viscoelastic fluids around spheres in the creeping flow range without significant wall effects. With wall effects present, however, perturbation solutions to the entire viscoelastic flow problem are very difficult to obtain if not impossible. Nevertheless, by assuming a zero-order velocity field solution, *i.e.*

the Newtonian velocity solution, and making use of the fact that the drag on the sphere can be indirectly calculated by considering the pressure difference on two ends of the bounding wall and the friction on the wall, Luo (1987) carried out a perturbation analysis and obtained an approximate expression for drag reduction valid for a very small elasticity level quantified by a dimensionless Weissenberg number, $Ws = \lambda U/R$, where λ is a fluid relaxation time, U is the terminal fluid velocity and R is the sphere radius. For purely viscous inelastic fluids, $Ws = 0$. In the presence of shear thinning, the drag change from the Newtonian case was a quadratic function of Weissenberg number. In the absence of shear thinning, the drag reduction was at least proportional to the fourth power of Weissenberg number. However, these results were not confirmed by his finite element analysis.

Many previous works have been contradictory to each other on how the fluid elasticity and shear thinning affect the drag. Acharya et al. (1976) found that for the flow of viscoelastic fluids past a solid sphere at low Reynolds numbers, the drag coefficient is in agreement with the Newtonian value, while Broadbent and Mena (1974) concluded from their results that the viscoelastic drag coefficient is less than the Newtonian value. Chhabra et al. (1977) have also experimentally examined the influence of fluid elasticity on the drag coefficient in the absence of shear thinning and found that for creeping flow the viscoelastic drag coefficient value was below the Newtonian value due to the elasticity effect.

Apart from the drag calculation, the streamline pattern is another major concern in the sphere problem. For a sphere bounded by a cylinder, a down-

stream shift from the Newtonian symmetric pattern is usually observed (Leslie, 1961; Giesekus, 1963; Sugeng and Tanner, 1986). This streamline downstream shift is depicted in Figure 1.1. According to Adachi et al. (1977), no shift in the streamlines was observed due to the non-Newtonian viscosity effect, which tends to decrease the pressure and friction drags. On the other hand, due to the viscoelastic effect, they found an increase in the normal force drag and upstream shift in the streamlines. Experimental results of Manero and Mena (1981) for flow of a viscoelastic fluid past a circular cylinder, show that there are two different streamline patterns which are strongly dependent on Weissenberg number but independent of the Reynolds number. For values of Weissenberg number less than unity a downstream shift of the streamlines was observed. On the other hand, for values of Weissenberg number greater than unity an upstream displacement of the streamlines was observed, which agree with the results of Sigli and Coutanceau (1977).

In recent years, two major numerical techniques has been used in the simulation of viscoelastic flows around spheres. These are the Boundary Element Method (BEM) and the Finite Element Method (FEM). These numerical techniques are suitable due to the ease of incorporating complicated geometrical boundaries. References of investigators who used these numerical techniques is given by Zheng et al. (1991). However, with few exceptions, these techniques fail to obtain convergent results for relatively high elasticity levels ($Ws>0.3$). A summary of the elasticity limits and the numerical techniques is given by Phan-Thien et al. (1991).

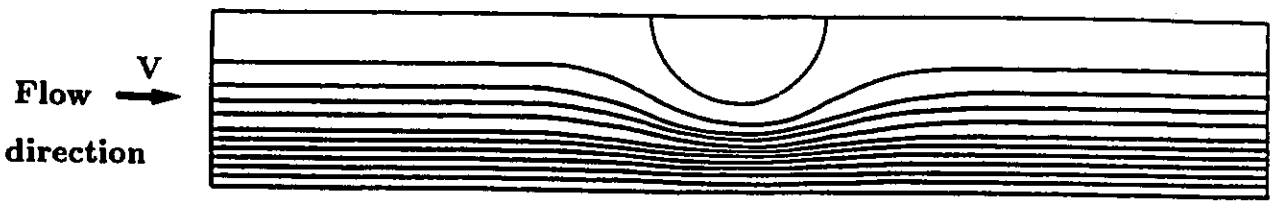

Figure 1.1: Streamline pattern showing a downstream shift from the Newtonian symmetric pattern for $Ws = 0.3$ (Luo, 1987).

1.3 Objectives

The objectives of this work are to study the behaviour of viscoelastic fluids by solving the appropriate governing conservation and constitutive equations for flows around spheres using the NACHOS finite element program (Luo, 1987). Details of the Galerkin finite element formulation for Newtonian viscous flows are fully described by Gartling (1978) and for non-Newtonian fluids by Luo (1987). We shall use integral constitutive equations to examine the flows of viscoelastic fluids past stationary spheres confined in cylinders. The emphasis will be on finding the extent of the change in the drag coefficient as the elasticity level increases. The significance of the wall effect will also be examined. First, flows of viscoelastic fluids past spheres with strong wall effects will be studied using the integral Maxwell model. Secondly, flows of less significant wall effects will be simulated using a memory integral K-BKZ model (Kaye, 1962; Bernstein et al., 1963) with multiple relaxation times. The drag correction factor (K) will be presented as a function of the dimensionless Weissenberg number.

The flow of viscoelastic fluids around stationary spheres will be considered as steady-state, incompressible, creeping flow (inertia forces negligible). The numerical study undertaken will include:

(a) Newtonian fluid

(b) ideal viscoelastic fluid according to the Maxwell model

(c) a test polymer solution (M1) fluid using the K-BKZ integral constitutive model.

Our results will be tested against known analytical and previous numerical so-

lutions and thus their accuracy will be established. Then the programs will be used for parametric studies in flows around spheres and finally to simulate experimental results available in the literature (Tirtaatmadja et al., 1990).

1.4 Outline of Thesis

Chapter (2): The equations of conservation of mass, momentum and energy are introduced and simplified using the appropriate assumptions. The models and the constitutive equations available for the description of flow of viscoelastic fluids around spheres are also presented. The relevant dimensionless groups are discussed and the appropriate boundary conditions are outlined. The method of solution is also presented. The Finite Element formulation (FEM) of continuity and momentum equations (velocities-pressure or $u-v-p$ formulation) is briefly discussed together with the stream function formulation.

Chapter (3): Results from pressure-driven Poiseuille flows are presented for planar and axisymmetric geometries. The integral Maxwell, Oldroyd-B and K-BKZ models are used and results are obtained for a range of elasticity levels based on a dimensionless Ws number. The validity and accuracy of the results are checked against analytical solutions.

Chapter (4): The benchmark problem of flow around a sphere contained in a cylinder with a 2:1 diameter ratio is considered. Results are presented for Newtonian and viscoelastic fluids obeying the Maxwell model. The drag correction factor is calculated with different finite element grids for Newtonian fluids to check the adequacy of the discretization, and the results are compared

with values available in the literature. As a further test for the numerical scheme, results for increasing elasticity levels are obtained using the integral Maxwell model. The drag correction factors obtained are compared with published results in the literature obtained with its differential counterpart.

Chapter (5): Numerical simulations are undertaken using the K-BKZ integral constitutive equation with multiple relaxation times for flows of viscoelastic fluids around spheres for which experimental results are available in the literature. Comparisons are made which give rise to concluding remarks.

Chapter (6): The results of this thesis are summarized for the various problems examined. Conclusions and recommendations for future work are presented.

Chapter 2

Mathematical Modelling of Viscoelastic Fluids

This chapter presents an introduction on the importance and need for analyzing and predicting the behaviour of viscoelastic materials. The general conservation equations for the flow analysis are presented along with the constitutive equations used. Finally the reduction of these equations for steady-state flows in planar and axisymmetric geometries is given under the appropriate assumptions.

2.1 Introduction

Rheology is the study of deformation and flow. It includes Newtonian fluid mechanics at one end of the spectrum of subject material and Hookean elasticity at the other. The region in between is governed by the domination of viscosity over elasticity or vice versa.

It is customary to classify the whole range of fluids into groups which possess similar flow properties. Rheologically, a fluid may approach one of the following ideal categories:

(a) *Inviscid fluids*: these exhibit negligible viscosities. The state of stress is isotropic and is given by the local pressure alone. Gases of very low viscosity flowing at high rates and away from boundaries can approach this idealization.

(b) *Newtonian liquids*: these exhibit viscosity independent of the rate of deformation and lack elasticity. The stress is a combination of the local pressure and the local viscous stress, which is in general anisotropic and a function of the local rate of deformation. Water, aqueous solutions, glycerine and many non-polymeric liquids and solutions behave as Newtonian liquids except in extreme circumstances.

(c) *Viscous inelastic liquids*: these exhibit deformation rate-dependent viscosity and no elasticity. The stress is a function of the local pressure and the local rate of deformation. Many sauces and juices, like mayonnaise and ketchup, and many non-polymeric suspensions and emulsions ordinarily fall in this class. In addition, these materials may exhibit yield stress (Abdali, 1992).

(d) *Viscoelastic liquids*: these exhibit deformation rate-dependent viscosity and elasticity. The stress is a function of the local pressure and of the deformation and rate of deformation to which the fluid particle was subjected in the past, *i.e.* upstream of its present location (Figure 2.1). Liquids, solutions, suspensions and emulsions of polymeric origin often behave as viscoelastic liquids.

(e) *Elastic solids*: these exhibit large viscosities and elasticities. The stress is

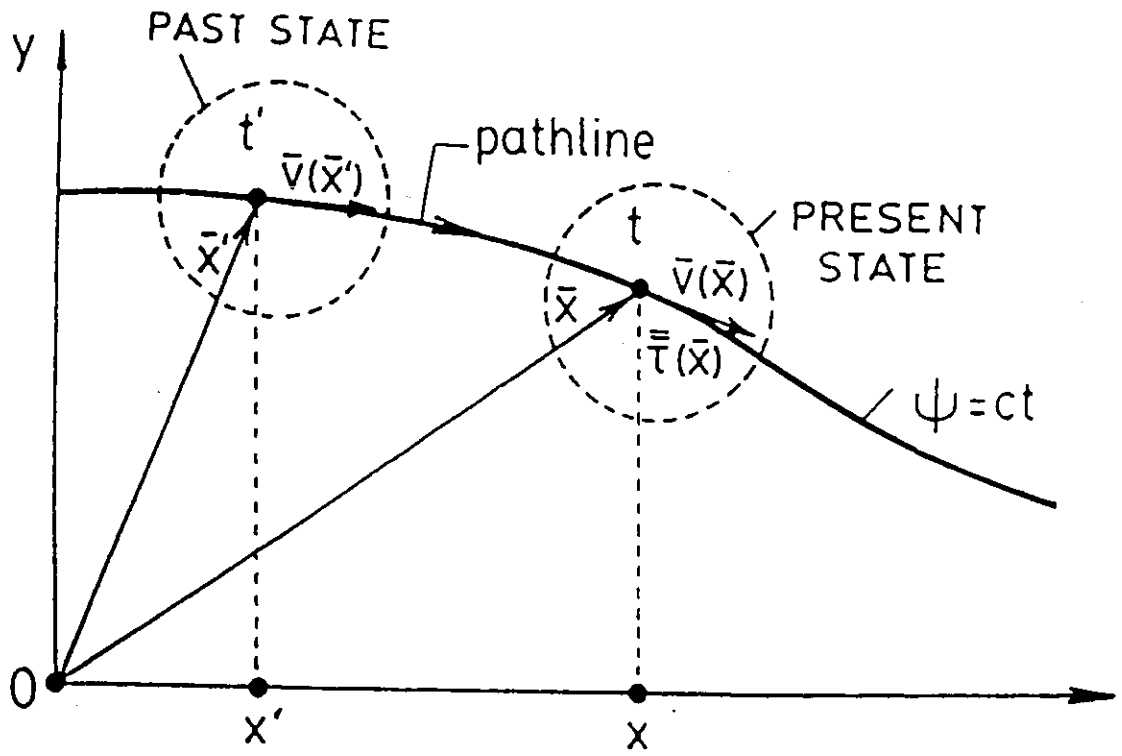

Figure 2.1: In steady-state flows of viscoelastic fluids, the present state of the stress $\bar{\bar{\tau}}(\bar{x})$ is a function of the present kinematics $[\bar{v}(\bar{x}),\ \nabla\bar{v}(\bar{x})]$ as well as of those of the past state $[\bar{u}(\bar{x}'), \nabla\bar{v}(\bar{x}')]$.

a function of the local pressure and local deformation. Rubber and most metallic solids behave as elastic solids if they are not too greatly deformed.

2.2 Viscoelastic Liquids

Non-Newtonian viscoelastic flow is perhaps one of the most fascinating phenomena in the world of fluids. It is well known that liquids with complex structure, such as polymer solutions and melts, behave in unexpected ways and fail to obey either Newton's linear law of friction or Hooke's linear law of elasticity (Lodge, 1964, 1974; Walters, 1980).

Viscoelasticity refers to the simultaneous existence of viscous and elastic properties in a material. Viscoelastic liquids possess memory: past deformations of a liquid *particle* contribute to the present state of stress in that *particle* (see Figure 2.1). The state of stress in it and in its neighbours combine with any external forces on them to determine their motion. Moreover their memory is fading; only recent deformations contribute heavily to the present state of stress. Associated with the fading memory is the ability of viscoelastic liquids to undergo delayed elastic recovery, *i.e.* after suffering external stresses they tend to recover their earlier undeformed state. This recovery is never complete for viscoelastic liquids because of their viscous character. Newtonian liquids, lacking memory, do not recover at all. Ideal elastic solids, having perfect memory, recover completely.

Unlike in Newtonian liquids, elasticity gives rise to large viscoelastic normal stresses even in unidirectional shear flows. The first normal stress coefficient

(ratio of the difference between the normal stress in the direction of flow and that in a perpendicular direction) like the viscosity depends on the rate of deformation. The combination of viscosity with elasticity results in some strange viscoelastic flow phenomena which are qualitatively different from pure Newtonian viscous flow. These include (see also Figure 2.2): (1) the **Weissenberg effect**, in which a polymeric liquid climbs up a rotating rod; (2) the reversal of direction of the secondary-flow pattern when a disc rotates a liquid in a beaker; (3) the slight bulging of the surface of a liquid as it flows down a trough; (4) the tubeless-siphon effect, in which a siphon continues to operate even though there is a gap between the end of the tube and the surface of the liquid; (5) the swelling of extrudates issuing from a die; (6) the development of toroidal vortex upstream when a liquid flows from a larger-diameter tube to a small diameter tube, and many others.

In order to describe these bizzare effects which are qualitatively different from those of Newtonian liquids, it is required to develop a fundamental relationship between deformation and stress through a constitutive equation. There is no doubt on the importance of fluids which exhibit viscoelastic properties. However, it is the subject of modern research in the field of rheology to find a general constitutive equation which can describe adequately the flow phenomena of these materials.

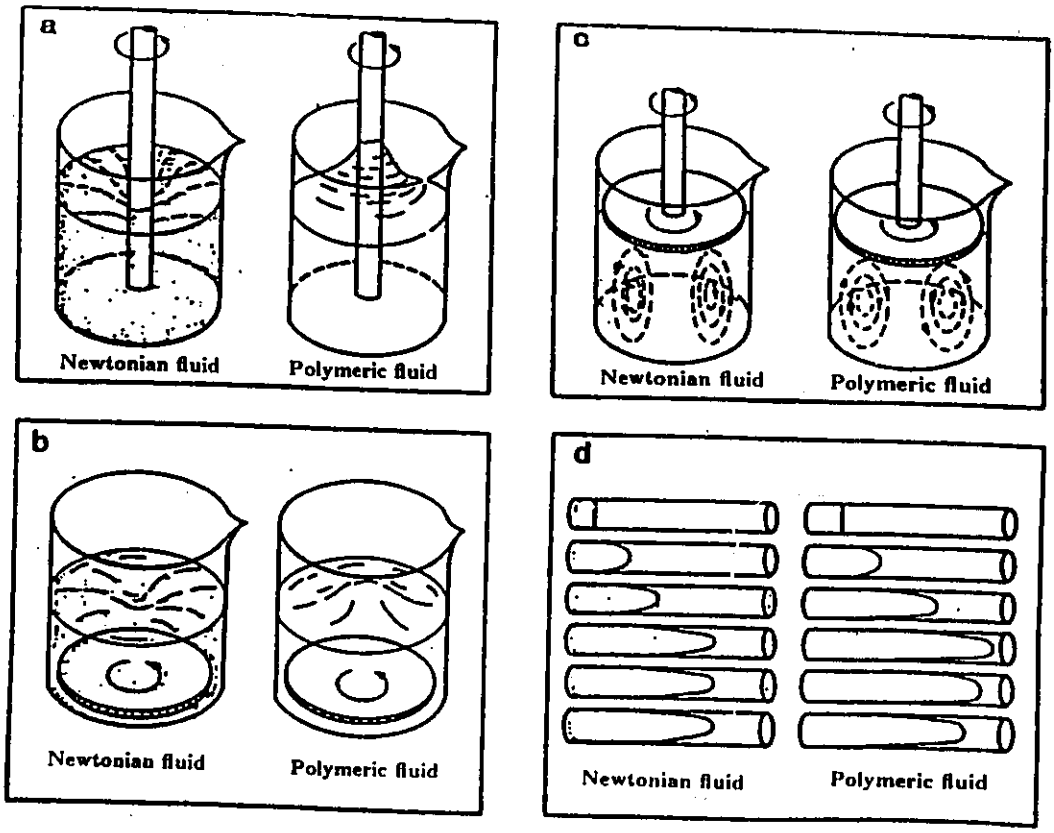

Figure 2.2: Unusual flows. The ten experiments sketched here show how the behaviour of polymeric liquids is qualitatively different from that of Newtonian liquids. A polymeric liquid climbs a rotating rod in a; rises above a rotating disc in b; moves radially inward along a rotating disc in c; recoils in a tube when the pump is turned off in d; swells when it emerges from a tube in e; siphons across a gap in f; develops a slightly convex surface when flowing down a trough in g; develops a vortex when the tube diameter decreases for slow flow in h; moves toward a transversely oscillating cylinder along the line of oscillation in i; and causes falling spheres to grow further apart in j (Papanastasiou, 1984).

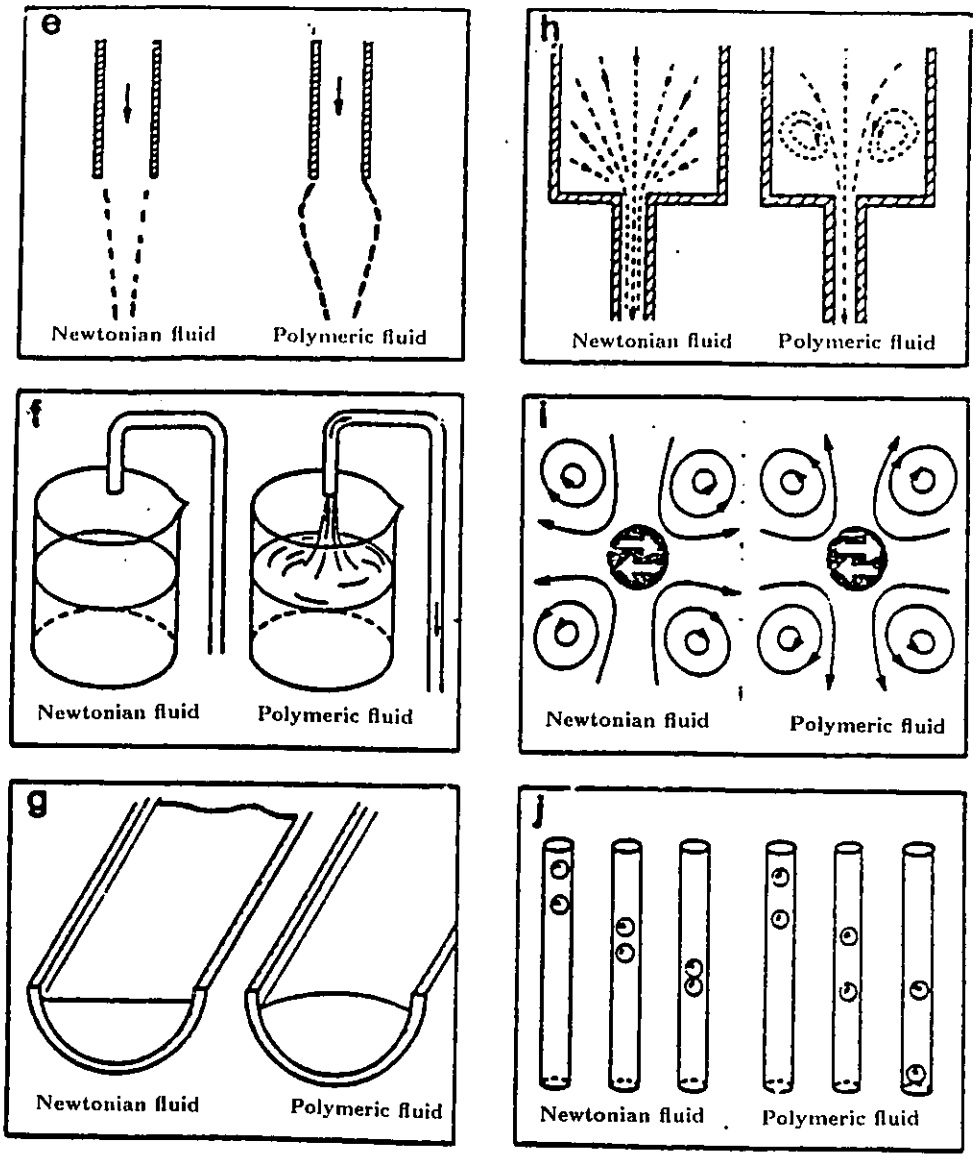

Figure 2.2 continued...

Constitutive equations that have been used in computational schemes may be classified into the following categories (Tanner, 1992):

(a) **Rate-type equations:** these include generalized Newtonian, viscometric and higher-order equations.

(b) **Differential models:** these include Maxwell, Oldroyd-B, Phan-Thien/Tanner (PTT), modified Phan-Thien/Tanner (MPTT), Leonov and modified Leonov, Giesekus and other models.

(c) **Integral-type expansions:** these include Green-Rivlin expansions, K-BKZ, inelasticity and Larson's equivalents.

It has been shown that the rate-type equations are inadequate for describing general flows (Tanner, 1988). For the differential models a great deal of effort has been expended, especially for the Maxwell and Oldroyd-B models (Crochet, 1989). However, problems involving free surfaces and stress singularities cannot be solved using these models. Of the integral expansions, the K-BKZ model has been found to be the most realistic model (Tanner, 1992). This model has been successful in many numerical simulations, and good agreement has been achieved between numerical simulations and experimental results (Luo and Tanner, 1988; Luo and Mitsoulis, 1990; Park and Mitsoulis, 1992).

2.3 Conservation Equations

The governing equations in non-Newtonian fluid mechanics consist of conservation equations and constitutive equations, with the choice of the latter being

often at one's disposal. The conservation equations are the usual classical ones: the equation of continuity, which is a formal mathematical expression of the principle of conservation of mass; the stress equation of motion, which arises from the application of Newton's second law of motion to a moving continuum and the local expression of the principle of balance of angular momentum; and the energy equation, which is a specific continuum statement of the first law of thermodynamics.

In general tensorial form the conservation equations are (Bird et al., 1960):

Mass:

$$\frac{D\rho}{Dt} + \rho(\nabla \cdot \bar{v}) = 0 \tag{2.1}$$

Momentum:

$$\rho\frac{D\bar{v}}{Dt} = -\nabla p + \nabla \cdot \bar{\bar{\tau}} + \rho\bar{g} \tag{2.2}$$

Energy:

$$\rho C_p \frac{DT}{Dt} = -\nabla \cdot \bar{q} + \bar{\bar{\tau}} : \nabla\bar{v} \tag{2.3}$$

The following assumptions are made based on the present study:

(a) the fluid is incompressible (constant density), then the material derivative of the mass density vanishes identically and the conservation of mass (Equation 2.1) reduces to:

$$\nabla \cdot \bar{v} = 0 \tag{2.4}$$

The incompressibility assumption is not valid when large pressure gradients are present. However for most viscoelastic materials under creeping flow conditions, equation (2.4) is indeed applicable.

The equation of conservation of momentum involves a balance between inertia, viscous, pressure and body forces. Since viscoelastic creeping flows are considered in this study, it may be assumed that:

(b) inertia effects are negligible in comparison with viscous and pressure forces. We also assume that:

(c) body forces (such as gravity) are negligible in comparison with viscous and pressure forces;

(d) the flow is steady ($\frac{\partial}{\partial t} = 0$), which applies to many viscoelastic processes. Thus, the conservation of momentum Equation (2.2) reduces to:

$$0 = -\nabla p + \nabla \cdot \bar{\bar{\tau}} \tag{2.5}$$

Finally, the assumption of isothermal flows in the present work makes the use of the energy equation (2.3) unnecessary.

2.4 Constitutive Equations

To solve the above equations we also need constitutive equations that relate the extra stress tensor $\bar{\bar{\tau}}$ to the rate-of-strain tensor $\bar{\bar{\dot{\gamma}}}$ given by:

$$\bar{\bar{\dot{\gamma}}} = \nabla \bar{v} + (\nabla \bar{v})^T \tag{2.6}$$

2.4.1 Newtonian Fluid

For Newtonian fluids we have:

$$\bar{\bar{\tau}} = \mu \bar{\bar{\dot{\gamma}}} = \mu \dot{\gamma}_{ij} \tag{2.7}$$

where μ is a constant viscosity coefficient and $\dot{\gamma}_{ij}$ are the components of $\bar{\bar{\dot{\gamma}}}$.

2.4.2 The Maxwell Integral Model

The upper-convected Maxwell model of the integral type is given by the following equation (Luo and Tanner, 1988):

$$\bar{\bar{\tau}}(t) = \frac{1}{1-\theta}\int_{-\infty}^{t} \frac{\mu}{\lambda^2} exp\left(-\frac{t-t'}{\lambda}\right)\left[\{\bar{\bar{C}}_t^{-1}(t') - \bar{\bar{I}}\} + \theta\{\bar{\bar{C}}_t(t') - \bar{\bar{I}}\}\right] dt' \qquad (2.8)$$

where μ is a constant viscosity, λ is a single relaxation time, $\bar{\bar{C}}_t^{-1}$ is the Finger strain tensor, $\bar{\bar{C}}_t$ is the Cauchy-Green tensor and $\bar{\bar{I}}$ is the identity tensor (see also Appendix A for further definitions). The θ factor is related to the ratio of the second normal stress difference $N_2 = \tau_{22} - \tau_{33}$ to the first normal stress difference $N_1 = \tau_{11} - \tau_{22}$ in simple shear flow so that:

$$\frac{N_2}{N_1} = \frac{\theta}{1-\theta} \qquad (2.9)$$

The above model is of particular importance in the development of numerical techniques because it has a simple differential counterpart and because some analytical solutions exist in a few simple cases.

2.4.3 The Oldroyd-B Integral Model

The integral analogue of the Oldroyd-B model is given by (Wesson et al., 1988):

$$\bar{\bar{\tau}}(t) = \mu_s\bar{\bar{\dot{\gamma}}} + \frac{1}{1-\theta}\int_{-\infty}^{t} \frac{\mu_m}{\lambda_1^2} exp\left(-\frac{t-t'}{\lambda_1}\right)\left[\{\bar{\bar{C}}_t^{-1}(t') - \bar{\bar{I}}\} + \theta\{\bar{\bar{C}}_t(t') - \bar{\bar{I}}\}\right] dt' \qquad (2.10)$$

$$\mu = \mu_m + \mu_s, \qquad (2.11a)$$

$$\lambda_2 = \lambda_1\frac{\mu_s}{\mu_m + \mu_s}, \qquad (2.11b)$$

with λ_1 and λ_2 the relaxation and retardation times, respectively, and μ the constant viscosity. Commonly, $\mu_m = 8\mu/9, \mu_s = \mu/9$ and thus $\lambda_2 = \lambda_1/9$.

Equation (2.10) models solutions of viscoelastic liquid of relaxation time λ_1 and constant viscosity μ_m in a Newtonian solvent of viscosity μ_s. The Oldroyd-B integral model reduces to the Maxwell model (2.8) when $\mu_s = 0$ and to the Newtonian fluid when $\lambda_1 = 0$.

In simple shear flow, the Maxwell and Oldroyd-B fluids have a constant viscosity, a constant first normal stress coefficient ($\Psi_1 = N_1/\dot{\gamma}^2$), a zero second normal stress coefficient ($\Psi_2 = N_2/\dot{\gamma}^2$) and a first normal stress difference N_1 that is quadratic in the shear rate ($\dot{\gamma}$). These models also exhibit an infinite elongational viscosity η_E at a certain value of the elongational rate $\dot{\epsilon}$ (see Figure 2.3). This is not the case for most viscoelastic materials because the elongational viscosity may increase, remain constant or decrease with the elongational rate depending on the nature of the fluid. Figure 2.4 shows the dependence of elongational viscosity on the elongational rate for low-density polyethylene (LDPE), high-density polyethylene (HDPE) (Laun, 1980) and polystyrene (PS) (Münstedt, 1980). The behaviour of these two models is totally unrealistic for real viscoelastic materials.

Viscoelastic materials exhibit a shear-rate dependent viscosity (see Figure 2.5) and first normal stress coefficient, and a negative second normal stress coefficient, approximately $10-30\%$ of the first normal stress coefficient (Mitsoulis, 1990). Interest in studying these models is essentially qualitative. However, a numerical technique developed for solving the flow of such fluids could be extended without major difficulty to the flow of more realistic fluids.

MODEL PREDICTIONS

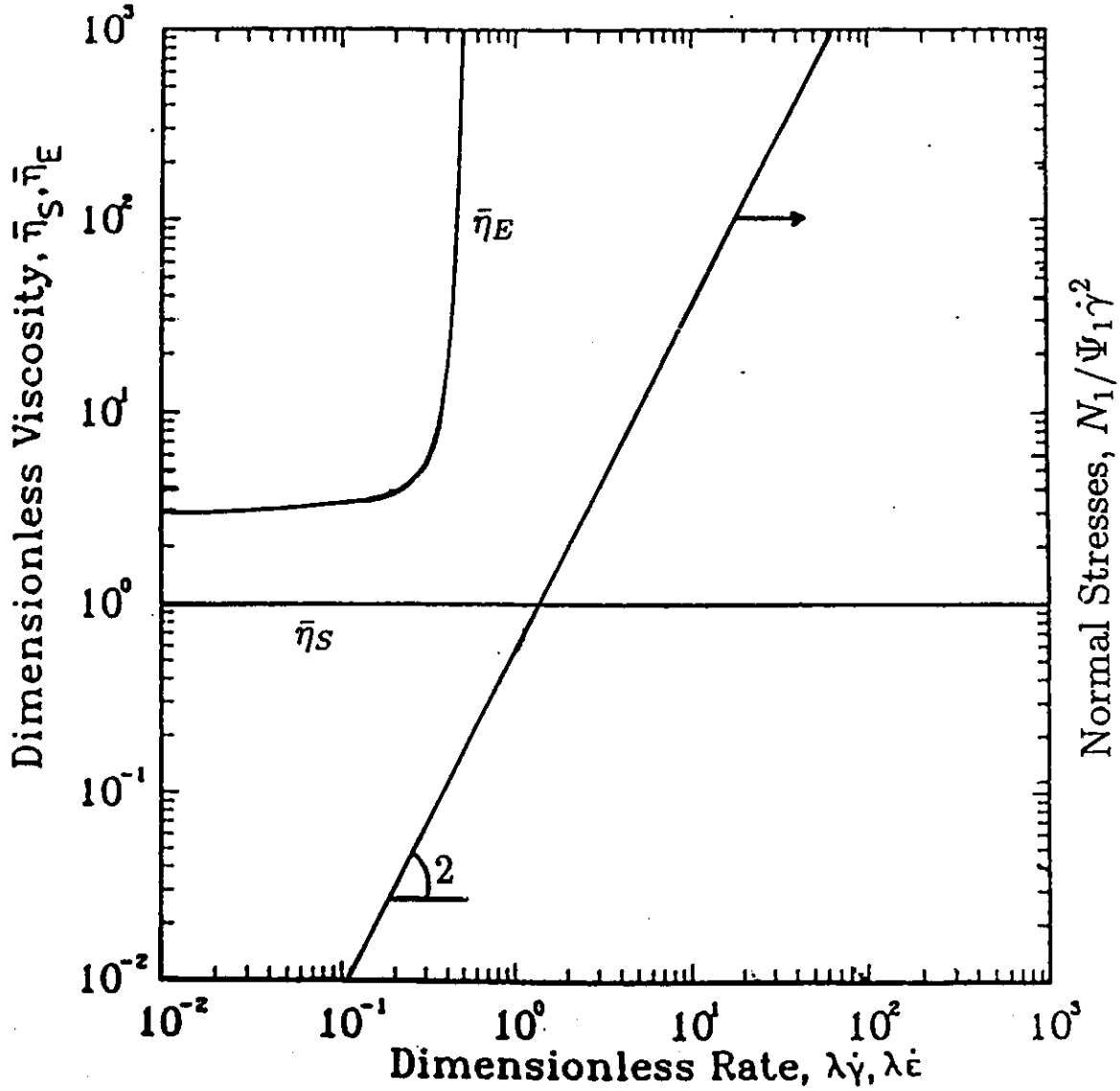

Figure 2.3: Dimensionless steady-state shear viscosity ($\bar{\eta}_S = \eta_S/\mu$), and elongational viscosity ($\bar{\eta}_E = \eta_E/\mu$) as a fuction of dimensionless shear rate ($\lambda\dot{\gamma}$) or strain rate ($\lambda\dot{\epsilon}$) for Maxwell and Oldroyd-B models (Bush et al., 1985).

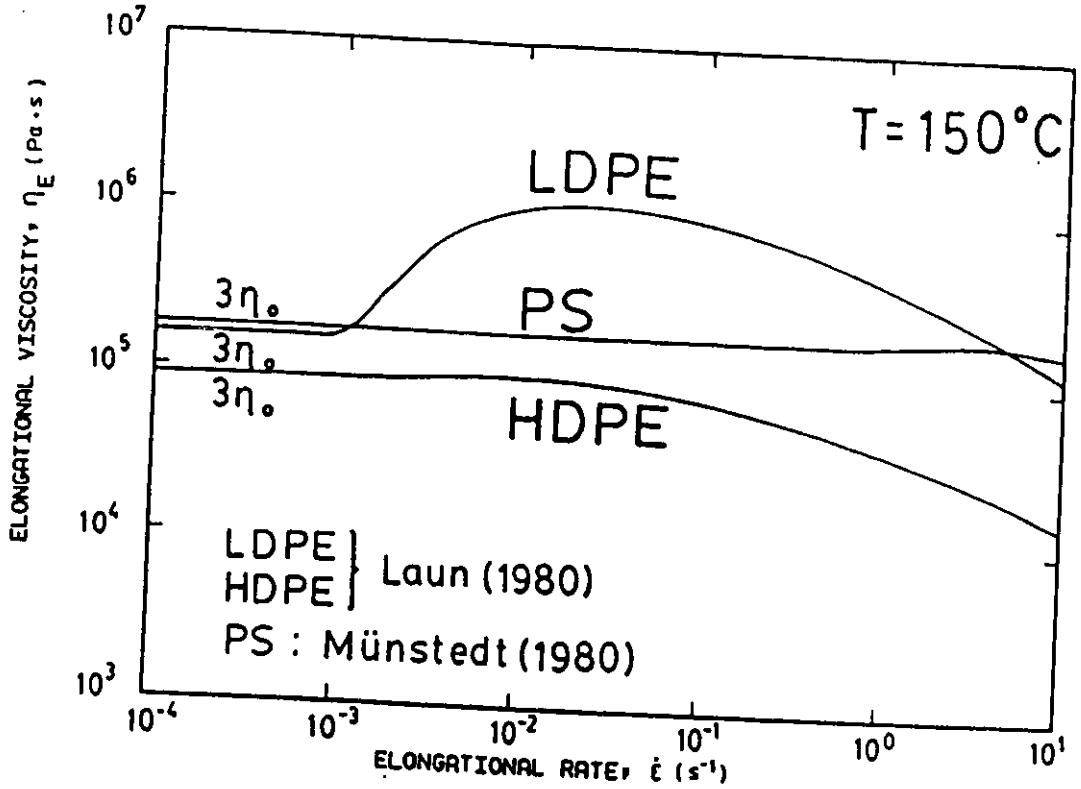

Figure 2.4: Steady-state elongational viscosity (η_E) as a function of elongational rate ($\dot{\epsilon}$) for PS, LDPE and HDPE at 150°C.

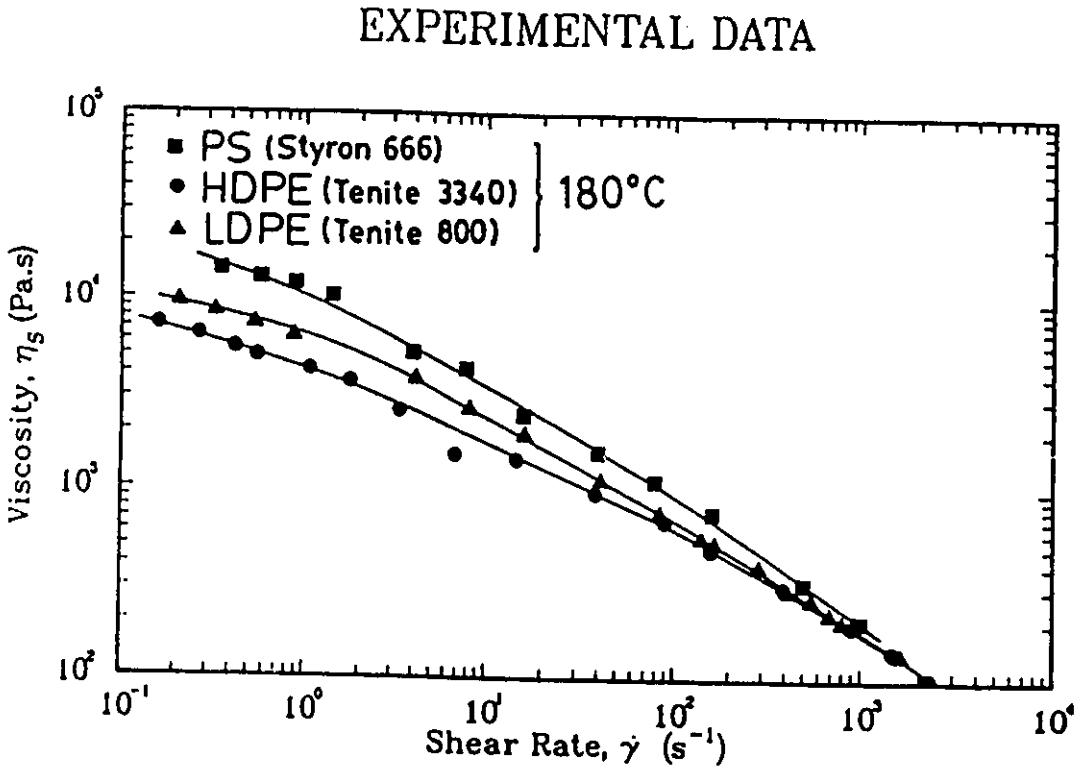

Figure 2.5: Steady-state shear viscosity (η_S) as a function of shear rate ($\dot{\gamma}$) for PS, LDPE and HDPE at 180 ^oC (Ballenger et al., 1971).

2.4.4 The K-BKZ Integral Model

The K-BKZ equation proposed by Papanastasiou et al. (1983), and further modified by Luo and Tanner (1988), has the following form:

$$\bar{\bar{\tau}}(t) = \frac{1}{1-\theta}\int_{-\infty}^{t} \mathbf{M}(t-t')\Phi\left(\bar{\bar{I}}_c, \bar{\bar{I}}_{c^{-1}}\right)\left[\{\bar{\bar{C}}^{-1}(t') - \bar{\bar{I}}\} + \theta\{\bar{\bar{C}}(t') - \bar{\bar{I}}\}\right] dt' \tag{2.12}$$

where:

$$\mathbf{M}(t-t') = \sum_{k=1}^{N} \frac{a_k}{\lambda_k} exp\left(-(t-t')/\lambda_k\right) \tag{2.13}$$

is a linear time-memory function with N modes, and $\Phi(\bar{\bar{I}}_c, \bar{\bar{I}}_{c^{-1}})$ is a non-linear strain-memory function given by

$$\Phi(\bar{\bar{I}}_c, \bar{\bar{I}}_{c^{-1}}) = \frac{\alpha}{(\alpha-3) + \beta\bar{\bar{I}}_{c^{-1}} + (1-\beta)\bar{\bar{I}}_c} \tag{2.14}$$

where λ_k and a_k are the relaxation times and relaxation modulus coefficients at a reference temperature T_0, respectively, α and β are material parameters chosen to fit the shear and elongational viscosities respectively, and $\bar{\bar{I}}_c$ and $\bar{\bar{I}}_{c^{-1}}$ are the first invariants of the Cauchy-Green tensor $\bar{\bar{C}}_t$ and its inverse $\bar{\bar{C}}_t^{-1}$, the Finger strain tensor. The K-BKZ model predictions of shear viscosity, first normal stress difference, and elongational viscosity for high-density polyethylene (HDPE) are shown in Figure 2.6, while the values of the constants are given in Table 2.1. The model has been used in earlier simulations by Luo and Mitsoulis (1989) to fit experimental data (symbols) given by Orbey and Dealy (1984).

The upper-convected Maxwell model of the integral type, Equation (2.8), is readily obtained by setting $N = 1$, $\lambda_1 = \lambda$, $a_1 = 1$, $\alpha \to \infty$ (or equivalently a very large number, say 10,000) and $\beta = 0$.

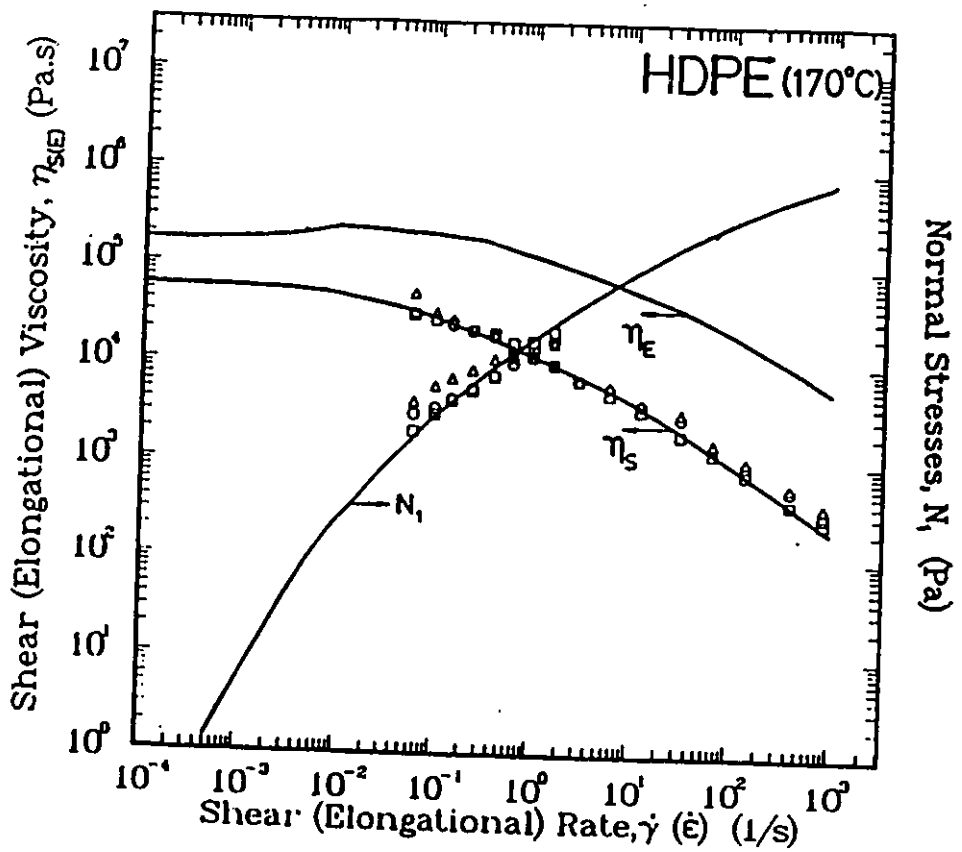

Figure 2.6: Model predictions (solid lines) of shear viscosity η_S, first normal stress difference N_1, and elongational viscosity η_E for HDPE melt at $170°C$ using Equation (2.12) (Luo and Mitsoulis, 1990). Symbols are experimental data given by Orbey and Dealy (1984).

Table 2.1: Material parameter values used in the K-BKZ model for fitting data of HDPE melt at 170°C ($\alpha = 5.1,\ \beta = 0.1,\ \theta = -0.25$)

k	λ_k (s)	$a_k(Pa)$
1	$1.0\text{x}10^{-4}$	$5.20\text{x}10^{5}$
2	$1.0\text{x}10^{-3}$	$1.48\text{x}10^{5}$
3	$1.0\text{x}10^{-2}$	$9.16\text{x}10^{4}$
4	$1.0\text{x}10^{-1}$	$4.21\text{x}10^{4}$
5	$1.0\text{x}10^{0}$	$8.80\text{x}10^{3}$
6	$1.0\text{x}10^{1}$	$2.12\text{x}10^{3}$
7	$1.0\text{x}10^{2}$	$2.10\text{x}10^{2}$
8	$1.0\text{x}10^{3}$	$6.0\text{x}10^{-1}$

2.5 Governing Equations

The flow of viscoelastic materials around spheres is in general three-dimensional. However, since the fluid flow occurs inside tubular or annular geometries (like cylinders) or flat surfaces that can be considered two-dimensional, such geometries conveniently allow the reduction of the problem from three to two dimensions. In Cartesian coordinates we assume no change in the z-direction. In cylindrical coordinates no changes in the θ-direction could be safely assumed. Due to these assumptions the three-dimensional problem can be fully described as two-dimensional with two independent variables, namely x and y (planar case) and r and z (axisymmetric case).

2.5.1 Planar Geometries

For planar geometries, the continuity equation can be written as (Bird et al., 1960):

$$\frac{\partial v_x}{\partial x} + \frac{\partial v_y}{\partial y} = 0 \tag{2.15}$$

The equation of conservation of momentum gives:

$$(x - momentum) \qquad 0 = -\frac{\partial p}{\partial x} + \frac{\partial \tau_{xy}}{\partial y} + \frac{\partial \tau_{xx}}{\partial x} \tag{2.16}$$

$$(y - momentum) \qquad 0 = -\frac{\partial p}{\partial y} + \frac{\partial \tau_{yx}}{\partial x} + \frac{\partial \tau_{yy}}{\partial y} \tag{2.17}$$

It should be noted that because of the symmetry of the stress tensor, $\tau_{xy} = \tau_{yx}$. Thus, only three stress components are needed for planar flows. This simplifies the analysis by using a stress vector $(\tau_{xx}, \tau_{yy}, \tau_{xy})$ and a corresponding rate-of-strain vector $(\dot{\gamma}_{xx}, \dot{\gamma}_{yy}, \dot{\gamma}_{xy})$.

For planar flows, the Newtonian constitutive equation gives:

$$\tau_{xx} = 2\mu \frac{\partial v_x}{\partial x} \tag{2.18}$$

$$\tau_{yy} = 2\mu \frac{\partial v_y}{\partial y} \tag{2.19}$$

$$\tau_{xy} = \mu \left(\frac{\partial v_x}{\partial y} + \frac{\partial v_y}{\partial x} \right) \tag{2.20}$$

2.5.2 Axisymmetric Geometries

For axisymmetric geometries, the continuity equation can be written as (Bird et al., 1960):

$$\frac{\partial v_r}{\partial r} + \frac{v_r}{r} + \frac{\partial v_z}{\partial z} = 0 \tag{2.21}$$

The equation of conservation of momentum gives:

$$0 = -\frac{\partial p}{\partial r} + \frac{\partial \tau_{rr}}{\partial r} + \frac{\tau_{rr}}{r} + \frac{\partial \tau_{rz}}{\partial z} - \frac{\tau_{\theta\theta}}{r} \tag{2.22}$$

$$0 = -\frac{\partial p}{\partial z} + \frac{\partial \tau_{rz}}{\partial r} + \frac{\tau_{rz}}{r} + \frac{\partial \tau_{zz}}{\partial z} \tag{2.23}$$

It should be noted that because of the symmetry of the stress tensor, $\tau_{rz} = \tau_{zr}$. Thus, only four stress components are needed for axisymmetric flows. This simplifies the analysis by using a stress vector $(\tau_{rr}, \tau_{zz}, \tau_{rz}, \tau_{\theta\theta})$ and a corresponding rate-of-strain vector $(\dot{\gamma}_{rr}, \dot{\gamma}_{zz}, \dot{\gamma}_{rz}, \dot{\gamma}_{\theta\theta})$.

For axisymmetric flows, the Newtonian constitutive equation gives:

$$\tau_{rr} = 2\mu \frac{\partial v_r}{\partial r} \tag{2.24}$$

$$\tau_{\theta\theta} = 2\mu \frac{v_r}{r} \tag{2.25}$$

$$\tau_{zz} = 2\mu \frac{\partial v_z}{\partial z} \tag{2.26}$$

$$\tau_{rz} = \mu \left(\frac{\partial v_z}{\partial r} + \frac{\partial v_r}{\partial z} \right) \tag{2.27}$$

The viscoelastic constitutive equations described in section 2.4 when substituted in the momentum equations give stress components which are very complicated integro-differential equations, and thus are not given here. However, they are used in a fully two-dimensional finite element analysis to simulate the behaviour of viscoelastic fluids in test planar and axisymmetric flows, where simple expressions can be derived (see chapter 3).

2.6 Dimensionless Groups

Before proceeding with the boundary conditions necessary for the solution of the governing conservation and constitutive equations, it is interesting to examine

the relevant dimensionless numbers in viscoelastic flows. The various dimensionless groups are used to characterize the relative significance of each term in the conservation equations of momentum. The dimensionless groups are calculated at a characteristic length H or a characteristic radius R and a characteristic velocity V. In the context of flow past a sphere, R is the sphere radius and V is the average fluid velocity. It is appropriate then to define a characteristic (nominal or surface-average) shear rate

$$\dot{\gamma}_a = \frac{V}{R} \tag{2.28}$$

and a zero-shear viscosity (the viscosity in the limit of vanishing shear rate)

$$\eta_o = \sum_{k=1}^{N} a_k \lambda_k \tag{2.29}$$

With the above definitions at hand we can now define the relevant dimensionless groups of interest in the analysis.

1. **Reynolds Number** Re

$$Re = \frac{2\rho V R}{\eta_o} \tag{2.30}$$

For Newtonian fluids, η_o is replaced by the Newtonian viscosity μ. The Reynolds number is a measure of the relative importance of inertia forces compared to viscous forces in the equation of momentum. For viscoelastic flows in general, $Re \ll 1$, and the creeping flow approximation is valid. As a result the inertia terms are not included in the calculations.

2. **Weissenberg Number** Ws

$$Ws = \lambda V/R \tag{2.31}$$

For Newtonian fluids, Ws=0. The Weissenberg number is a measure of the relative importance of elastic forces compared to viscous forces. For viscoelastic flows in general, $Ws \neq 0$, and it may reach values Ws>1.

3. **Deborah Number** De The Deborah number is the ratio of a characteristic relaxation time λ of the material to a characteristic time t_0 of the relevant deformation process (taken usually as $1/\dot{\gamma}_a$) .

$$De = \frac{\lambda}{t_0} = \lambda \dot{\gamma}_a \tag{2.32}$$

Since $\dot{\gamma}_a = V/R$, the above definitions of Ws and De are identical.

4. **Recoverable Stress Ratio** S_R The recoverable stress ratio is defined as follows:

$$S_R = \frac{N_1}{2\tau_w} = \frac{N_1}{2\eta_S \dot{\gamma}_w} \tag{2.33}$$

where N_1 is the first normal stress difference, τ_w is the shear stress at the wall, ans η_S is the shear viscosity.

5. **Dimensionless Stress** τ^*

For computing purposes it is necessary to define a dimensionless stress τ^* which is given by

$$\tau^* = \frac{\tau R}{\eta_o V} \tag{2.34}$$

6. **Dimensionless Pressure** P^*

For computing purposes, the dimensionless pressure is defined in a similar manner to the dimensionless stress.

$$P^* = \frac{PR}{\eta_o V} \tag{2.35}$$

7. **Dimensionless Drag Correction Factor K**

For the flow of Newtonian fluids around spheres at low Reynolds numbers, Stokes' law is valid, which is expressed as

$$D_\infty = 6\pi R\mu V \tag{2.36}$$

where D_∞ is the drag force on a sphere of radius R moving with a constant velocity V in an unbounded Newtonian fluid. In any other case, such as non-negligible Re or Ws numbers or a bounded medium, the drag correction factor is then defined as

$$K = \frac{F_D}{D_\infty} \tag{2.37}$$

where F_D is the drag force over the sphere.

2.7 Boundary Conditions

The solution of the conservation equations (2.1-2.4) can be obtained by imposition of appropriate boundary conditions. In order to solve boundary-value problems such as in fluid flows around spheres, a complete set of boundary conditions is necessary.

There are basically two types of boundary conditions (Huebner and Thornton, 1982):

1 - Essential boundary conditions (or fixed boundary conditions);

2 - Natural boundary conditions (or flux boundary conditions).

The first type refers to the primary variable, e.g. velocities for the flow analysis, temperatures for the thermal analysis, and stream function values for a flow analysis based on stream function formulation. The second type of boundary

conditions refers to the secondary variables (usually derivatives of the primary variables), e.g. surface traction for the flow analysis, heat fluxes for the thermal analysis and velocities for the stream function formulation.

More specifically, for flow problems the following set of boundary conditions is available (Ben-Sabar and Caswell, 1979):

1 - V_n, V_t pure velocity conditions; specify V_n, V_t

2 - T_n, T_t pure surface traction conditions; specify T_n, T_t

3 - T_n, V_t *or* V_n, T_t mixed conditions; specify T_n, V_t *or* V_n, T_t

where the subscripts n and t represent the components of a vector in the normal and tangential direction to a surface, respectively. In flow problems, velocity conditions (type 1) are most commonly encountered. However in materials processing, the appearance of free surfaces requires the specification of surface tractions (type 2). Such surface tractions can be air drag, drawdown forces, surface tension, etc.

The boundary conditions for the stream function are (Huebner and Thornton, 1982):

1 - stream function conditions; specify ψ

2 - velocity conditions; specify $\frac{\partial \psi}{\partial \bar{n}}$

where $\frac{\partial \psi}{\partial \bar{n}}$ represents the tangential velocity at the surface.

2.8 Method of Solution

The numerical method used in this study is the Finite Element Method (FEM). The finite element method is a numerical analysis technique for obtaining ap-

proximate solutions to a wide variety of engineering problems. The main advantage of FEM over other numerical methods is its ability to solve problems in irregular and complex geometries with unusual boundary conditions (Vlachopoulos, 1977). The overall numerical formulation for a viscoelastic flow problem is very much similar to that for a Newtonian viscous flow problem. In fact, within one iteration, numerical discretization and solution procedure for the field equations is almost identical to that of a Newtonian problem, thus existing numerical methods for Newtonian viscous flow can be adapted without difficulty. The separation of field equations and constitutive equations by a Picard-type iterative scheme enable us to *borrow* from the relatively rich library of Newtonian viscous flow computer packages and solve the constitutive equations for the non-Newtonian extra stresses and meeting other specific challenges encountered exclusively in non-Newtonian flow simulations.

2.8.1 The General Iterative Process

As opposed to a *mixed formulation*, a *non-mixed formulation* for non-Newtonian flow problems does not define nodal stress unknowns at all in the discretized numerical system. Instead, an iterative scheme of the Picard type (direct substitution) is employed to calculate the extra stresses in the momentum equations. In the process, knowledge of the velocity field obtained from a previous iteration is provided to the constitutive equations for computing the non-Newtonian extra stresses at some relevant points. After the non-Newtonian extra stresses have been calculated, they are treated as pseudo-body forces in the discretized system for the momentum equations in the next iteration. This process is repeated

until some preassigned convergence criterion is satisfied.

2.8.2 Galerkin Finite Element Formulation

Details of the Galerkin finite element formulation for Newtonian viscous flow in the program NACHOS are fully described by Gartling (1978), and the basic concepts of finite element construction and the isoparametric element formulation are thoroughly discussed in the literature (Oden, 1972; Huebner, 1975; Gallagher, 1975; Zienkiewicz, 1980; Crochet et al., 1984). The formulation presented here was directly adapted from that of the original Newtonian program NACHOS, and the implementation of the iterative process for solving viscoelastic flow problems is discussed by Luo (1987). The solution method is based on the Galerkin form of the FEM and a novel particle tracking integration technique (Luo and Mitsoulis, 1990). This scheme decouples the momentum equation and the constitutive equation by treating the non-linear elastic stresses as pseudo-body forces. During each iteration the program performs particle tracking and integrates the integral constitutive equation along the particle lines.

Of central importance to a finite element formulation is the choice of particular elements and shape functions. Among other types of basic elements included in NACHOS (Gartling, 1978), the 8-node isoparametric quadrilateral serendipity elements were found suitable for this work (Luo and Mitsoulis, 1990). Each element has 8 nodes and 20 degrees of freedom for an isothermal problem (see Figure 2.7). Within each element, the velocity components are approximated by using quadratic interpolation functions while the pressure is approximated by using bilinear shape functions. The Galerkin form of the method of weighted

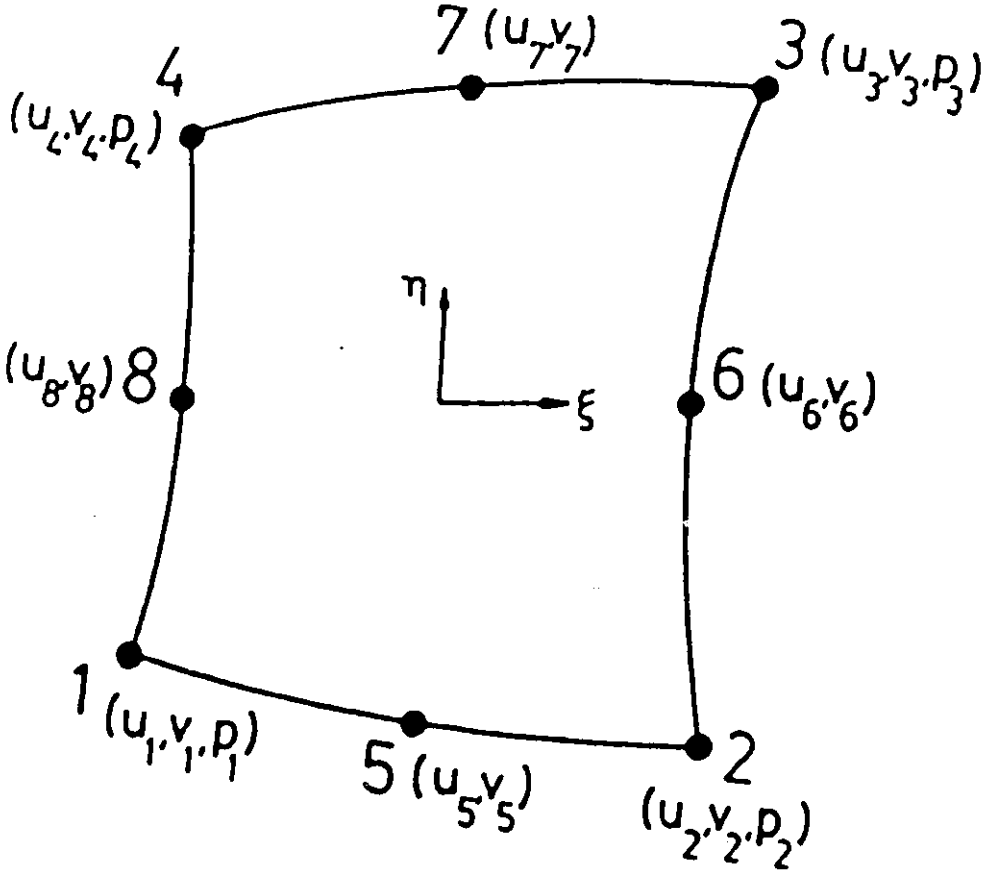

Figure 2.7: 8-node, isoparametric, quadrilateral, serendipity element used in the FEM analysis (u-v-p formulation).

residuals (Finlayson, 1972), was adapted to minimize errors by making the residuals orthogonal to the interpolation functions over each element.

The analysis using NACHOS follows the procedure as outlined in the flowchart of Figure 2.8 and Figure 2.9. A complete data file is composed of input data essential for proper simulation using the FEM. Such data includes material properties, operating and boundary conditions, information to allow construction of the finite element grid, geometric structure of the flow domain, required number of solution and/or free surface iterations, and various flags to invoke or suppress certain capabilities of the program (such as non-isothermal or non-Newtonian analysis). Initially the finite element grid is constructed, after which all other data is incorporated. If the analysis is non-isothermal, temperature data is read in from an external file and used to calculate new material property values.

Since this method is based on solution contributions from area domains rather than individual points, the differential equations are rewritten in approximate integral equations and having set the boundary conditions, a set of simultaneous linear algebraic equations is created. The primitive variables are then found from the following expression:

$$\begin{pmatrix} [K_v] & [K_p] \\ [K_p]^T & [0] \end{pmatrix}_n \begin{pmatrix} \begin{bmatrix} v_x \\ v_y \end{bmatrix} \\ [p] \end{pmatrix}_n = \begin{pmatrix} [F] \\ [0] \end{pmatrix}_n \tag{2.38}$$

The individual contributions from each element are found through integration of the individual terms of the FEM expressions corresponding to the con-

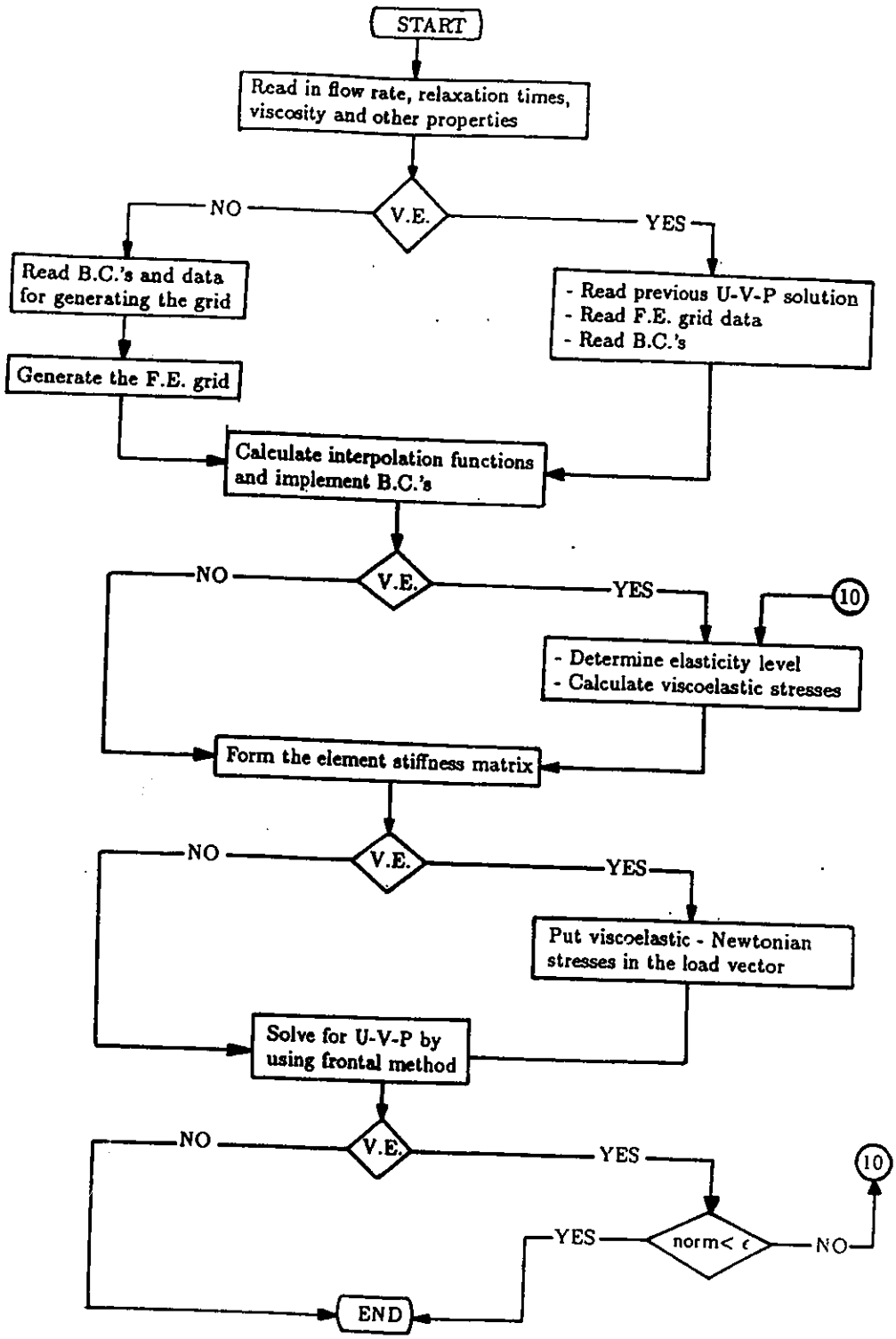

Figure 2.8: Flow sheet for the organization of main program (NACHOS).

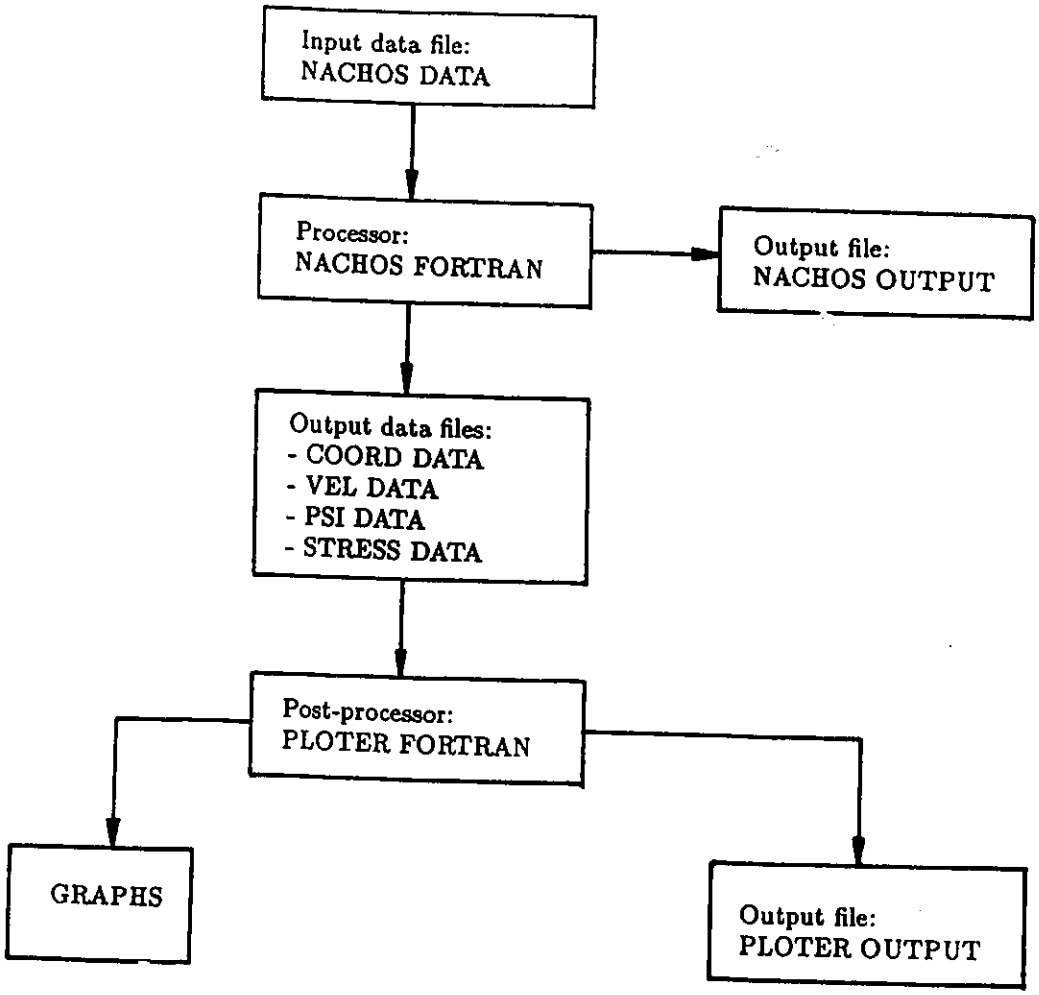

Figure 2.9: Flow sheet for the overall organization of all programs used.

servation equations. Together they produce a symmetric **stiffness matrix**, $[K]$, for each element n, with all contributions eventually added up and equated with the **load vector**, F, that contains body forces, surface tractions and boundary conditions. These algebraic equations can be solved by using a frontal method (subroutine UNZIP in NACHOS, Gartling, 1978; Luo, 1987).

In the presence of free surfaces the program regenerates the grid to account for the altered domain due to the inclusion of the free surface, and the process for $u - v - p$ solution is repeated. The iterative process stops when both the norm-of-the-error is below the prescribed tolerance and virtually no change is seen for the location of the free surface.

Computer time requirements for NACHOS vary due to various considerations such as number of iterations desired and the extent of intensity of the analysis. A denser grid will undoubtedly yield more precise data although the increase in CPU time required could make costs prohibitive. Therefore a balance must be struck between the two concerns.

NACHOS is a self-contained analysis program with its own mesh generator and data analysis, while plotting is done with a post-processor called PLOTER and using DISSPLA software. The data analysis portions of the code allow the stream function, local heat fluxes and fluid stresses (Newtonian or non-Newtonian) to be calculated. The plotting package provides graphic output of element meshes, nodal point locations, velocity and heat flux fields, and a variety of contour plots including streamlines, isobars, non-Newtonian stress and strain rate components, vorticity, viscous dissipation and isotherms. The NACHOS

program employs a save-and-restart procedure with a controlled increment in the elasticity level for the analysis of viscoelastic flows.

Chapter 3

Poiseuille Flow of Viscoelastic Fluids

Before proceeding with the numerical analysis of flow past a sphere, the finite element program was tested against some well-known analytical results for simple shear flow (Poiseuille flow) of viscoelastic fluids. The effect of the finite element mesh is examined on the results and the iterative process highlighted. Planar and axisymmetric geometries are considered with and without the presence of second normal stress difference, and the accuracy of the results is established.

3.1 Unidirectional Flow between Parallel Plates

A viscoelastic fluid between two parallel plates of length L and height 2H is being driven in the x-direction by a constant pressure gradient (see Figure 3.1). For the FEM analysis, the grid used consists of 16 quadrilateral elements, 81 nodes and 155 unknown degrees of freedom (d.o.f.) (9 nodes across, 9 nodes along the domain).

Figure 3.2 shows the finite element grid along with the boundary conditions. Because of the symmetry involved only half the domain need be considered. The

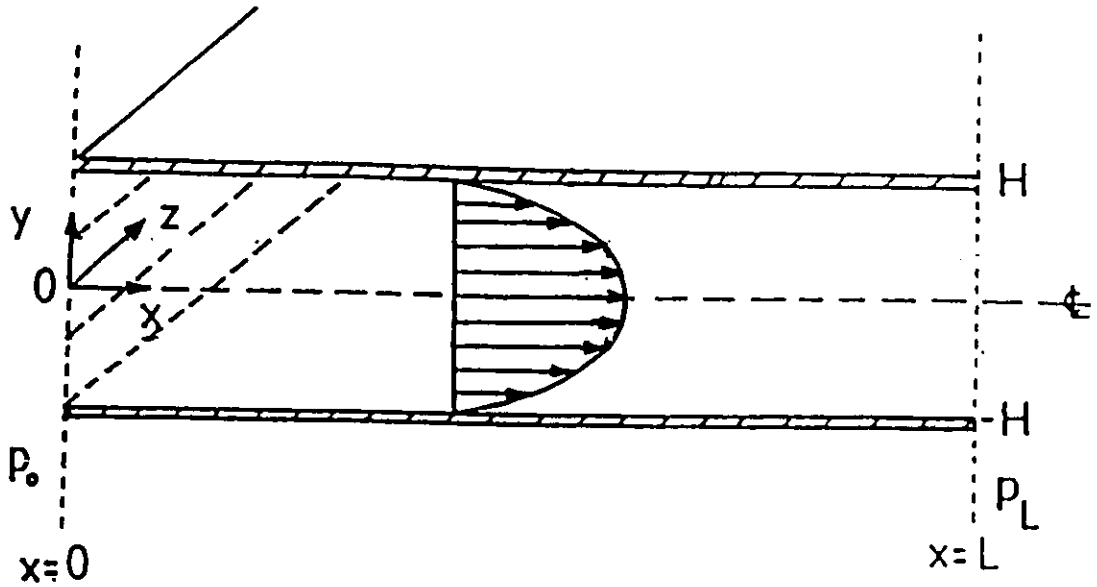

Figure 3.1: Pressure-driven Poiseuille flow in a planar slit with relevant notation.

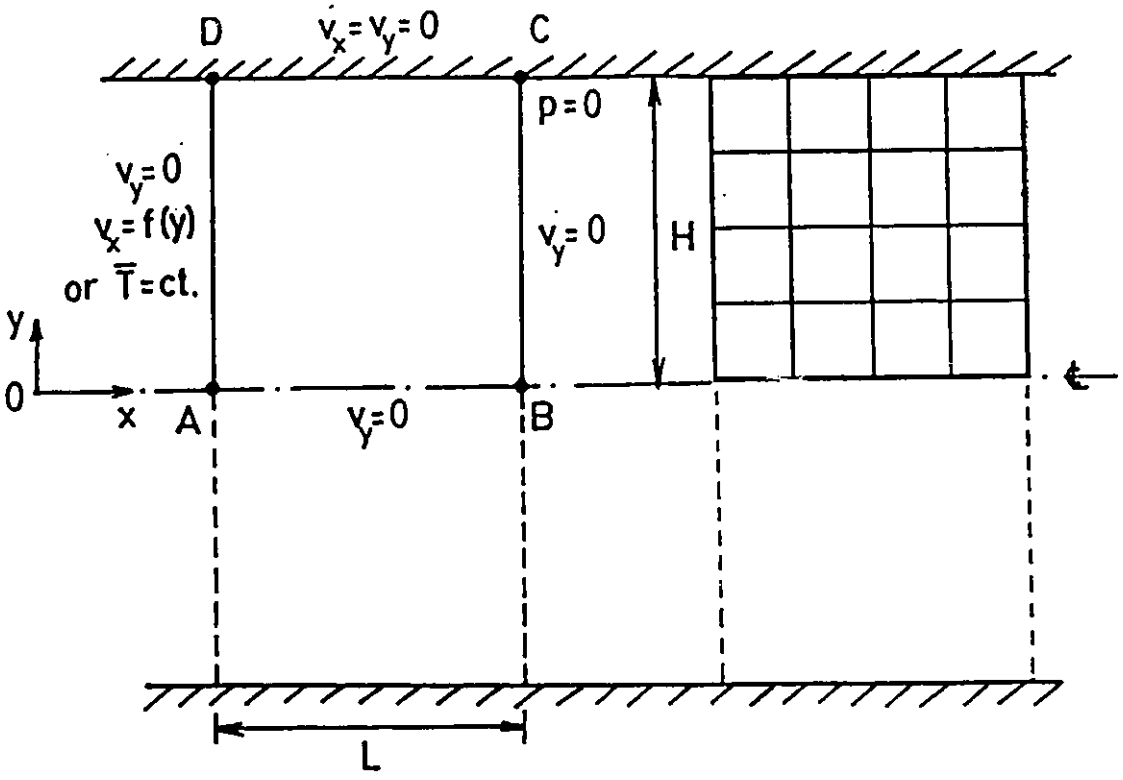

Figure 3.2: Boundary conditions in pressure-driven flow through a planar slit and finite element grid used in the computations.

boundary conditions are:

- on edge AD either a fully-developed profile v_x or a uniform surface traction $\bar{T}$ to account for the pressure forces acting on the material;
- on edge CD, $v_x = 0$ (no-slip condition at wall);
- on all four edges, $v_y = 0$;
- at an arbitrary point downstream (here at C), p=0.

The finite element iterative process starts from the Newtonian solution and using direct substitution (Picard method) proceeds to the viscoelastic solution. The numerical results obtained for the three models are presented here.

3.1.1 Maxwell Model

In this case, the upper-convected Maxwell integral constitutive equation (2.8) gives the same parabolic velocity profile as for Newtonian fluids, *i.e.*

$$v_x = V_{max}\left[1 - \left(\frac{y}{H}\right)^2\right] \tag{3.1a}$$

$$V_{max} = \frac{\Delta P H^2}{2\mu L} \tag{3.1b}$$

However, the viscoelastic stresses are given by:

$$\tau_{xx} = 2\left(\frac{1}{1-\theta}\right)\mu\lambda\dot{\gamma}^2 \tag{3.2a}$$

$$\tau_{yy} = 2\left(\frac{\theta}{1-\theta}\right)\mu\lambda\dot{\gamma}^2 \tag{3.2b}$$

$$\tau_{xy} = \mu\dot{\gamma} \tag{3.2c}$$

where $\dot{\gamma} = -\frac{dv_x}{dy}$ is the shear rate and is a linear function of y.

The shear stress at the wall (τ_w) is given by:

$$\tau_w = \mu\dot{\gamma}_w = 2\mu V_{max} \tag{3.3}$$

where $\dot{\gamma}_w$ is the wall shear rate ($\dot{\gamma}_w = -\frac{dv_x}{dy}$ at $y = H$), μ is the viscosity of the fluid, λ is the relaxation time and θ is the ratio of τ_{yy} to τ_{xx}, $i.e.$

$$\theta = \frac{\tau_{yy}}{\tau_{xx}} \tag{3.4}$$

The Maxwell model gives rise to the following viscometric functions:

The first normal stress difference N_1

$$N_1 = \tau_{xx} - \tau_{yy} = \Psi_1 \dot{\gamma}^2 \tag{3.5}$$

where Ψ_1 is the first normal stress difference coefficient

$$\Psi_1 = \frac{N_1}{\dot{\gamma}^2} = 2\mu\lambda \tag{3.6}$$

The second normal stress difference N_2

$$N_2 = \tau_{yy} - \tau_{zz} = \Psi_2 \dot{\gamma}^2 \tag{3.7}$$

where Ψ_2 is the second normal stress difference coefficient

$$\Psi_2 = \frac{N_2}{\dot{\gamma}^2} \tag{3.8}$$

Then:

$$\frac{N_2}{N_1} = \frac{\theta}{1-\theta} \tag{3.9}$$

The pressure difference between wall and centerline is then given by

$$\Delta P = P_w - P_{cl} = -\tau_{yy} = -\Psi_2 \dot{\gamma}^2 \tag{3.10}$$

For the solution all lengths have been normalized by H, all velocities by V_{max} and all pressures and stresses by $\mu\frac{V_{max}}{H}$. We have used $L = 1$, $H = 1$, $\mu = 1$ and

$V_{max} = 1$, while changing the relaxation time λ to reach higher elasticity levels, determined by the dimensionless Weissenberg number

$$Ws = \lambda \frac{V_{max}}{H} \tag{3.11}$$

The solution is shown in Figure 3.3, where the parabolic velocity profile (Figure 3.3a) and shear stress profile (Figure 3.3b) are compared with the analytical solutions (Equation 3.1a and 3.3). The agreement is exact. The pressure varies linearly in the x-direction (Figure 3.4a, b) in the absence ($\theta = 0$) or presence ($\theta \neq 0$) of a second normal stress difference. It is worthwhile to note that the total pressure drop in the axial direction remains the same with $\theta = 0$ and $\theta = -0.25$.

In the absence of a second normal stress difference ($\theta = 0$), the isobars are straight lines (Figure 3.4c), while in the presence of a second normal stress difference ($\theta = -0.25$) the isobars show a quadratic behaviour (Figure 3.4d). The contour values for the isobars are made dimensionless between 0 and 1 with increments of 0.1. The quadratic variation of the normal stress difference and the pressure are in agreement with Equations 3.5 and 3.10, respectively. This behaviour is demonstrated in Figure 3.5a,b for different Weissenberg numbers ($Ws = 0 - 2$).

3.1.2 Oldroyd-B Model

The expressions for the velocity and stresses are the same as for the Maxwell integral constitutive equation. In the case of Oldroyd-B fluid (Equation 2.10), $\mu = \mu_m$ except in Equation (3.2c) where $\mu = \mu_m + \mu_s$, and the expressions for

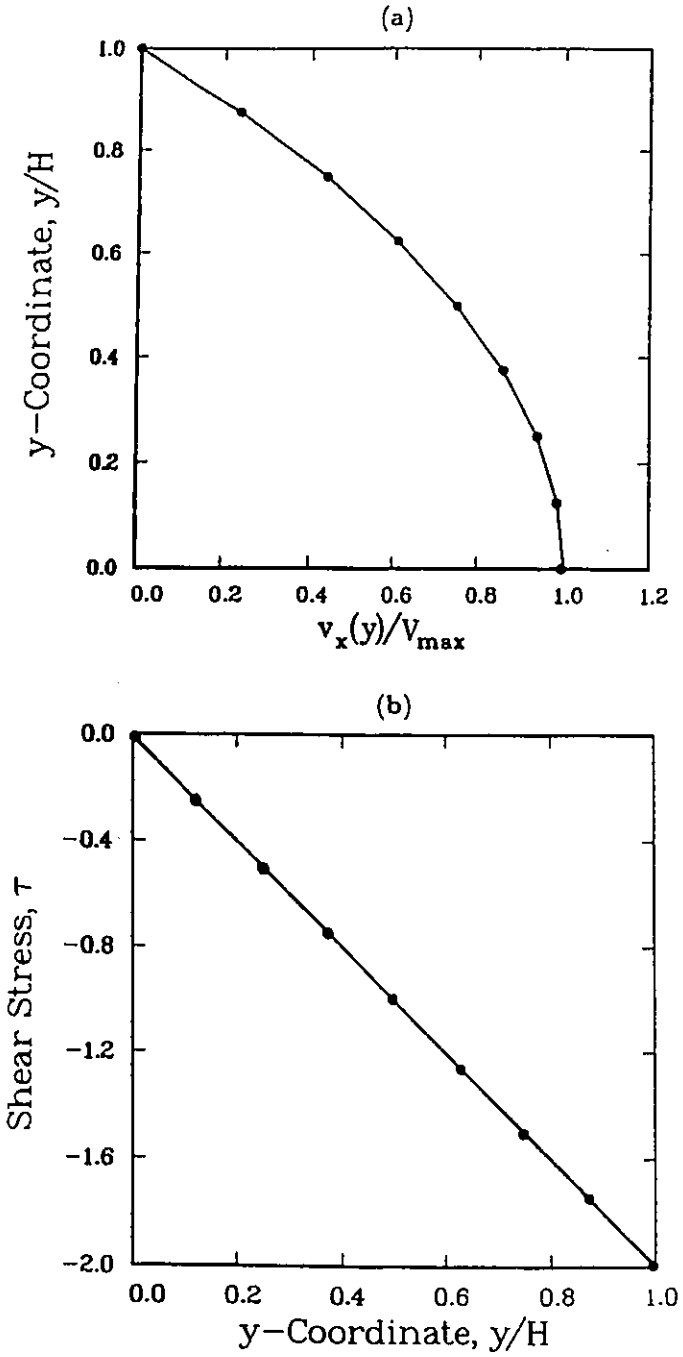

Figure 3.3: Comparison between the analytical solution (solid line) and numerical solution (symbols) in fully-developed pressure-driven flow of a viscoelastic fluid using the Maxwell model: (a) velocity profile for all Ws; (b) shear stress distribution as a function of y.

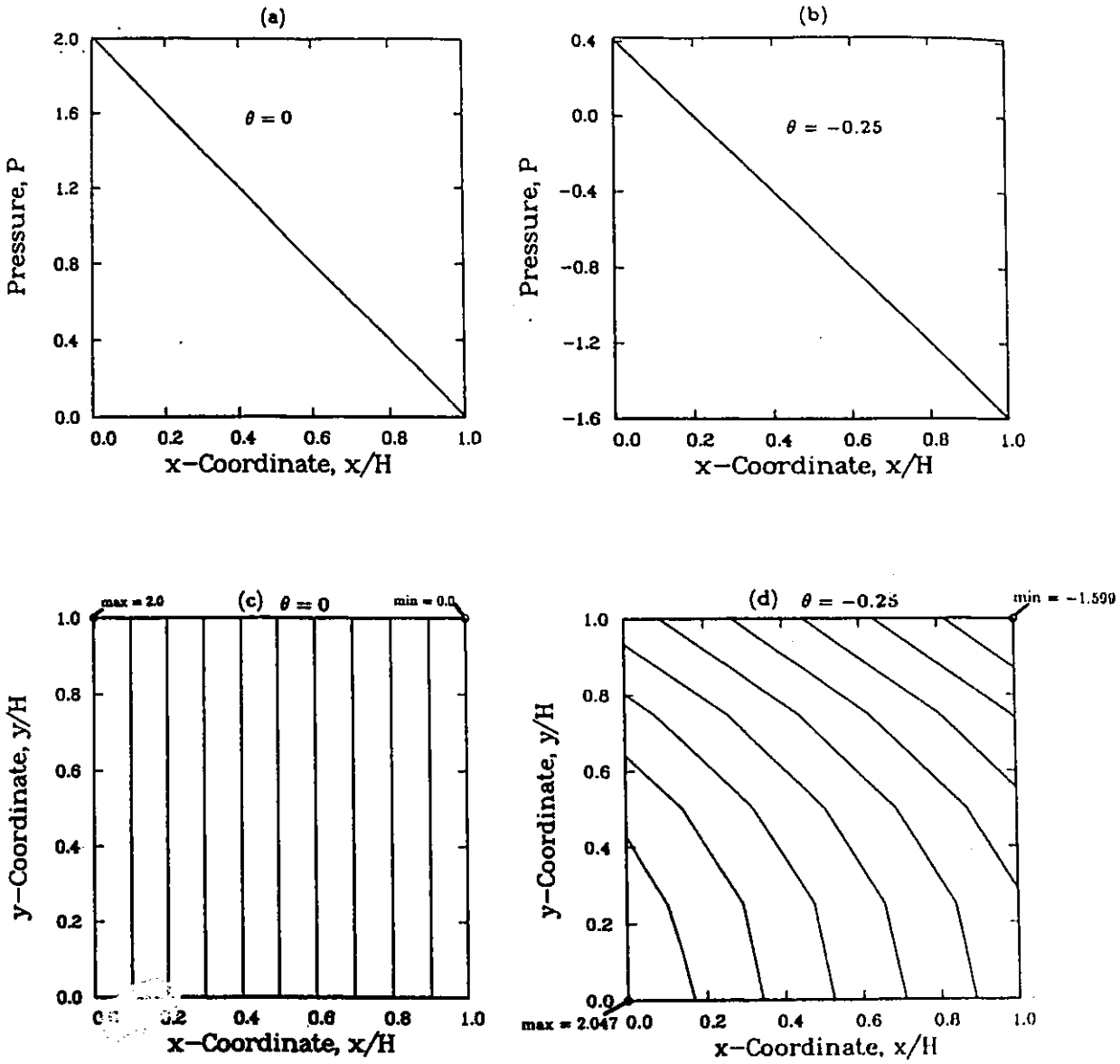

Figure 3.4: Pressure fields given by FEM solution in a pressure-driven flow of a viscoelastic fluid between parallel plates using the Maxwell model (Ws=1.0): (a,b) Axial pressure distribution at the wall (c,d) isobars.

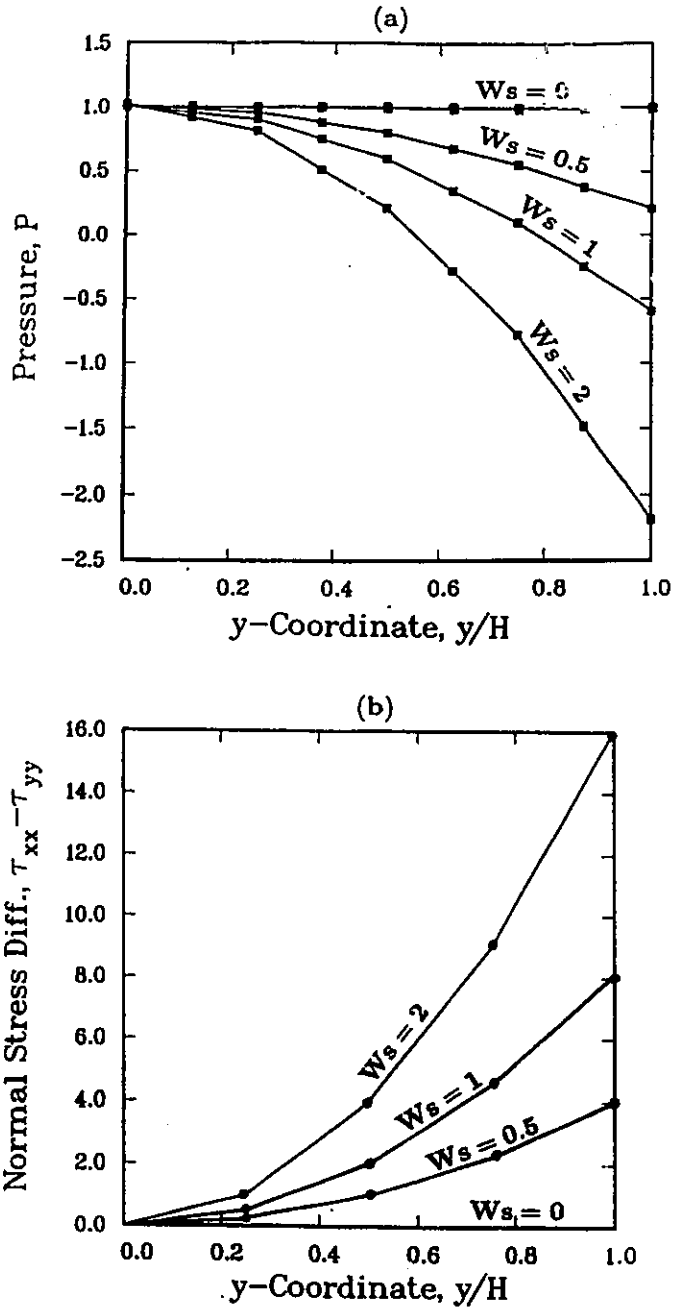

Figure 3.5: (a) Pressure and (b) normal stress difference distributions as a function of y for a viscoelastic fluid with $\theta = -0.25$ given by FEM solution in a pressure-driven flow between parallel plates using the Maxwell model for different Weissenberg numbers.

the normal stress differences and pressure are given by:

$$N_1 = \tau_{xx} - \tau_{yy} = \mu_m \Psi_1 \dot{\gamma}^2 \tag{3.11}$$

$$N_2 = \tau_{yy} - \tau_{zz} = \mu_m \Psi_2 \dot{\gamma}^2 \tag{3.12}$$

$$\Delta P = P_w - P_{cl} = -\mu_m \Psi_2 \dot{\gamma}^2 \tag{3.13}$$

For the solution of the Oldroyd-B model we have used $\mu_m = 8/9$, $\mu_s = 1/9$ and $\lambda_2 = \lambda_1/9$. For this model λ_1 was incremented to reach higher elasticity levels. In this case the Weissenberg number is given by

$$Ws = \lambda_1 \frac{V_{max}}{H} \tag{3.14}$$

The results obtained using the Oldroyd-B model are the same as those obtained using the Maxwell model except for the pressures and normal stress differences, which are presented in Figure 3.6. The Oldroyd-B model underpredicts the dimensionless pressure and normal stress difference as y increases from the centerline to the wall in the presence of a second normal stress difference by a factor of 8/9.

3.1.3 K-BKZ Model

Simple analytical expressions for the stresses by using the K-BKZ model (Equation 2.12) are not available due to the complicated nature of the model itself. However, the velocity profile is given by Equation (3.1a) with V_{max} given by Equation (3.1b). In an attempt to reduce the K-BKZ model to the upper-convected Maxwell model, a very big α value ($\alpha = 15000$) was used while β was set equal to zero. A single relaxation time was used and its corresponding

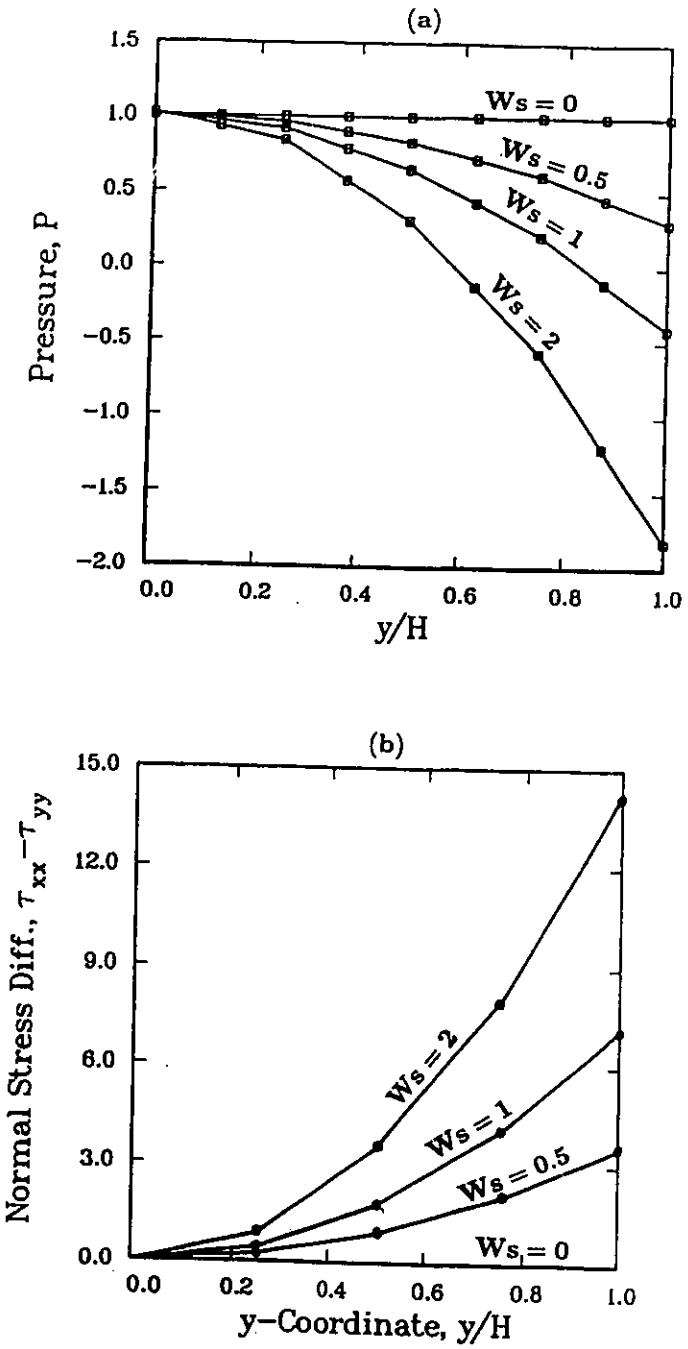

Figure 3.6: (a) Pressure and (b) normal stress difference distributions as a function of y for a viscoelastic fluid with $\theta = -0.25$ given by FEM solution in a pressure-driven flow between parallel plates using the Oldroyd-B model for different Wessenberg numbers.

relaxation modulus was set to 1.0. An average dimensionless velocity $\bar{v} = 0.5$ was used to give $V_{max} = 1.0$. The results obtained were indistinguishable with those predicted by the Maxwell model.

3.2 Axial Flow in a Circular Tube

A viscoelastic fluid flowing in a circular tube of radius R and length L is driven in the z-direction by a constant pressure gradient (Poiseuille flow in a tube, see Figure 3.1, where H is substituted by R and y by r).

For the FEM analysis, the same grid was used as before for the planar analysis. The boundary conditions are the same and the solution has been pursued for the same material data as before. The numerical results for the three integral models are presented below.

3.2.1 Maxwell Model

In this case, the upper-convected Maxwell constitutive equation (2.8) gives expressions for the shear stresses which are identical to the planar case, where $\tau_{zz} = \tau_{xx}$, $\tau_{rr} = \tau_{yy}$ and $\tau_{rz} = \tau_{xy}$. In general axisymmetric flows, an extra stress component ($\tau_{\theta\theta}$) appears, which for Poiseuille flow is zero everywhere.

The velocity distribution is the same as in Equation (3.1) with y replaced by r and H replaced by R, which corresponds to the parabolic equation for Newtonian fluids. The maximum velocity V_{max} is given by the usual expression

$$V_{max} = \frac{\Delta P R^2}{4\mu L} \tag{3.15}$$

The solution is presented in Figure 3.7, where the velocity profile is compared to

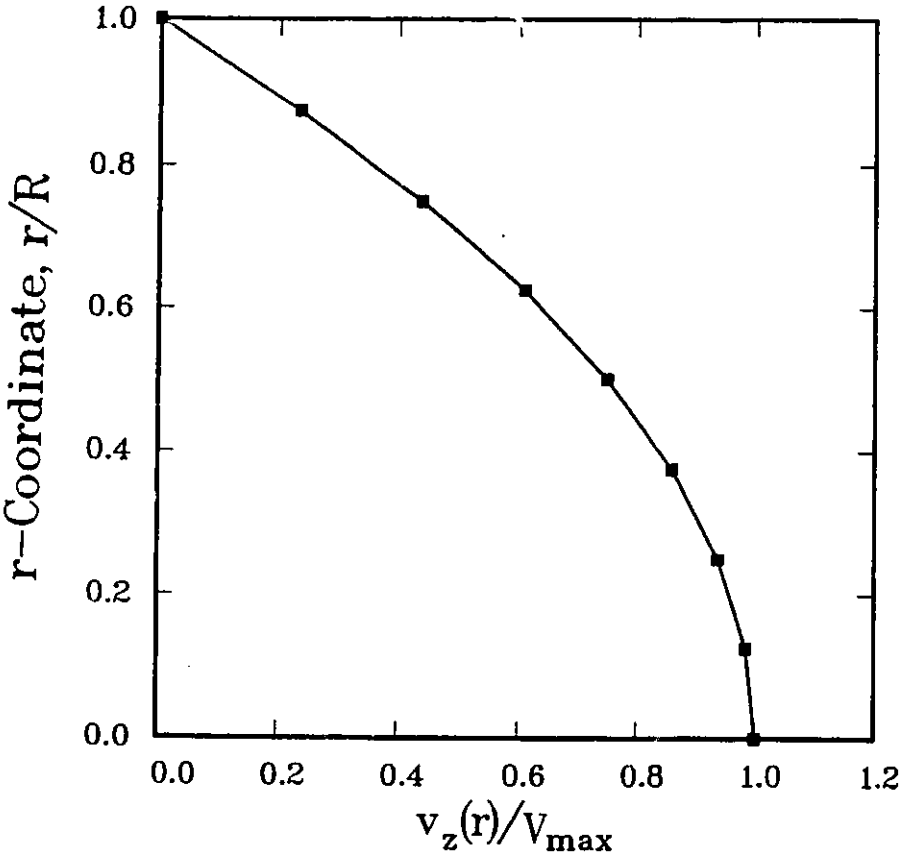

Figure 3.7: Comparison between the analytical solution (solid line) and numerical solution (symbols) for the velocity profile in fully-developed Poiseuille flow of a viscoelastic fluid in a tube using the Maxwell model ($Ws = 1$).

the analytical solution (Equation 3.1) with V_{max} given by Equation (3.15). The agreement is exact. The numerical results for the pressure distributions both in the presence and absence of a second normal stress difference are presented in Figure 3.8a and b. The pressure varies linearly in the z-direction, in a manner similar to the planar case (see Figure 3.4a). The shear stress for the axisymmetric flow was found to be the same as in the planar case (see Figure 3.3b). The total pressure drop was found to be in exact agreement with the analytical value of $\Delta P = 4.0$. The isobars demonstrated a behaviour similar to that of the planar case both in the presence and absence of a second normal stress difference. In the presence of a second normal stress difference ($\theta = -0.25$), the normal stresses (τ_{rr} *and* τ_{zz}) show a parabolic distribution in the radial direction (see Figure 3.8c and d), which is in agreement with Equations 3.2a and 3.2b. Similarly, the pressure and the normal stress difference show a parabolic profile (see Figure 3.9a and b), which is confirmed by Equations 3.7 and 3.10, respectively.

3.2.2 Oldroyd-B Model

The analytical expressions for the velocity and stresses are the same as for the Maxwell model for the axisymmetric case. The Oldroyd-B model requires that the viscosity μ be changed to μ_m for the normal stress expressions. The results obtained using the Oldroyd-B model are qualitatively the same as those obtained using the Maxwell model and they are presented in Figure 3.10.

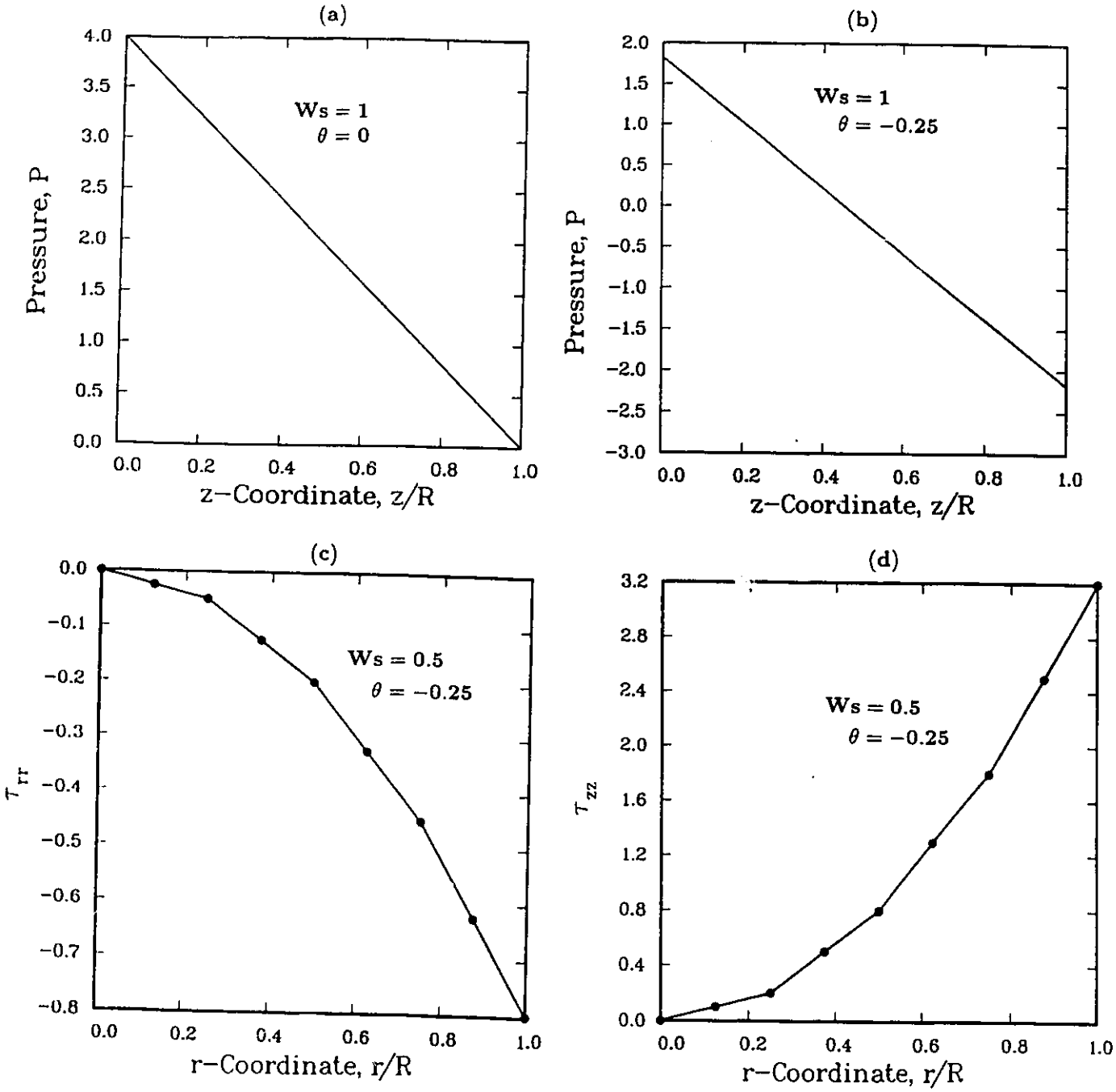

Figure 3.8: (a,b) Axial pressure (Ws=1); (c,d) normal stress distributions (Ws=0.5) given by FEM solution in a pressure-driven flow of a viscoelastic fluid in a tube using the Maxwell model.

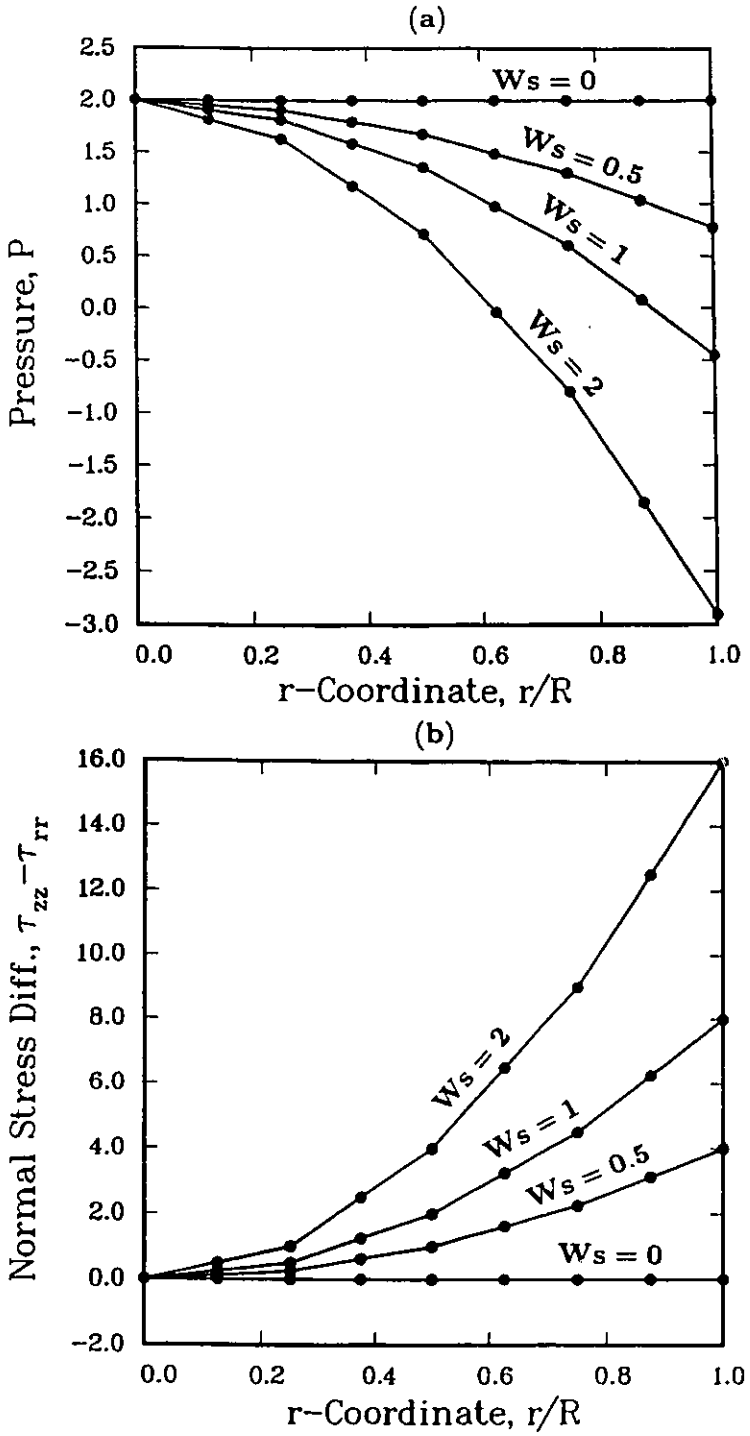

Figure 3.9: (a) Pressure and (b) normal stress difference distributions as a function of r for a Maxwell fluid with $\theta = -0.25$ given by FEM solution in a pressure-driven flow of a viscoelastic fluid in a tube using the Maxwell model for different Weissenberg numbers.

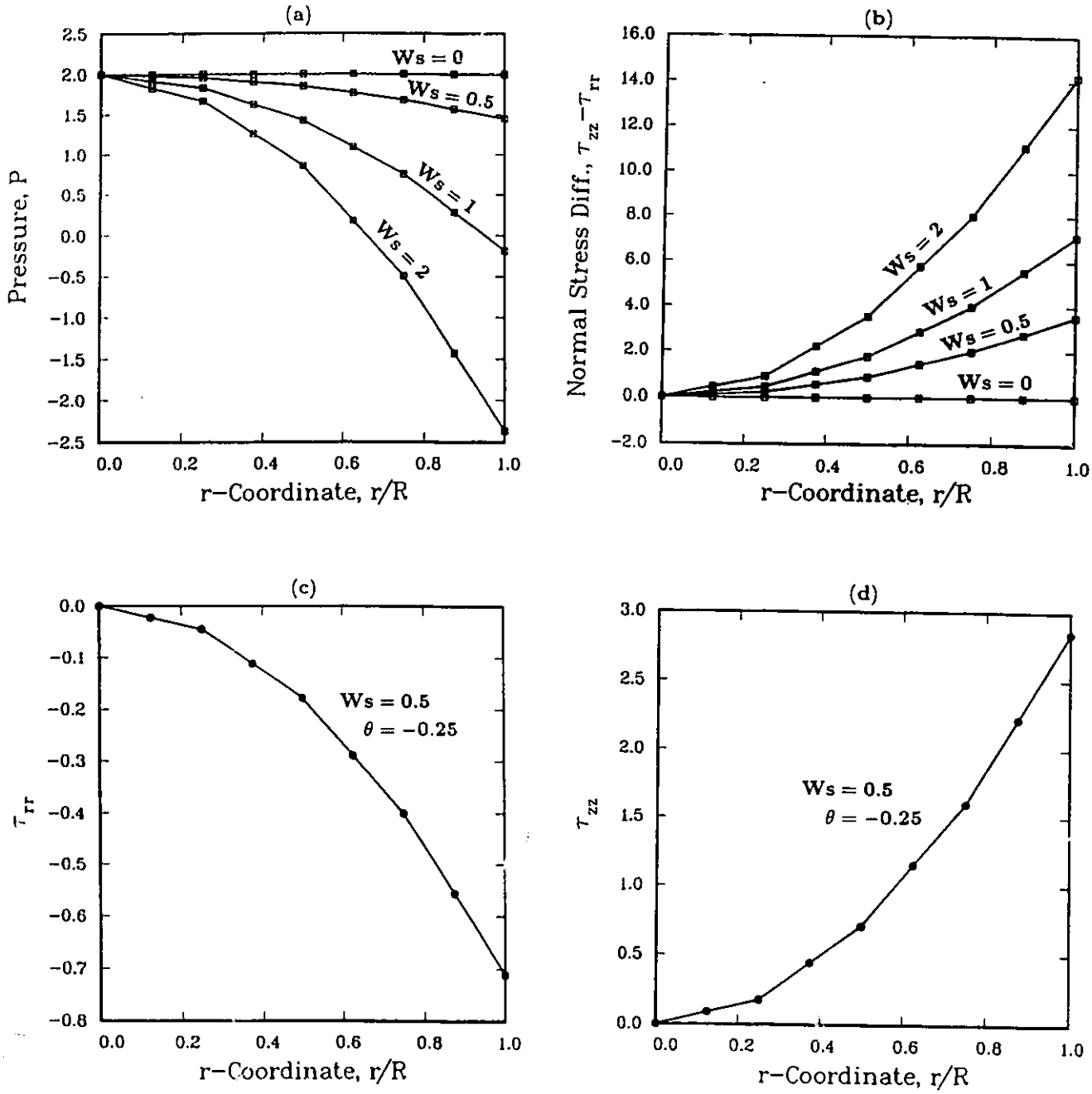

Figure 3.10: (a) Pressure and (b) normal stress difference distributions as a function of r; (c) and (d) normal stress distributions for Ws=0.5 for a viscoelastic fluid with $\theta = -0.25$ given by FEM solution in a pressure-driven flow of a viscoelastic fluid in a tube using the Oldroyd-B model.

3.2.3 K-BKZ Model

Simple analytical expressions for the K-BKZ model are not available due to the complicated nature of the model itself. However, the velocity profile is given by Equation (3.1a), where y/H is substituted by r/R, with V_{max} given by Equation (3.15). The same data as in the planar case were used to simulate the flow in the axisymmetric case for the K-BKZ model. The results obtained were similar as in the previous planar case.

3.3 Convergence Study of the Numerical Scheme

It is interesting to study the convergence of the numerical scheme for the different models, geometries and elasticity levels. For Ws=0, the Newtonian fluid is recovered (all relaxation times equal to zero), which is a linear problem and no iterations are needed. However, for Ws≠0, the problem is non-linear, and iterations are needed to obtain a converged solution. One expects that as Ws increases, the further the solution departs from its linear Newtonian counterpart and the more iterations are needed for convergence. Finally, when the elasticity level becomes high enough, a limiting Ws number is reached beyond which no convergence can be obtained.

The iterative sheme is successive substitution (Picard method), which is straightforward and does not require any extra manipulation of the solution. The convergence criteria used are the relative norm-of-the-error $\|e\|$ based only on velocities and given by

$$\|e\| = \frac{\|\Delta v_i\|}{\|v_i\|} \tag{3.16}$$

where $\|\Delta v_i\|$ is the norm of the differences in the velocities $v_i - v_{i-1}$ at the ith and $i-1$st iterations and $\|v_i\|$ is the norm of the velocity vector at the ith iteration.

Another criterion is the maximum difference of the velocities anywhere in the field recorded between the ith and $i-1$st iterations, *i.e.*

$$max|\Delta v_i| = max|v_i - v_{i-1}| \tag{3.17}$$

and the same is also done for the pressures for all nodes, *i.e.*

$$max|\Delta p_i| = max|p_i - p_{i-1}| \tag{3.18}$$

For the Maxwell fluid and with the finite element grid of Figure 3.2 consisting of 16 elements, the results for the planar and axisymmetric cases are given in Figure 3.11 for Ws=1.0. In all cases we start the solution process for a new Ws number from the previous solution obtained for a lower Ws number. It is seen that the planar case gives lower errors than the axisymmetric one with $\|e\|$ hovering around 10^{-10}, $max|\Delta v_i|$ around 10^{-9} and $max|\Delta p_i|$ around 10^{-7}. No clear convergence or divergence could be detected at Ws=1.0 although the axisymmetric case seems to show a small tendency for reducing the error in the velocities with increasing number of iterations.

For values of Ws=1.5 and Ws=2.0, a steady but clear divergence was occurring with errors slowly increasing with the number of iterations. Table 3.1 shows the findings for the cases examined. This diverging behaviour is

Table 3.1: Convergence behaviour of the Maxwell model in Poiseuille flow through parallel plates (planar geometry) and tubes (axisymmetric geometry). 16 elements have been used ($\theta = -0.25$).

Ws	N	$\|e\|$	$max\|\Delta v_i\|$	$max\|\Delta p_i\|$	Comment
		Planar			
1.0	10	$2.3\text{x}10^{-11}$	$4.8\text{x}10^{-10}$	$2.2\text{x}10^{-8}$	
1.5	10	$1.3\text{x}10^{-9}$	$1.6\text{x}10^{-8}$	$2.4\text{x}10^{-7}$	
1.5	20	$2.9\text{x}10^{-8}$	$3.3\text{x}10^{-7}$	$2.3\text{x}10^{-5}$	diverging
2.0	10	$9.8\text{x}10^{-9}$	$1.9\text{x}10^{-7}$	$1.7\text{x}10^{-5}$	diverging
		Axisymmetric			
1.0	10	$1.8\text{x}10^{-6}$	$6.5\text{x}10^{-6}$	$2.3\text{x}10^{-4}$	
1.0	20	$2.6\text{x}10^{-7}$	$3.7\text{x}10^{-6}$	$4.0\text{x}10^{-4}$	
1.5	10	$1.6\text{x}10^{-6}$	$1.9\text{x}10^{-5}$	$5.0\text{x}10^{-4}$	diverging
2.0	10	$7.5\text{x}10^{-4}$	$4.4\text{x}10^{-3}$	$2.5\text{x}10^{-1}$	diverging

hardly surprising, since it has been shown analytically for Poiseuille flow of a Maxwell fluid (Phan-Thien et al., 1991) that this model is unstable to infinitesimal disturbances, such as these occurring in a numerical simulation due to the round-off error inherent in every computer. The limiting Ws number is thus around 1 for this flow field.

The K-BKZ model with a spectrum of relaxation times was then studied for its convergence. To approach the Maxwell model as close as possible but still retain a relaxation spectrum, the parameters shown in Table 3.2 were used. These correspond to a truncated relaxation spectrum for a high-density polyethylene (HDPE) melt, which normally has 8 relaxation times and modulus coefficients and $\alpha = 8$.

Table 3.2: Material parameter values used in the K-BKZ model for convergence study ($\alpha = 15000,\ \beta = 0.5,\ \theta = -0.25, k = 4$)

k	$\lambda_k(s)$	$a_k(Pa)$
1	$1.0\text{x}10^{-4}$	$3.0\text{x}10^{5}$
2	$1.0\text{x}10^{-3}$	$1.5\text{x}10^{5}$
3	$1.0\text{x}10^{-2}$	$5.0\text{x}10^{4}$
4	$1.0\text{x}10^{-1}$	$2.0\text{x}10^{4}$

The convergence characteristics are given in Figure 3.11 for $Ws = 1.38$, and for all cases the results are summarized in Table 3.3. It is seen that a clear monotonic convergence is obtained for all 3 error criteria. This was also the case up to Ws=2.0, which seems to be the limiting number for this flow field. It should be also noted that in industrial practice the limiting Ws numbers hardly exceed 2 before breakdown of the polymer occurs.

Table 3.3: Convergence behaviour of the K-BKZ model in Poiseuille flow through parallel plates (planar geometry) and tubes (axisymmetric geometry). 16 elements have been used (constants are given in Table 3.2).

Ws	N	$\|e\|$	$max\|\Delta v_i\|$	$max\|\Delta p_i\|$	Comment
		Planar			
0.23	5	$6.3\text{x}10^{-11}$	$3.0\text{x}10^{-10}$	$7.3\text{x}10^{-8}$	
0.46	15	$5.2\text{x}10^{-9}$	$3.7\text{x}10^{-8}$	$6.0\text{x}10^{-7}$	
0.92	24	$2.4\text{x}10^{-9}$	$4.3\text{x}10^{-8}$	$5.0\text{x}10^{-7}$	
1.38	31	$2.7\text{x}10^{-9}$	$7.8\text{x}10^{-8}$	$9.6\text{x}10^{-7}$	
1.84	40	$5.7\text{x}10^{-9}$	$8.1\text{x}10^{-7}$	$6.1\text{x}10^{-5}$	
2.30	20	$7.2\text{x}10^{-6}$	$1.3\text{x}10^{-3}$	$8.6\text{x}10^{-2}$	diverging
		Axisymmetric			
1.84	10	$9.4\text{x}10^{-10}$	$1.5\text{x}10^{-7}$	$1.6\text{x}10^{-5}$	

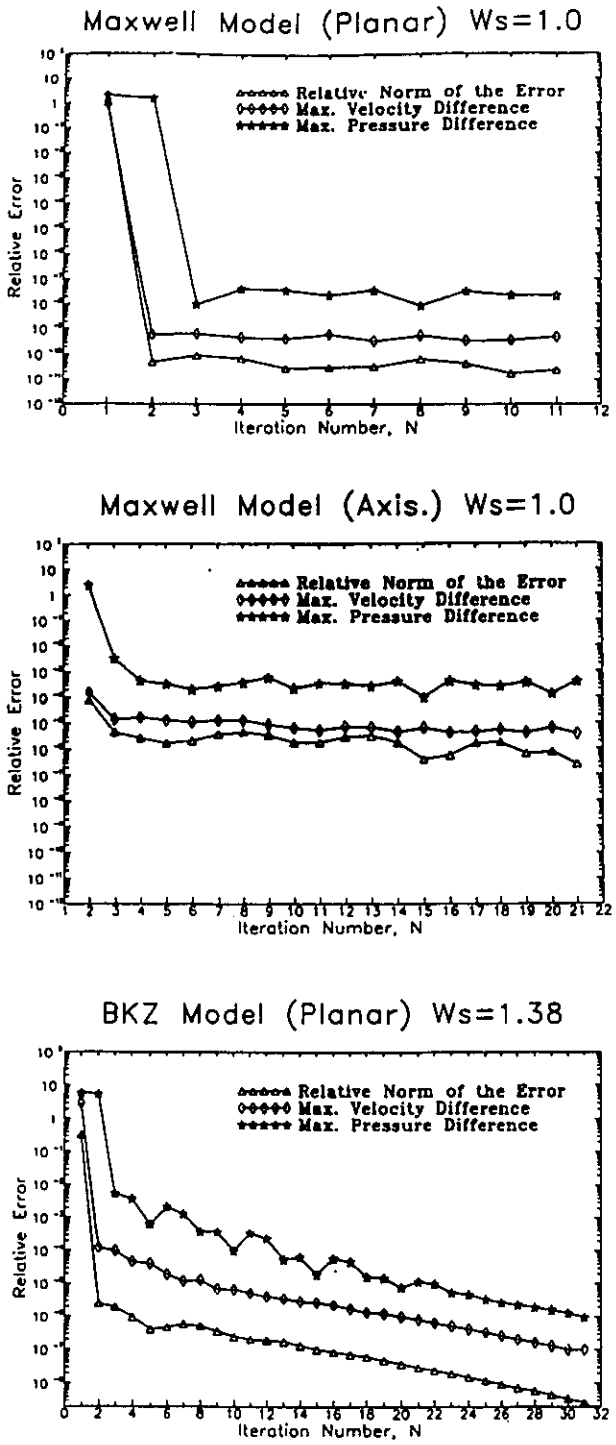

Figure 3.11: Convergence behaviour of Maxwell and K-BKZ models in different geometries.

Chapter 4

Flow around a Sphere Contained in a Cylinder (2:1 Diameter Ratio)

In this chapter, the finite element program will be used for solving a benchmark problem (flow around a sphere in a cylinder with a 2:1 diameter ratio) for which numerical results exist in the literature. The effects of mesh density and element arrangement will be discussed. Finally, the drag coefficient will be calculated at different elasticity levels by using the integral Maxwell constitutive equation. These results will be presented along with pertinent results from the literature to establish the accuracy of the present numerical scheme and domain discretization.

4.1 Introduction

The uniform flow of a viscoelastic fluid past a sphere of radius R contained in a cylinder with radius R_c (see Figure 4.1) is a situation which has received much attention in the field of non-Newtonian fluid mechanics. The particular case of a diameter ratio 2:1, *i.e.* flow around a sphere in a cylinder with strong wall

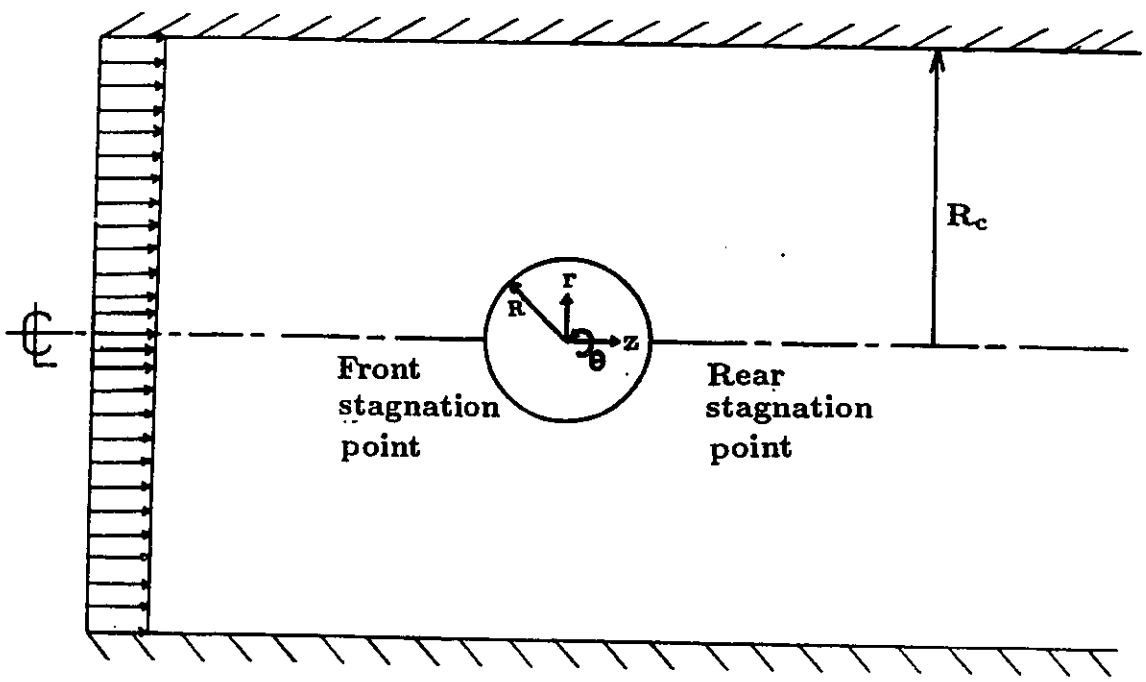

Figure 4.1: Schematic diagram of the flow past a sphere contained in a cylinder.

effects, was marked as a test problem about a decade ago (Caswell, 1983) for the Fourth International Workshop on Numerical Methods in Viscoelastic Flows held in Spa, Belgium, in 1985.

In the early stages, a major subject of interest had been the relative effects of shear-thinning and elastic behaviour on the drag force experienced by the sphere. Most real fluids possess both these properties and the individual contributions

from each were not identified.

Numerically, several attempts have been made to deal with the sphere problem with significant wall effects. Hassager and Bisgaard (1983) used the Lagrangian finite element method to simulate the flow of an upper-convected Maxwell liquid around a rigid sphere moving axially in a cylinder. One consequence of the Lagrangian formulation is that any simulation necessarily becomes an initial-value problem. At the onset of the simulation the location of all particles as well as the entire past history of deformation (often the rest history) are assumed known and the flow is then simulated forward in time. Their simulation showed that the drag correction factor for a sphere with strong wall effects is a rapidly decreasing function of the Deborah number ($De = \lambda\dot{\gamma}_a$), while the drag correction factor for a sphere in a very wide cylinder was not significantly affected by fluid elasticity (see Figure 4.2). Sugeng and Tanner (1986) have applied a Boundary Element Method (BEM) to deal with this problem by using the Phan-Thien-Tanner (PTT) model (Phan-Thien and Tanner, 1987), which can be reduced to the differential form of the upper-convected differential Maxwell model. Their results showed a quadratic decrease departing from the Newtonian solution for Ws<0.05 and an exponential decrease for Ws>0.05. Luo and Tanner (1986) have applied a Streamline Finite Element Method (SFEM) by using the differential upper-convected Maxwell model and have arrived to similar conclusions as those by Hassager and Bisgaard (1983).

Experimentally, Bisgaard (1983) used a Laser-Doppler Anemometer (LDA) technique to obtain a detailed description of the flow field and measure the veloc-

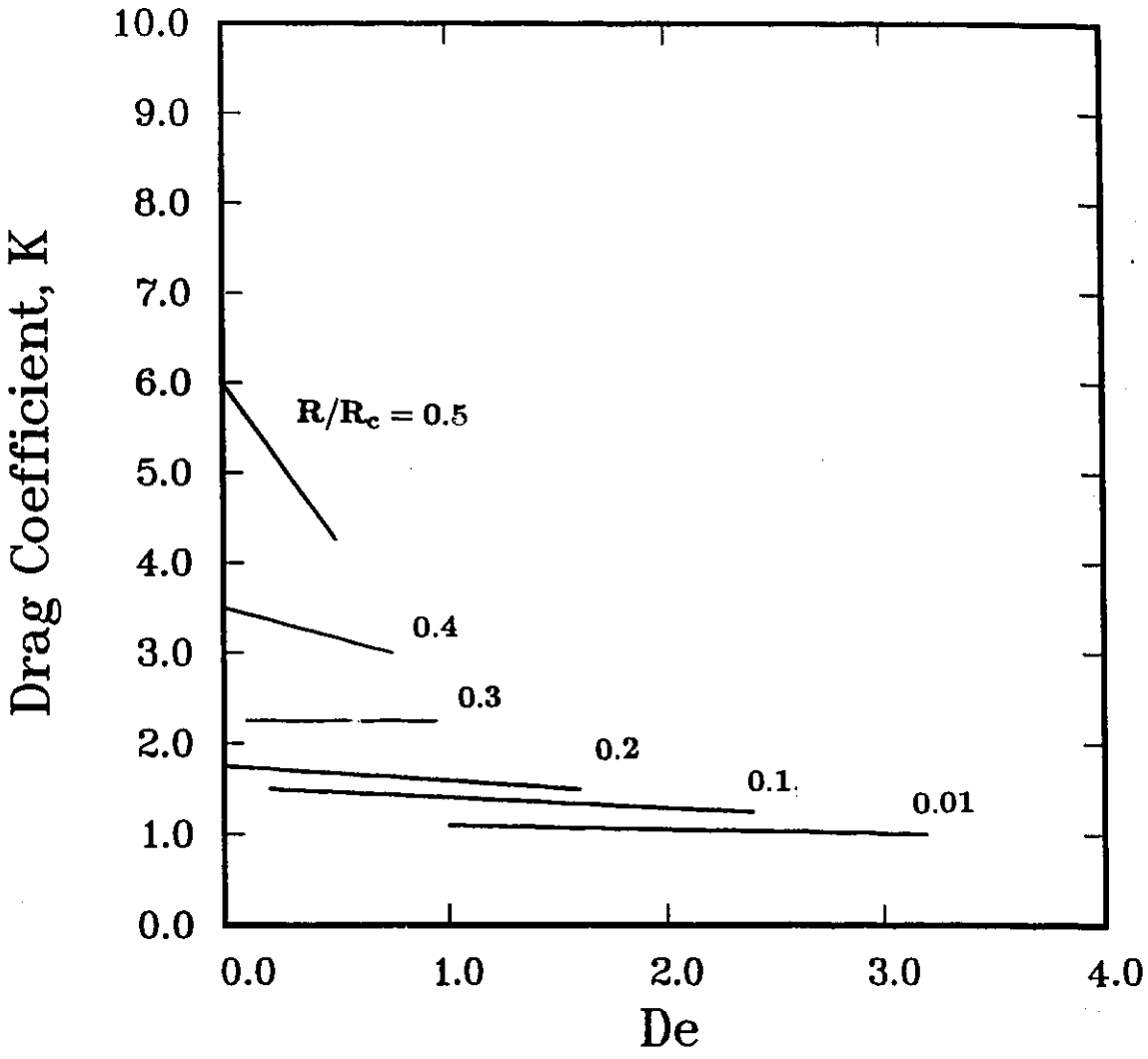

Figure 4.2: Lagrangian simulation results using the upper-convected Maxwell model for the drag coefficient K as a function of Deborah number for various values of R/R_c (Hassager and Bisgaard, 1983).

ity fields around spheres and bubbles. This technique was applied for different cylinder-to-sphere diameter ratios, and good agreement was obtained with his numerical findings mentioned above (see Figure 4.3).

The common overall prediction of these analysis is a drag reduction that depends on the Deborah number, which represents the ratio between the characteristic time of the fluid and the characteristic time of the flow. For our numerical computations the corresponding integral Maxwell constitutive equation will be used to solve the benchmark problem discussed previously.

4.2 Newtonian Flows

For the creeping flow of Newtonian fluids, *i.e.* for very low Reynolds numbers, the underlying theory is well established due to Happel and Brenner (1973). Stokes' law, which is expressed as

$$D_\infty = 6\pi R\mu V \tag{4.1}$$

gives the drag force on a sphere of radius R moving with a constant velocity V in an unbounded fluid. In the case that the sphere is moving along the centreline of a cylindrical tube, the Stokes' drag D is a function of sphere to cylinder radius ratio (R/R_c) and can be estimated from the value of the unbounded case using a method of reflections. The most well-known approximate result by this method, due to Bohlin (Happel and Brenner, 1973), is

$$\begin{aligned} K = \frac{D}{D_\infty} &= \Big[1.0 - 2.10444(R/R_c) + 2.08877(R/R_c)^3 - 0.94813(R/R_c)^5 \\ &\quad -1.372(R/R_c)^6 + 3.87(R/R_c)^8 - 4.19(R/R_c)^{10}\Big]^{-1} \end{aligned} \tag{4.2}$$

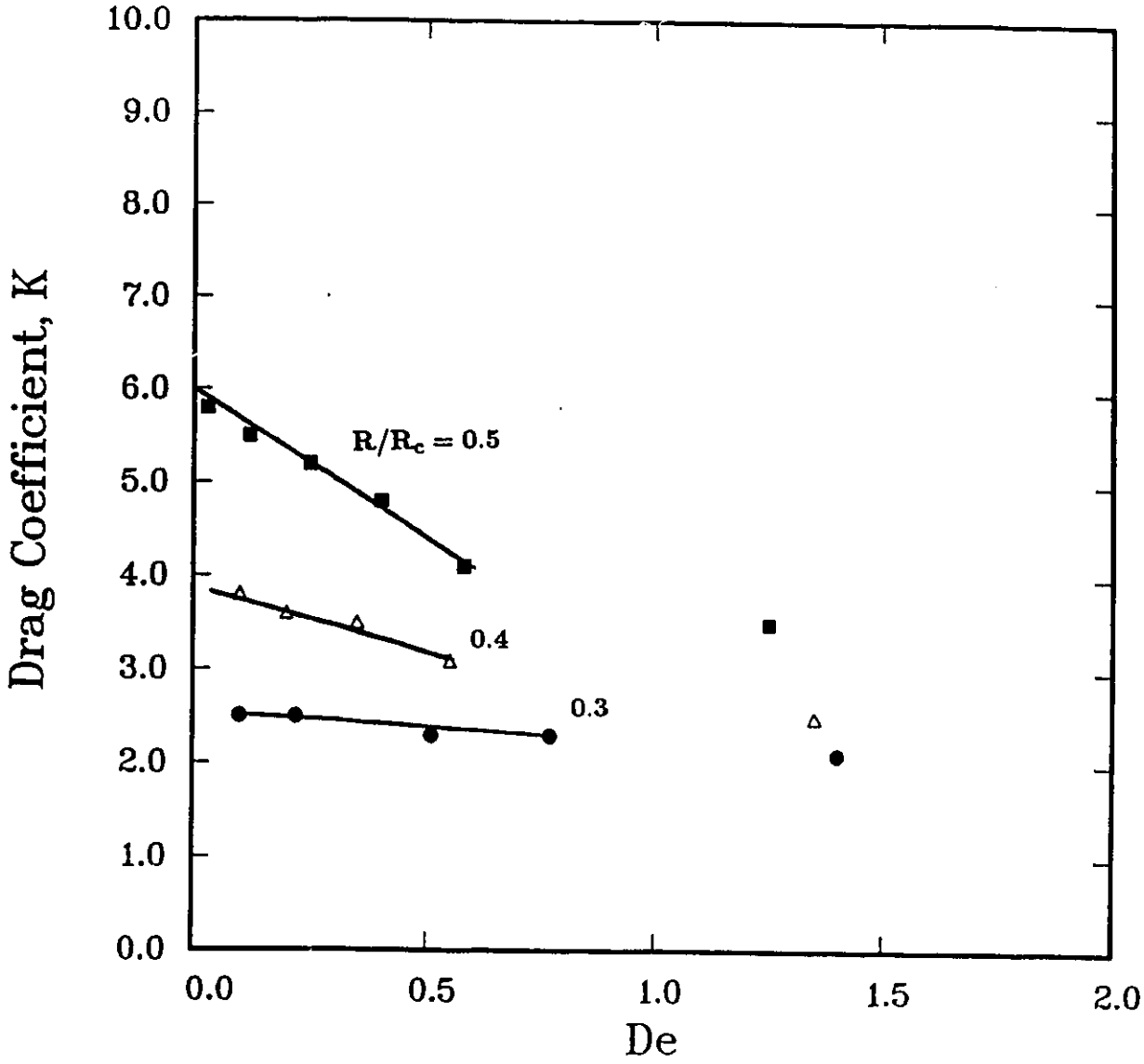

Figure 4.3: Experimental data (symbols) for the drag coefficient K for a 1% solution of polyacrylamide in glycerine at $20°C$ compared with finite element solutions for the upper-convected Maxwell model with parameters $\mu = 21.0$ Pa.s and $\lambda = 12.0$ s (Bisgaard, 1983).

where K is the drag coefficient, R is the sphere radius and R_c is the cylinder radius.

Most studies concerning Newtonian wall effects have been well documented in the literature (Happel and Brenner, 1965; Clift et al., 1978; Zheng et al., 1991). For our numerical computations the drag force is computed by integrating the tractions over the sphere surface. The calculation scheme is presented in Appendix B.

4.2.1 Boundary Conditions

The flow geometry used for our numerical computations is presented in Figure 4.4. Let L_u, L_d be the lengths upstream and downstream of the sphere center, respectively. The sphere has a radius of R and the container cylinder a radius $R_c = 2R$. For our calculations, we have chosen the ratios L_u/R and L_d/R to be 6 and 6, respectively, as done previously by other researchers (Harlen, 1990; Zheng et al., 1990; Zheng et al., 1991).

The boundary conditions for the flow geometry depicted in Figure 4.4, are as follows:

(1) At the entry of the flow domain ($z = -L_u$), plug flow conditions are applied, where the axial velocity $v_z = V$ and the radial velocity $v_r = 0$;

(2) Along the tube wall (r=R), $v_z = V$ and $v_r = 0$;

(3) Along the centerline (r=0), symmetry boundary conditions apply, where $v_r = 0$ and the axial traction is set to zero;

(4) On the surface of the sphere, no slip condition is applied, $v_z = v_r = 0$;

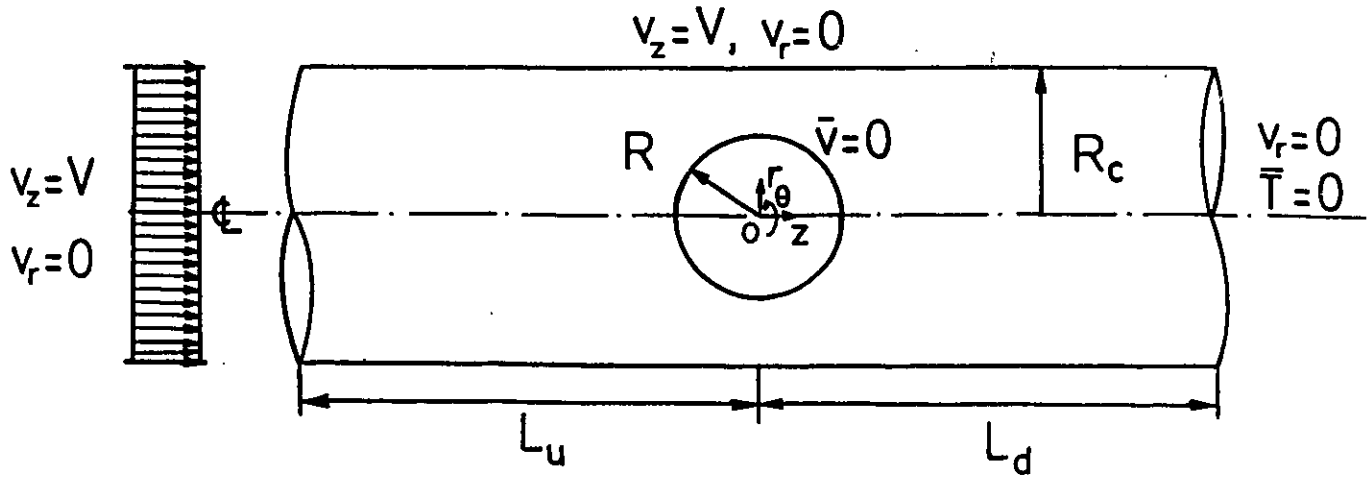

Figure 4.4: Schematic diagram of the flow past a sphere contained in a cylinder and boundary conditions.

(5) At the outlet of the flow domain ($z = L_d$), the axial traction is set to zero (no net force action on the fluid), and the radial velocity $v_r = 0$.

These boundary conditions apply both for Newtonian and non-Newtonian flow simulations.

4.2.2 Results and Discussion

It is well-known that the accuracy of numerical computations depends mainly on mesh refinement and a systematic mesh generation, which requires the physical understanding of the flow domain. The latter is purely intuitive and comes with experience. For example, for flows around spheres and for accurate drag calculations, the flow domain that must be closely captured remains in the vicinity of the surface of the sphere.

Three different meshes were used for evaluation purposes and these are presented in Figure 4.5. In particular:

(1) MESH1 has more elements in the radial direction and very sparse elements before and after the front and rear stagnation points, respectively. Straight lines of constant slope were used to generate the elements in the radial direction.

(2) MESH2 has more elements around the sphere and grows sparser from the front and rear stagnation points towards the entry and the exit, respectively. Also, straight lines of constant slope were used to generate the elements in the radial direction.

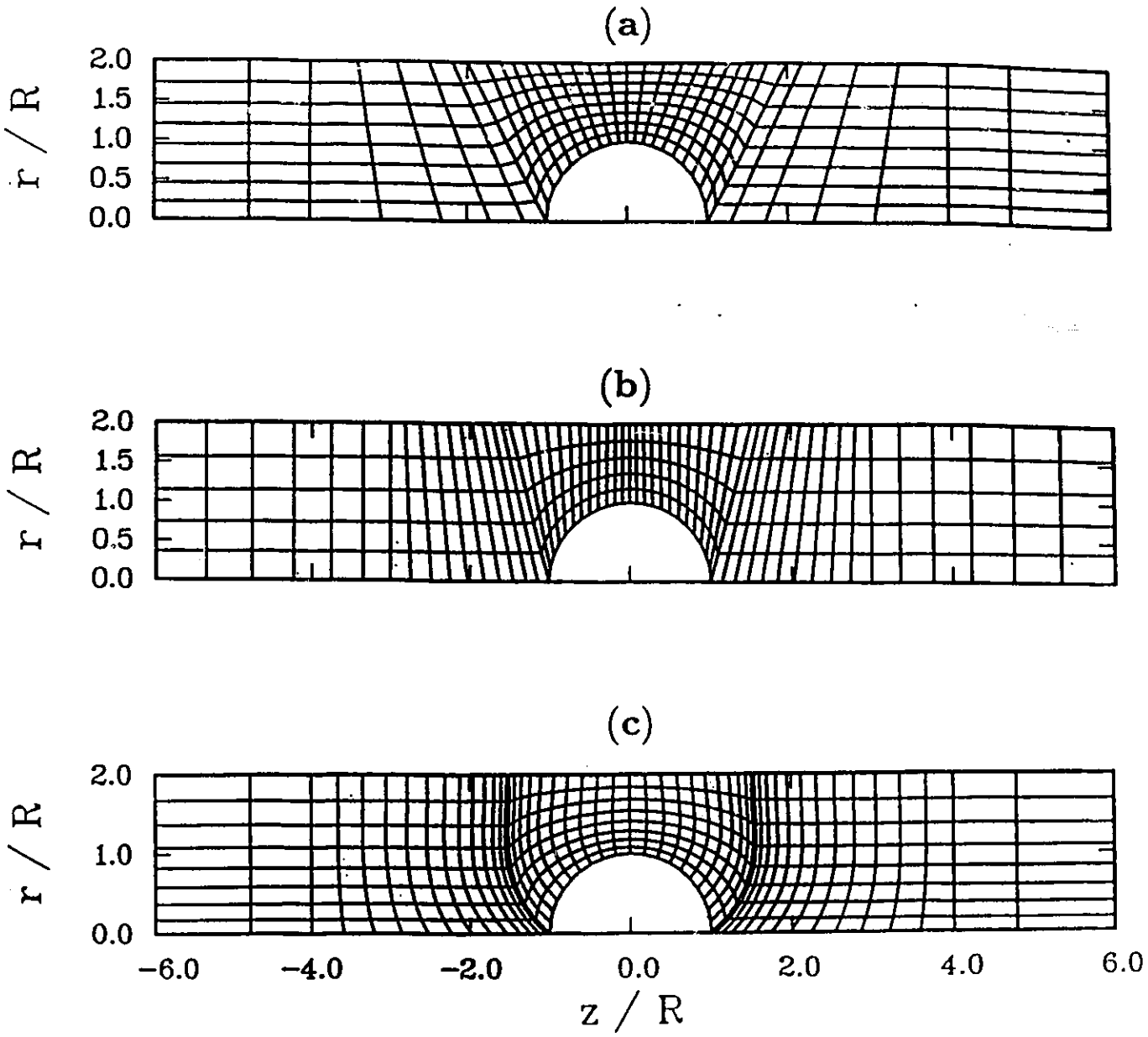

Figure 4.5: Finite element meshes used in the calculations: (a) MESH1, (b) MESH2, (c) MESH3.

(3) MESH3 has the same number of elements in the radial direction as MESH1 and one row of elements less in the horizontal direction than MESH2. The lines in the radial direction are curved so that the elements (nodal points) are evenly distributed around the sphere. Special care has been taken to discretize the region around the front and rear stagnation points by minimizing the nodal spacing both in the radial and axial directions.

In order to get the curved lines in the radial direction, 12 coordinates were used to define each isoparametric quadrilateral serendipity element. In all three meshes, less elements were assigned near the entry and exit because drastic changes are not expected to happen in these regions (plug flow). The upstream and downstream lengths, L_u and L_d, were so chosen as mentioned in section 4.2.2 because these lengths have been proved (Luo, 1987) to be long enough for very accurate drag calculations in the Newtonian case and also long enough to ensure, in a numerical sense, a stress-free region both upstream and downstream in the case of the Maxwell model (Luo, 1987).

A summary of the characteristics of the finite element meshes [number of elements, nodes, and degrees of freedom (DOF)] used for the numerical computations and the calculated Newtonian drag coefficients are shown in Table 4.1. The results show a decrease in the drag coefficient (K) with an increase in the number of elements. This trend has also been confirmed by Tanner (1990), who showed that by using FEM the calculated drag coefficient approaches the value of 5.9470 asymptotically from higher

Table 4.1: Summary of the finite element meshes used for the calculations and corresponding values of the drag coefficient K for Newtonian fluids flowing around a sphere in a tube ($R_c/R = 2:1$)

Name	Elements	Nodes	DOF	K
MESH1	272	901	2117	5.9724
MESH2	280	963	2296	5.9667
MESH3	400	1317	3093	5.9522

values, while using BEM an asymptotic aproach to the same value has been observed from lower values. The calculated value of the Newtonian drag was found to be 5.9522, which is about 0.08% in error from the asymptotic value.

The Newtonian flow results around spheres produce patterns which are symmetric upstream and downstream from the center of the sphere surface (see Figure 4.6). The axial velocity v_z and the velocity gradient $\partial v_z/\partial z$ along the axis of symmetry are plotted in Figure 4.7. The upstream and downstream velocity coincide. The velocity gradients are antisymmetric (mirror images).

The pressure, shear stress and normal stress difference distributions in the direction of flow are presented in Figure 4.8. The pressure increases drastically in the vicinity of the front stagnation point where it reaches its maximum at the front stagnation point. This is followed by a very sharp decrease below zero where it reaches its minimum at the rear stagnation point. The pressure goes to zero shortly after the rear stagnation point. Some authors reported the maximum value of the first normal stress difference $\tau_{zz} - \tau_{rr}$ just downstream

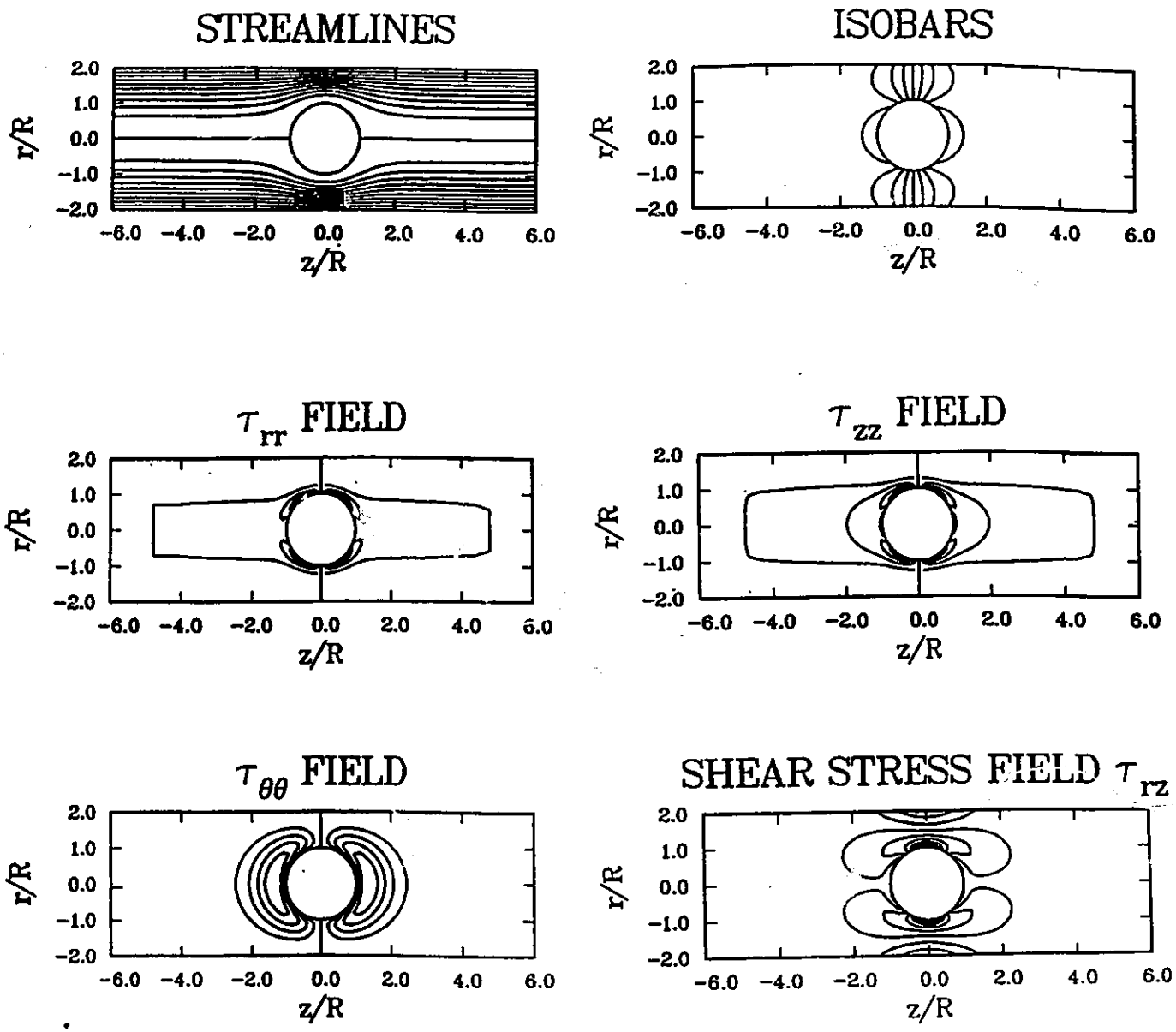

Figure 4.6: Newtonian results using MESH3: All values are normalized between 0 and 1 with increments of 0.1 in between.

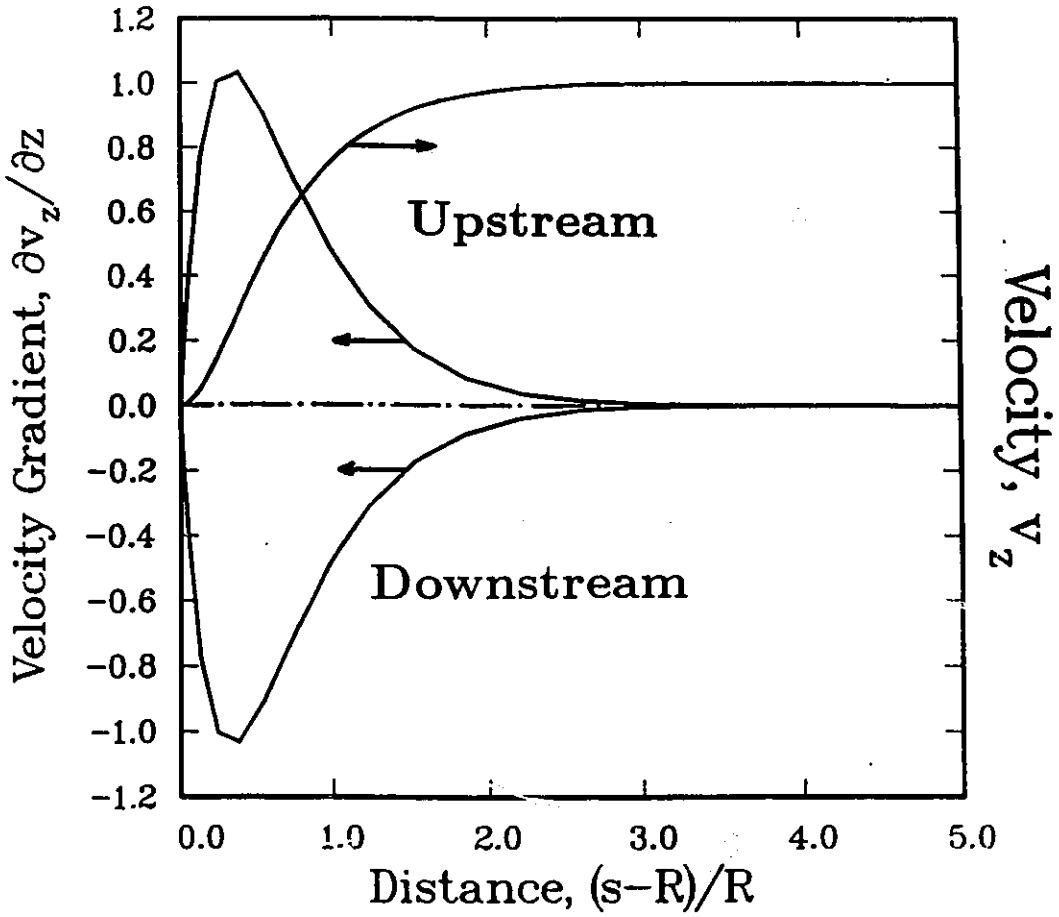

Figure 4.7: Axial velocity v_z and velocity gradient $\partial v_z/\partial z$ along the axis of symmetry as a function of s, where s is the distance from the sphere center for the Newtonian fluid using MESH3 ($R_c/R = 2:1$).

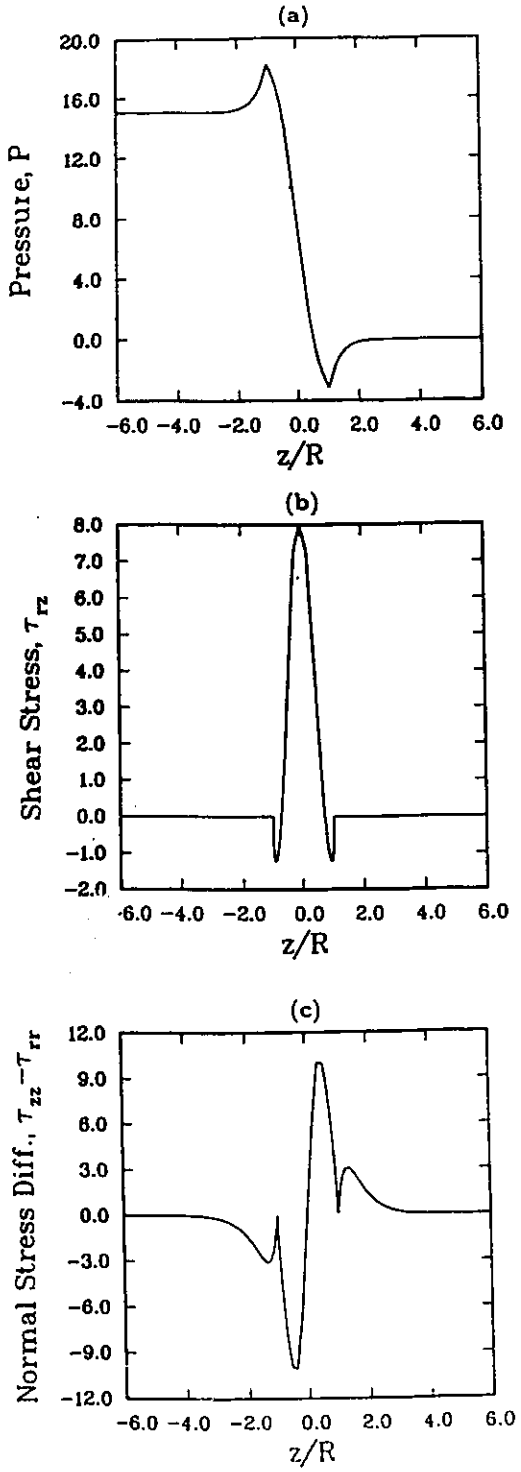

Figure 4.8: Newtonian results for pressure, shear stress and normal stress difference distributions along the axis of symmetry and on the sphere surface using MESH3 ($R_c/R = 2:1$).

of the rear stagnation point. Sugeng and Tanner (1986) found the value to be about 3.7; Luo and Tanner (1986) found about 2.9, while Carew and Townsend (1988) gave 4.0. In this work a maximum $\tau_{zz} - \tau_{rr}$ of 3.101 was obtained which is close to 2.957 found by Zheng et al. (1990) for a very dense grid (1130 domain cells).

4.3 Viscoelastic Flows (Maxwell Model)

Viscoelastic simulations have been undertaken only by using the Maxwell model and for a 2:1 cylinder/sphere diameter ratio. This is because previous numerical results exist in the literature for this particular geometry since its conception as a benchmark problem.

To obtain results for viscoelastic flows, MESH3 was chosen as being the densest. The same boundary conditions apply for the non-Newtonian flow as for the Newtonian. The Newtonian solution was used as an initial estimate. The solution obtained at a particular Weissenberg number was then used as an initial estimate to reach higher Weissenberg numbers. This process was carried out through a save-restart scheme until a limiting Weissenberg number occurred ($We_{limit} = 0.3$ for our FEM scheme).

The axial velocity v_z and velocity gradient $\partial v_z/\partial z$ along the axis of symmetry for $We = 0.3$ are shown in Figure 4.9. The upper curve of the velocity distribution represents the Newtonian upstream and downstream profiles as well as the Maxwellian profile upstream. The present results for the velocity and velocity gradients are also compared with published results (Zheng et al., 1990). The

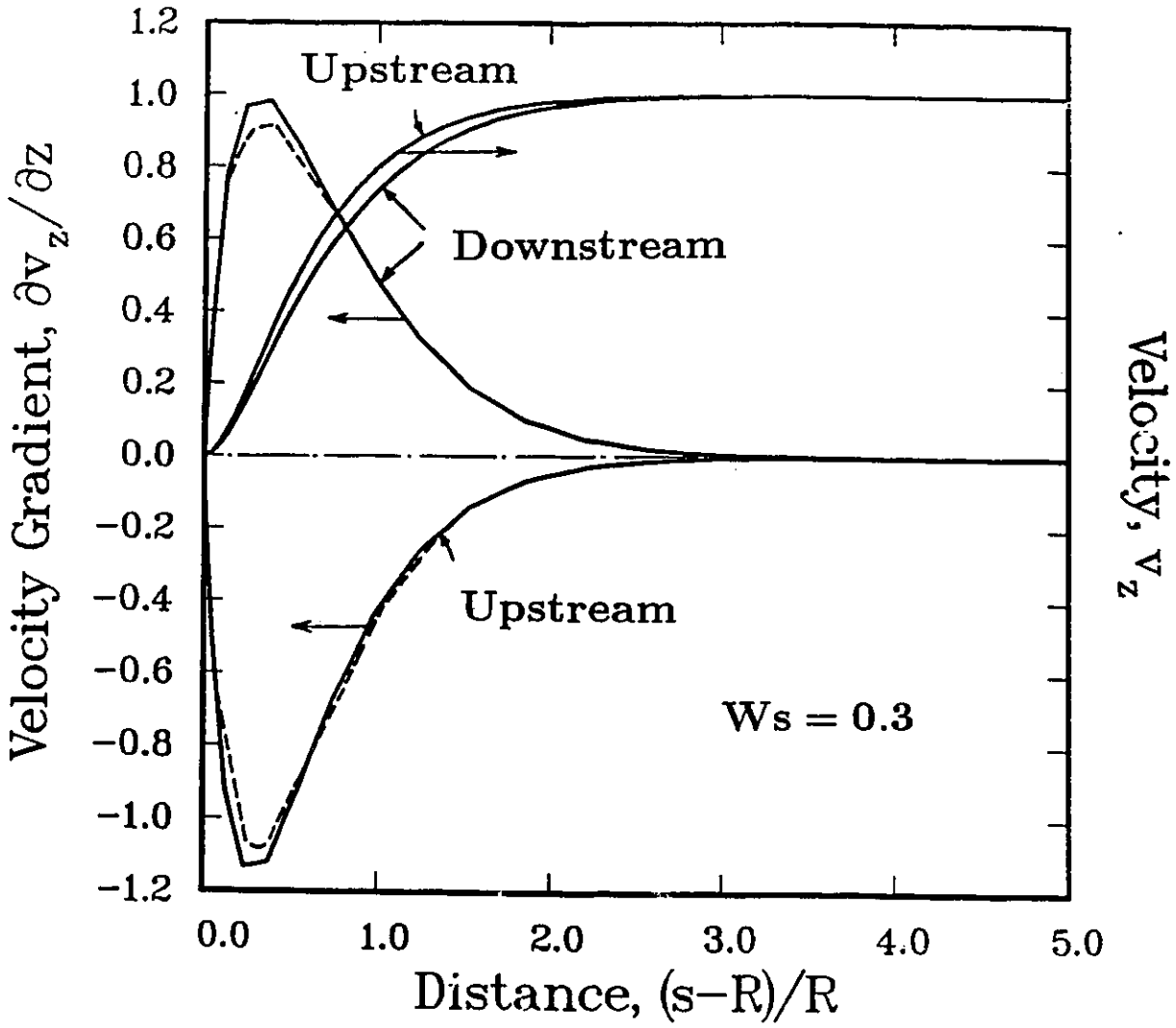

Figure 4.9: Axial velocity v_z and velocity gradient $\partial v_z/\partial z$ along the axis of symmetry and on the sphere surface as a function of s for the Maxwell fluid at $Ws = 0.3$ ---Zheng et al. (1990); ——present results using MESH3.

velocity distribution was in very close agreement, while the present results for the velocity gradients were slightly higher than the ones previously published. A slight downstream shift from the Newtonian case (Figure 4.7) in the velocity distribution is observed for the Maxwell model. This downstream shift is in the opposite direction to the experimental data reported by Sigli and Coutanceau (1977). This brings into question the ability of the Maxwell model to represent real fluids.

The results for the Maxwell fluid compared with the Newtonian results for the pressure, shear stress and normal stress difference are presented in Figure 4.10. The shear stress is plotted from the front stagnation point to the rear stagnation point around the sphere surface because the shear stress is zero everywhere away from this region along the centerline.

At Ws=0.3 the pressure indicates a wiggle at the front stagnation point, which is a sign of a numerical instability at this Ws number (see Figure 4.10a). The shear stress distribution at Ws=0.3 reaches its maximum earlier than in the Newtonian case (Figure 4.10b). The normal stress difference at Ws=0.3 shows a maximum 67% higher than the Newtonian (Figure 4.10c). This indicates that large tensile stresses are being developed at the sphere surface.

The plots of the first normal stress difference N_1 along the axis of symmetry and on the sphere surface as a function of the distance s from the center of the sphere are presented in Figure 4.11. Compared with the symmetric Newtonian curve, the curve for the upper-convected Maxwell model shows a significant downstream shift. The difference from the Newtonian value is greater in the

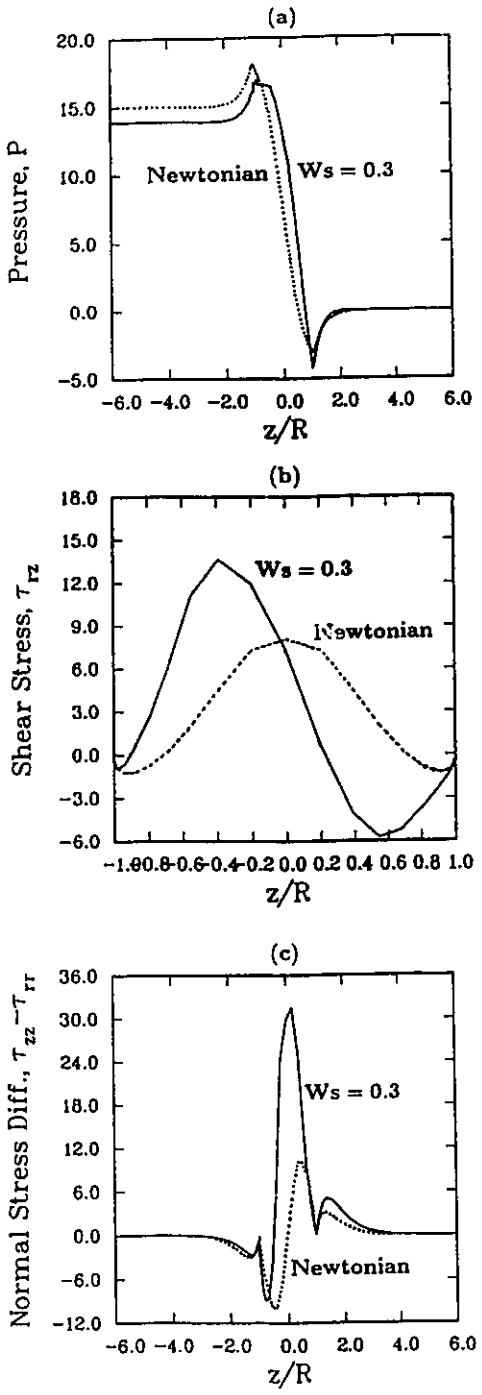

Figure 4.10: Comparison between a Newtonian fluid and the Maxwell fluid flowing past a sphere in a cylinder (2:1 ratio) at Ws=0.3. Distributions along the sphere surface and along the centerline for (a) pressure, (b) τ_{rz}, (c) $N_1 = \tau_{zz} - \tau_{rr}$ using MESH3.

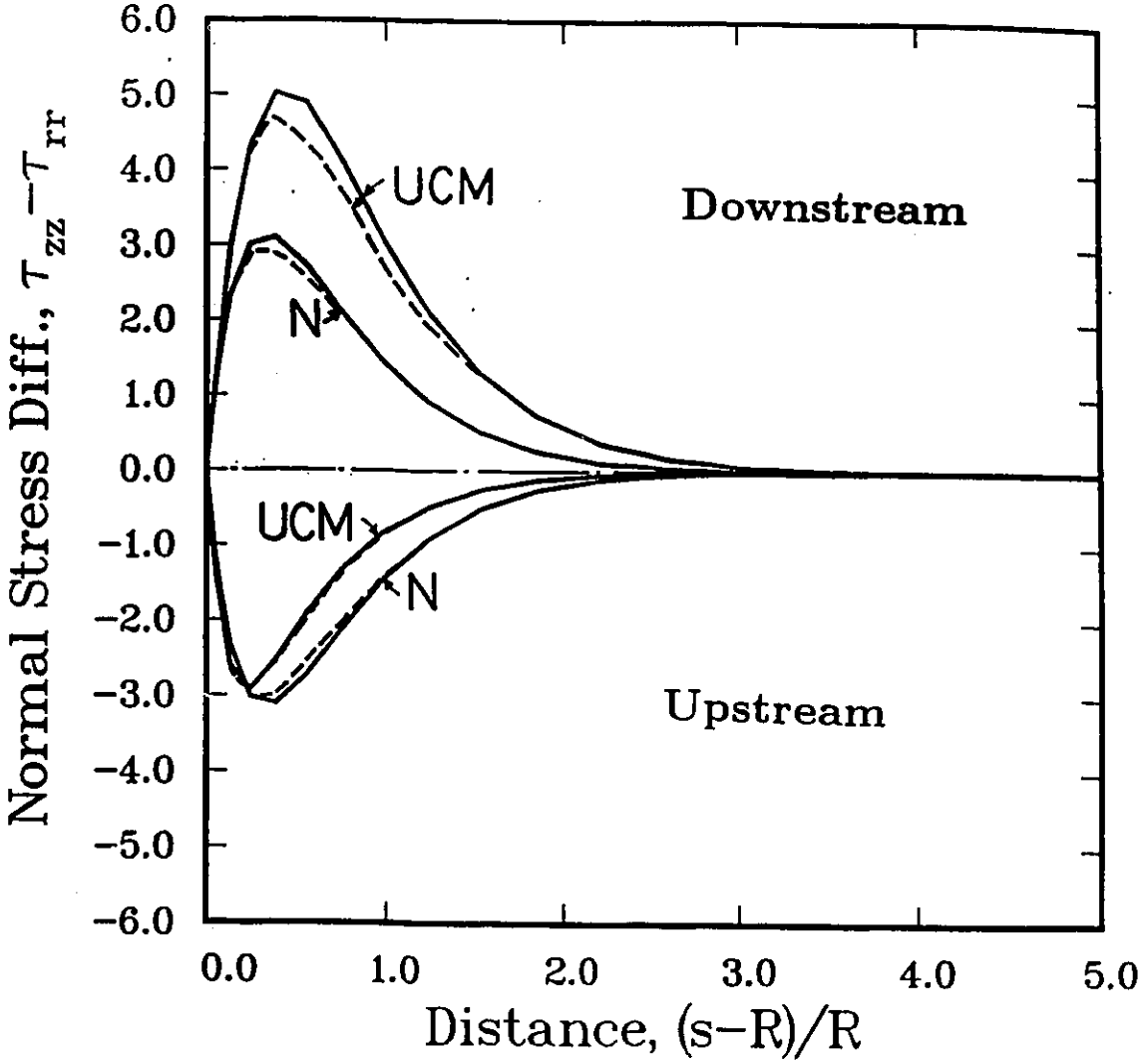

Figure 4.11: First normal stress difference $N_1 = \tau_{zz} - \tau_{rr}$ as a function of s for the Maxwell fluid at $Ws = 0.3$ ---Zheng et al. (1990); ——— present results using MESH3.

downstream region than in the upstream region. It also shows that away from the sphere, the Maxwellian stresses go to zero very quickly in a similar manner as in the Newtonian case. It is worth noting that at the upstream and downstream stagnation points (s=R) the Maxwellian stresses vanish. This can easily be shown in the Newtonian case by simply considering the flow kinematics at the stagnation points. Phan-Thien (1983b) obtained an exact solution to the axisymmetric stagnation flow of a Maxwellian fluid and found that the flow kinematics are exactly Newtonian.

The present results are in good agreement with those of Zheng et al. (1990), Sugeng and Tanner (1986), Luo and Tanner (1986) and Carew and Townsend (1988). At Ws=0.3, the present results show a slightly higher value than those of Zheng et al. (1990) because of differences in the number of elements and also because convergent results were difficult to obtain at this Weissenberg number, which was the limiting number for our scheme.

Drag coefficient calculations were made with and without the presence of the second normal stress difference, N_2. The results obtained are presented in Table 4.2. Figure 4.12 shows the dimensionless drag results using the integral upper-convected Maxwell model for this work along with other published works, which have used its differential counterpart. From Figure 4.12, it is evident that there is an overall agreement between the different numerical methods in predicting a drag reduction with increasing Weissenberg number. Most of these results are in a much better agreement at low Weissenberg numbers ($Ws < 0.5$) but the discrepancy broadens with increased Weissenberg number. At low

Table 4.2: Drag of Maxwell fluid on a sphere in a tube (2:1 ratio) using MESH3 at different elasticity levels

Ws	$\theta = 0$	$\theta = -0.25$
0.0	5.9522	5.9522
0.1	5.8529	5.8250
0.2	5.6784	5.6143
0.25	5.5641	5.4818
0.3	5.4935	5.3557

Weissenberg numbers the simulations predict a concave curve. The discrepancy of the drag coefficient K obtained in this study and between other researchers can be attributed to the different numerical techniques used, the number of elements used to discretize the flow domain and the type of the constitutive model used in the numerical scheme. These differences can play a vital role in the convergence and hence on the limiting value of the Ws. For most numerical techniques reported in the literature, with the exception of Crochet (1988) and Crochet and Legat (1992), the limiting values of Ws numbers are below 0.6. Most of these limiting values and the type of the numerical schemes employed by different researchers are summarized by Zheng et al. (1990). In a recent study conducted by Crochet and Legat (1992) for a very dense grid (1009 elements) and using a consistent streamline–upwind/Petrov–Galerkin (SUPG) technique, a limiting value of Ws=1.5 was encountered with the differential counterpart of the integral Maxwell model used in this study. Thus, the low Ws limiting value encountered here is hardly surprising because the method used (*i.e.* Galerkin FEM and not SUPG) has the same difficulties as those used by other researchers (Sugeng and

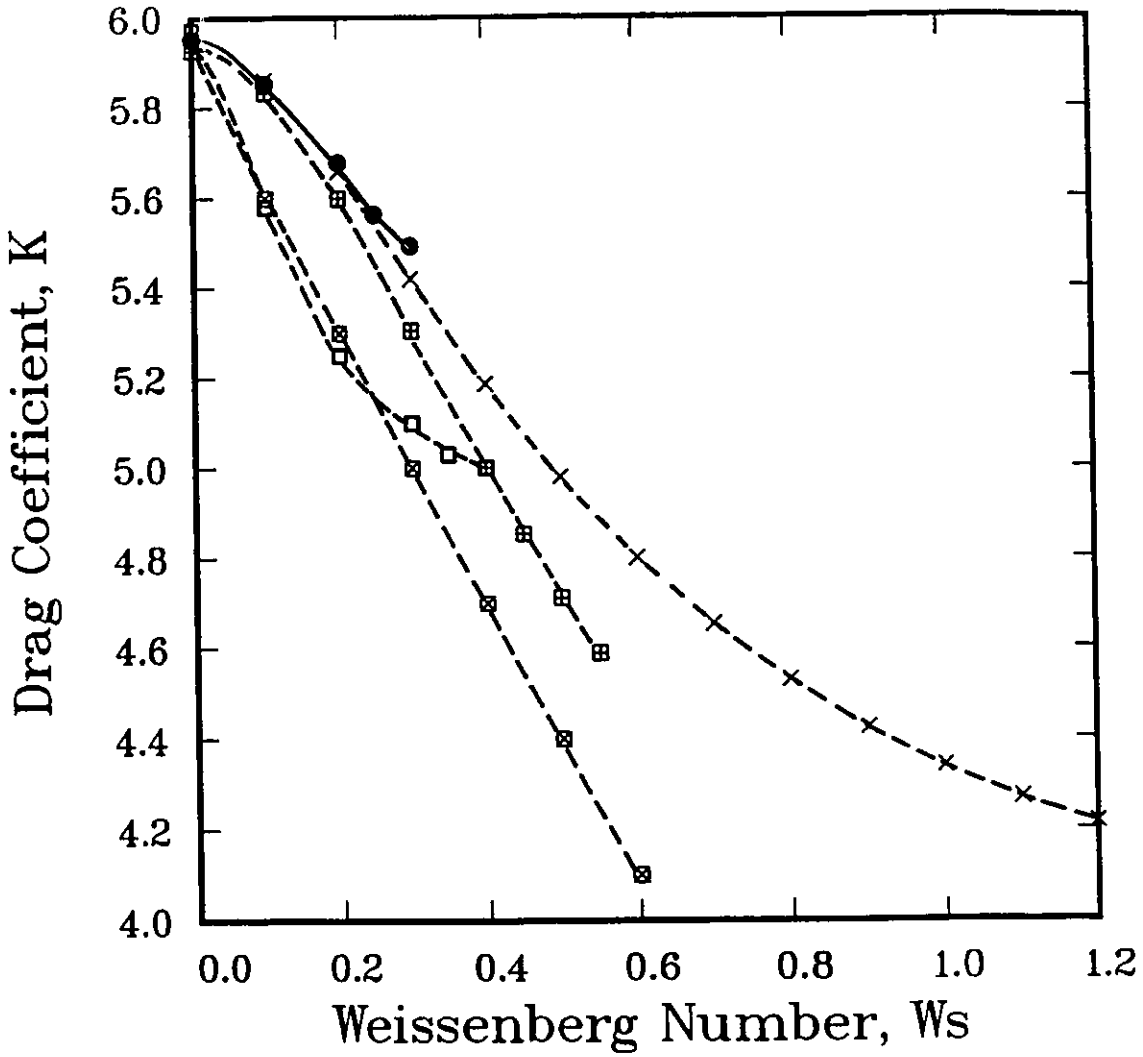

Figure 4.12: Drag coefficient as a function of Weissenberg number for the upper-convected Maxwell fluid; ● this work; + Crochet and Legat (1992); ◘ Luo and Tanner (1986); ⊞ Zheng et al. (1990); ◈ Sugeng and Tanner (1986).

Tanner, 1986; Luo and Tanner, 1986). The reasons for the numerical breakdown are not very clear, but the work of Phan-Thien (1983, 1984) gave an exact solution to a stagnation flow of the Maxwell and Oldroyd-B fluids and found that there is a limiting value of the Weissenberg number, beyond which no steady-state solution exists.

We have also used a value of $\theta = -0.25$ to examine the influence of a non-zero second normal stress difference ($N_2 \neq 0$) on the flow. The effect on the drag coefficient is to reduce it even further as shown in Figure 4.13. This novel result is equivalent to other viscoelastic phenomena such as the reduction in extrudate swell associated with a non-zero second normal stress difference N_2 (Luo and Tanner, 1988).

4.4 Concluding Remarks

In this chapter, results have been obtained from numerical simulations for a steady flow generated by a sphere falling along the centerline of a cylindrical tube (2:1 cylinder/sphere diameter ratio) containing Newtonian or viscoelastic liquids modelled by the upper-convected integral Maxwell constitutive equation. The numerical results, using the FEM are compared with results obtained by different numerical techniques by various researchers.

The present numerical results confirm the decrease in the drag coefficient with an increase in elasticity. Furthermore, the presence of second normal stress difference N_2 lowers the drag coefficient even further and this becomes significant as the elasticity increases. The present numerical simulations encountered a

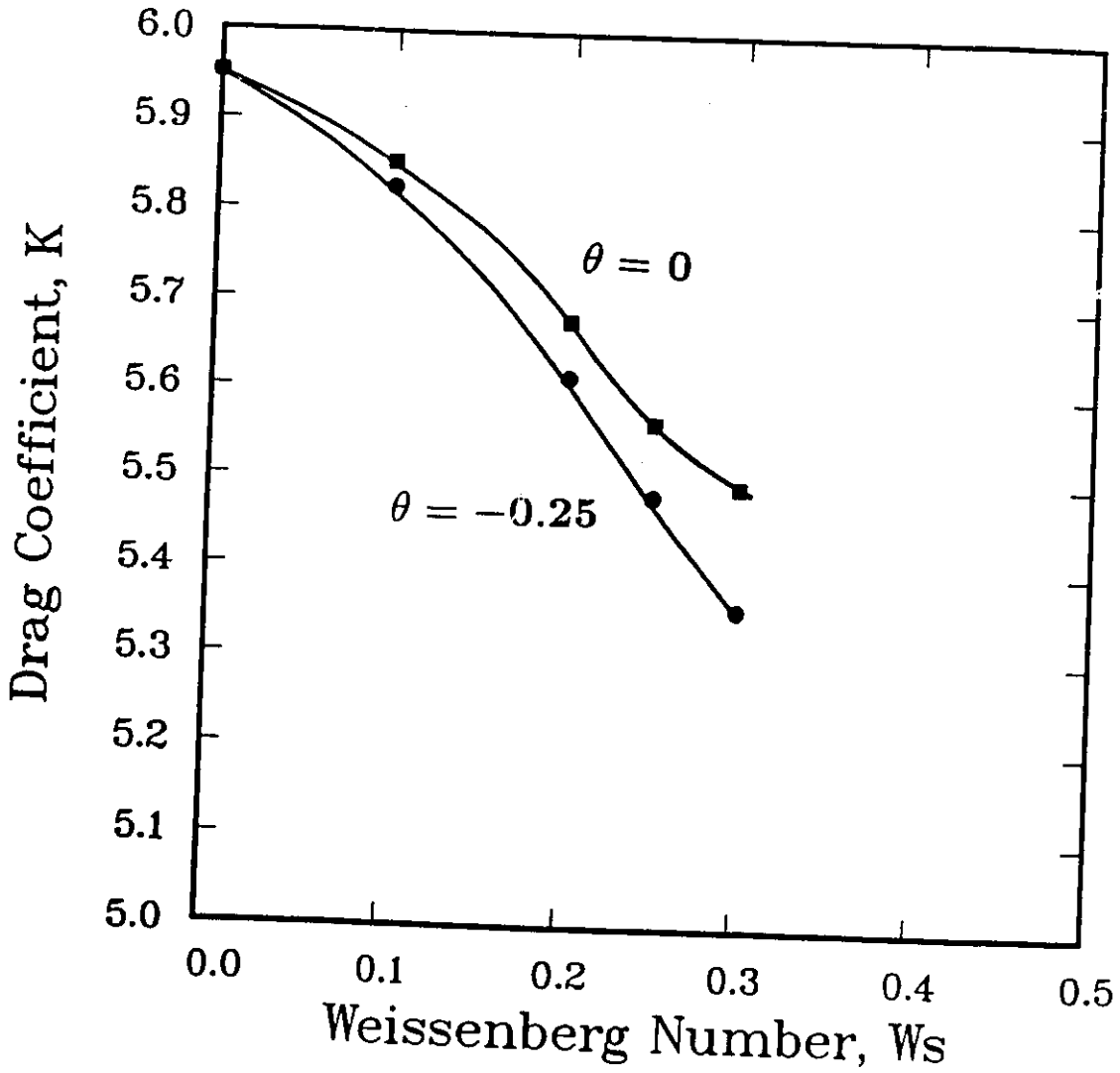

Figure 4.13: Drag coefficient as a function of Weissenberg number for the upper-convected Maxwell fluid. Effect of a non-zero second normal stress difference $N_2 = -0.2N_1$.

limiting Weissenberg number ($Ws = 0.3$), above which convergence could not be achieved because of the Galerkin formulation used. Although some researchers (Crochet and Legat, 1992), who used the SUPG formulation, claim to have encountered a higher value of a limiting Weissenberg number ($Ws = 1.5$), most other works have been limited to low values ($Ws < 0.6$).

In contrast to the results obtained by Luo (1987), our results do not show upstream shift in the streamlines from the Newtonian case for the range of Ws numbers used in this study.

In this chapter, we have tested and established the adequacy of our numerical scheme against published results by various researchers who used different numerical techniques to simulate the benchmark problem.

Chapter 5

Creeping Flow of Fluid M1 past a Sphere

In this Chapter we undertake the numerical simulation of the creeping motion past a sphere of a model fluid M1 contained in a very wide cylindrical tube having a 50:1 diameter ratio. The K-BKZ integral constitutive equation proposed by Papanastasiou et al. (1983) with the parameter constants determined by Chai and Yeow (1990) for fluid M1 is used as the working viscoelastic constitutive model.

Having established a proper finite element mesh, we will embark upon simulating the experiments by Tirtaatmaaja et al. (1990) for the M1 fluid, and the drag coefficient will be presented as a function of a surface-average shear rate or a dimensionless Weissenberg number.

5.1 Introduction

An improved understanding of non-viscometric flows such as flows around spheres can be achieved when a direct comparison between numerical and experimental works is possible. Unfortunately, relatively few examples of non-viscometric

flows exist with an adequate set of experimental results for materials which are well characterized rheologically to form a basis for further understanding of non-viscometric flow behaviour.

The early experimental works of flows around spheres have dealt with materials which are highly elastic and exhibit shear-thinning behaviour. This brings together two effects at the same time, namely the effect of the viscosity which is a function of the shear-rate, and the effect of elasticity through the characteristic relaxation time. These works have been criticized by Chhabra et al. (1980). For the systematic investigation of the deviation of the drag force from the Stokes' law, Chhabra et al. (1980) have investigated the influence of fluid elasticity using a constant viscosity fluid (Boger fluid) and found a reduction in the drag coefficient for $Ws > 0.1$ to some asymptotic value. Mena et al. (1987) have used different types of fluids for flows around spheres to investigate the influence of elasticity, shear-thinning, and wall effects upon the total drag force. These authors have concluded that both shear-thinning and elastic effects contribute to the drag reduction, which is in agreement with the works of Chhabra et al. (1980) for the latter case. However, in a more recent work by Tirtaatmadja et al. (1990) for an almost constant-viscosity Boger fluid, an initial decrease from the Newtonian case was observed followed by a rapid increase of the drag coefficient. Thus, different behaviours can be obtained even from fluids which do not show shear-thinning behaviour, depending on the polymeric constituents.

Despite the complexity of the problem, various numerical works have been

undertaken to investigate the flows of non-Newtonian fluids around spheres. For the flows of viscoelastic fluids around a sphere in an unbounded medium, Crochet (1982) used the upper-convected Maxwell model and observed a small decrease of around 3% from the Newtonian value. Another numerical solution obtained by Tiefenbruck and Leal (1982) for a four-constant Oldroyd-type model showed agreement with asymptotic predictions of both second and third-order fluid models, but no definite conclusions were made with respect to experimental results. Numerical solutions using the upper-convected Maxwell model by Hassager and Bisgaard (1983) showed that deviations from Stokes' law due to fluid elasticity are negligible up to a Deborah number of 3 for a sphere in an unbounded medium. In a more recent numerical work, Chilcott and Rallison (1988) have performed time-dependent numerical calculations for flows past a sphere at low Reynolds numbers using the FENE-dumbbell model with a set of simplified equations to represent a constant viscosity, elastic fluid. These investigators were able to obtain a qualitative fit for the drag reduction results of Chhabra et al. (1980) by choosing an appropriate set of parameters (see Figure 5.1).

Although wall effects can be neglected for spheres translating in large diameter tubes, viscoelastic effects can cause unpredictable phenomena in such non-viscometric flows. To model these flow phenomena, a more realistic constitutive equation has to be used along with an effective numerical scheme. It is, therefore, the purpose of this chapter to obtain a qualitative description between published experimental works and numerical solutions with an appropriate

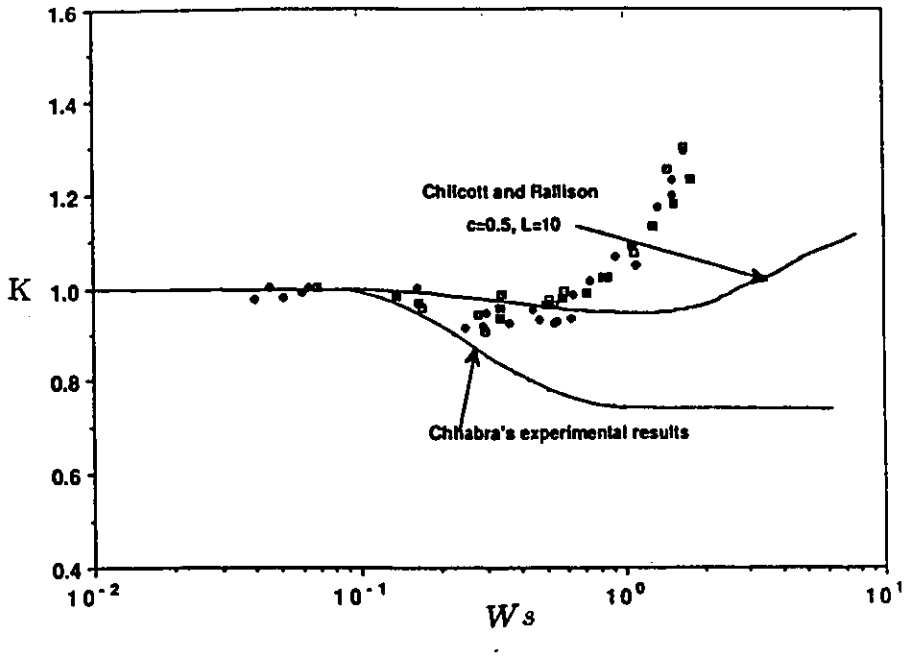

Figure 5.1: Drag correction factor as a function of Weissenberg number. Comparison between Chhabra's experimental results for a corn-syrup-based solution and Chilcott and Rallison's prediction using the FENE–dumbbell model. Symbols are experimental data of Tirtaatmadja et al. (1990) for fluid M1.

choice of a constitutive model, namely the K-BKZ model.

5.2 Test Fluids and Constitutive Models

In the mechanics of viscoelastic fluids, there has been a considerable gap between those who postulate constitutive equations and use them to obtain theoretical solutions for non-viscometric flow problems and those who collect experimental data in an attempt to verify or disprove available theoretical solutions. This gap has been bridged by choosing world-wide available fluid models, such as the Boger fluids, which have negligible shear-thinning effects and hence are good examples of elasticity-dominated media. This is a useful approach to avoid confusion and obtain a direct comparison between theoretical models and experimental data.

5.2.1 Test Fluids

Boger fluids have become increasingly important as test fluids for providing information on the behaviour of viscoelastic liquids in various flow fields. These fluids exhibit an approximately non-shear-thinning behaviour and have a region of quadratic normal stress behaviour in shear. As a result, these fluids are well suited for experimental work for the observation of elastic effects in flow fields without the complication of significant shear-thinning and inertial effects.

The fluid M1 belongs to this class of fluids. It consists of 0.244% polyisobutylene (PIB) in a mixed solvent consisting of 7% kerosene in polybutene (PB). The preparation of the test fluid and the manufacturer's specification on the constituents are detailed by Nguyen and Sridhar (1990). Other rheological

properties of the fluid M1 are also given by Binding et al. (1990), and Laun et al. (1990). For the purpose of the numerical work the appropriate choice of the constitutive equation is essential. The Oldroyd-B constitutive equation is one of the simplest models capable of providing a satisfactory description of the rheological properties of Boger fluids in shear flow. The model is known to exhibit unrealistic elongational characteristics in which the elongational viscosity grows without bound at a critical stretch rate, and it has failed to produce quantitative agreement on some key flow features observed experimentally (Debbaut et al., 1988). The limitations of this constitutive equation have continued to baffle many researchers.

5.2.2 The K-BKZ Representation of M1 Fluid

The search for more realistic models as a means of gaining further fundamental understanding on the flow properties of Boger fluids and other viscoelastic fluids in general is a major undertaking in the field. There have been numerous suggestions in the literature that constitutive models with a spectrum of relaxation times may be a good first step towards achieving the above goal. It has been argued that the flow behaviour of polymer solutions in different types of flow, such as shear flow and elongational flow, cannot be adequately described by models with one or two time constants. There are also sound theoretical reasons to associate a complete spectrum of relaxation times with a polymer solution (Denn and Marrucci, 1977). According to Denn (1977), different types of flow may "activate" different parts of the relaxation spectrum. It is therefore necessary to obtain the relaxation spectrum from the material functions and incorporate

Table 5.1: Material parameter values used in the K-BKZ model for fitting data of fluid M1 according to Chai and Yeow (1990) ($\alpha = 500,\ \beta = 0.001,\ \theta = -0.1,\ \rho = 0.9\ g\ cm^{-3}, k = 3$)

k	$\lambda_k(s)$	$a_k(Pa)$
1	$5.20\text{x}10^{-4}$	$3.06\text{x}10^{3}$
2	$8.90\text{x}10^{-2}$	$5.46\text{x}10^{0}$
3	$1.04\text{x}10^{0}$	$5.50\text{x}10^{-1}$

it into the constitutive equation. Such a constitutive equation is expected to perform better than constitutive equations with one or two time constants.

Recently a number of efforts have reported successes in using multiple relaxation time constitutive equations to model elongational behaviour of polymer melts. More specifically, the K-BKZ model described in Chapter 2 has shown a considerable success in modelling viscoelastic flows (Luo and Mitsoulis, 1990; Park and Mitsoulis, 1992).

To describe the rheological behaviour of a fluid such as M1, which has a relatively constant first normal stress coefficient, Chai and Yeow (1990) showed that no more than three relaxation times are required. This is in direct contrast to polymer melt systems, in which as many as eight relaxation times may be required (Luo and Mitsoulis, 1990). In this study, we adopt the material parameters established by Chai and Yeow (1990). The numerical values of the parameters associated with the K-BKZ model are presented in Table 5.1. Details of how to obtain the relaxation spectrum and the other constants appearing in the K-BKZ equation can be found in the works of Papanastasiou (1984) and Chai

(1990). The overall model predictions of shear and elongational viscosities and first normal stress difference along with some experimental data are presented in Figure 5.2. Note that a value of $\beta = 0.001$ is more appropriate for passing approximately through the envelope of the experimental elongational viscosity data. The fitting of N_1 is less satisfactory, giving rise to a dimensionless stress ratio (or recoverable shear) S_R defined by

$$S_R = \frac{N_1}{2\tau} = \frac{N_1}{2\eta_s\dot{\gamma}} \tag{5.1}$$

where τ is the shear stress. For the M1 data and according to the K-BKZ model, S_R increases monotonically with $\dot{\gamma}$ up to $\dot{\gamma} = 100\ s^{-1}$, where there is a maximum value of 1.67 (see Figure 5.3).

5.3 Newtonian Results for a 50:1 Diameter Ratio

Before proceeding to solve for viscoelastic flows, it is essential to establish a good solution for the Newtonian flow. This requires the choice of an appropriate finite element mesh. The results obtained must also conform to published results for comparison purposes.

The boundary conditions used for the flow around a sphere in a cylinder with a 50:1 diameter ratio are the same as those in the case of a 2:1 diameter ratio outlined in subsection 4.2.2.

5.3.1 Finite Element Meshes

For any numerical method it is necessary to try to establish some confidence in the results obtained. For the flow problem presented here we have studied

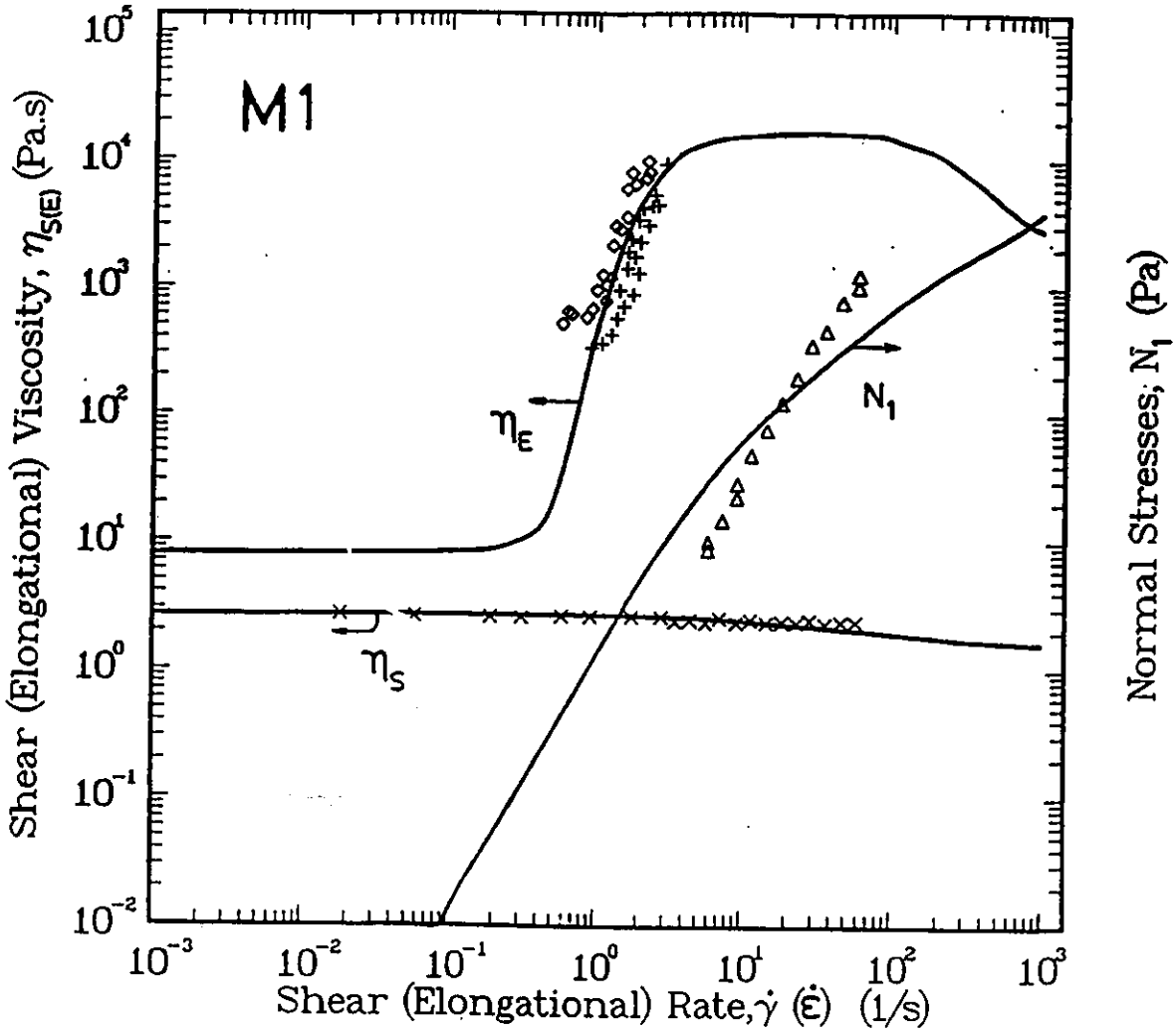

Figure 5.2: Model predictions of shear viscosity η_s, first normal stress difference N_1, and elongational viscosity η_E for fluid M1 using the K-BKZ model with data given in Table 5.1. Symbols are experimental data given by Chai and Yeow (1990).

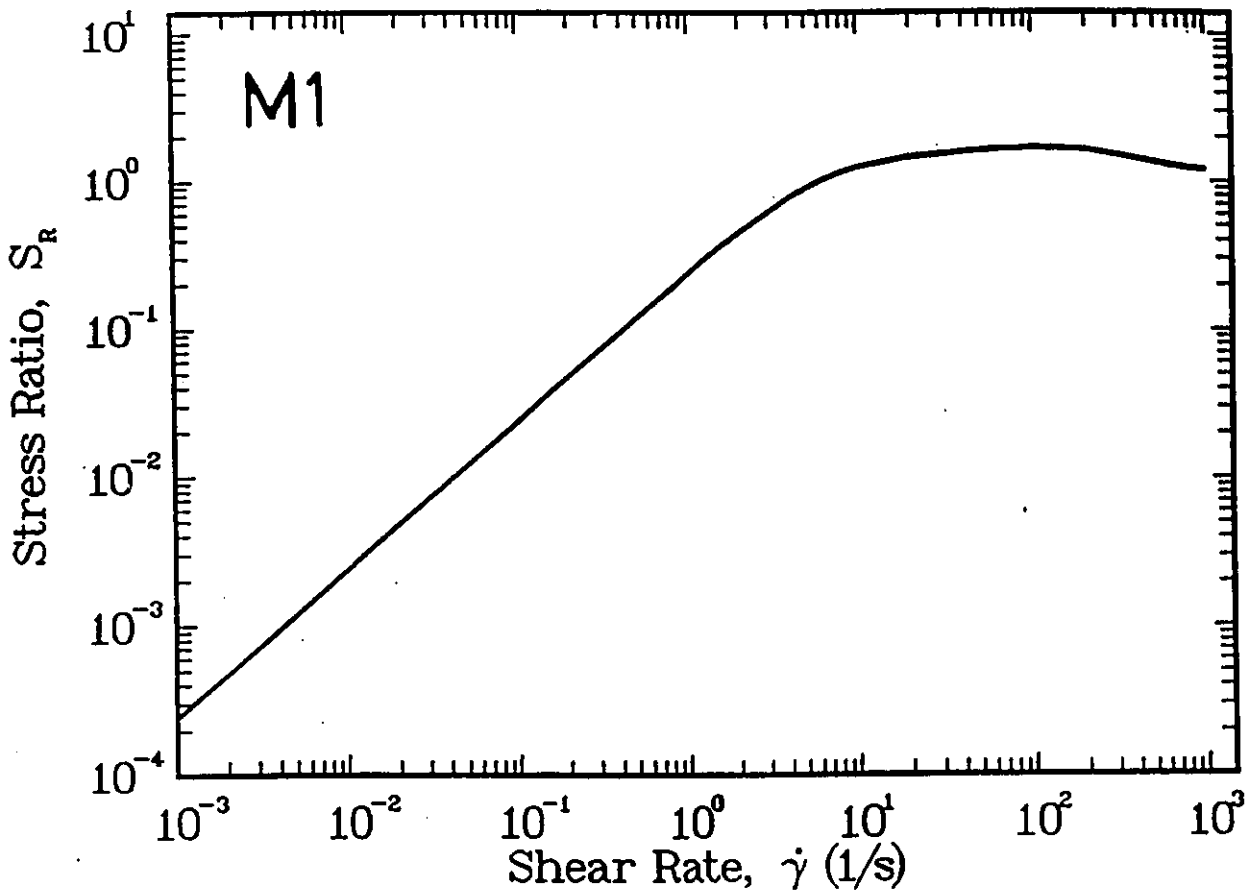

Figure 5.3: Model predictions of stress ratio S_R as a function of shear rate $\dot{\gamma}$ for fluid M1 using the K-BKZ model with data given in Table 5.1 (Park and Mitsoulis, 1992).

different finite element meshes with different densities and configurations. The design of finite element meshes for solving the present problem must take several factors into account. First, in view of the stress boundary layer which is likely to develop on the sphere surface, the finite element mesh near the sphere must be refined. Secondly, the mesh must be refined along the centerline downstream from the rear stagnation point. Thirdly, the velocity and stress fields do not require a high degree of mesh refinement as the distance from the sphere surface is increased.

Four finite element meshes were designed for obtaining the desired results. These meshes are presented in Figure 5.4, while their main parameters and results are shown in Table 5.2. MESH1 and MESH2 have the same number of elements. However, lengths of L_u and L_d of 25R were used in MESH1, while MESH2 has lengths of 50R. MESH3 contains 26 more elements than MESH1 and MESH2. These elements were added to the region within a radial distance of r=4R. This helps the analysis of mesh refinement especially in the vicinity of the sphere surface. It is important to notice that MESH1, MESH2 and MESH3 have the same number of elements from a radial distance of r=4R and further. In all the three meshes a perfectly circular grid was created up to a radial distance of r=4R in order to achieve mesh refinement having elements with very good aspect ratios. This is necessary in order to capture well the kinematics in the dynamically important region (not too far from the sphere surface). MESH4 was designed to have more elements inside an enlarged circular region (r=5R) and also outside. Special care has been taken to move the radial lines closer

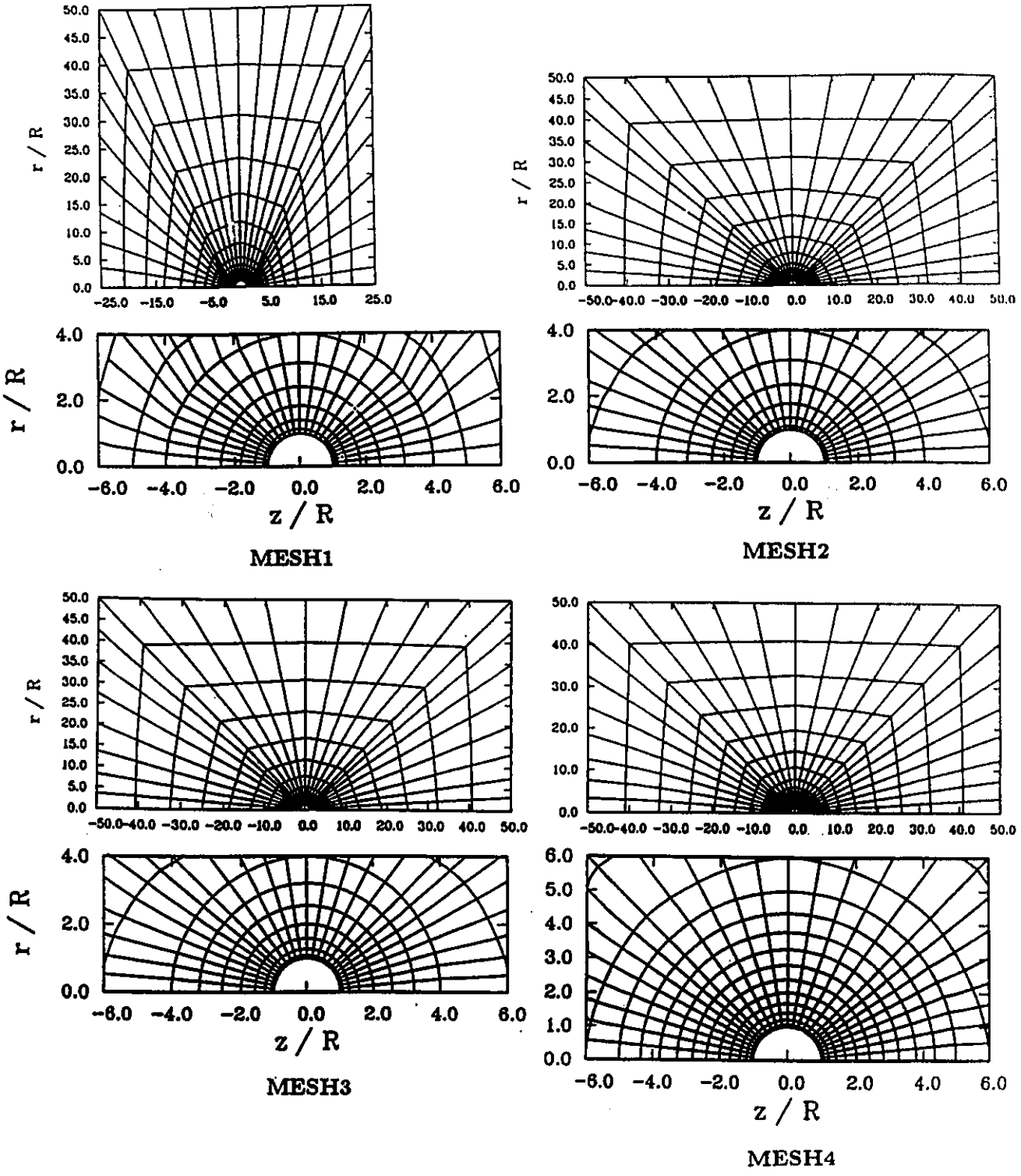

Figure 5.4: Finite element meshes and details (50:1 cylinder/sphere diameter ratio).

Table 5.2: Summary of characteristics for the finite element meshes used for the calculations and corresponding values of the drag coefficient K for Newtonian fluids flowing around a sphere in a tube ($R_c/R = 50:1$)

Name	Elements	Nodes	DOF	K
MESH1	364	1173	2751	1.0798
MESH2	364	1173	2751	1.0832
MESH3	390	1253	2938	1.0687
MESH4	520	1653	3873	1.0626

to the centerline. All four meshes contain 53 radial rows uniformly distributed around the sphere to ensure accurate drag calculations. All meshes used for this study are similar to the ones developed by Delvaux and Crochet (1990).

It is evident form Table 5.2 that as the mesh becomes more and more refined, the drag correction factor decreases to reach a value of 1.0626 for MESH4. The drag coefficient obtained using Equation 4.3 is 1.044. It should be noted, however, Equation 4.3 also gives an approximate value. MESH2 gives a slightly higher value of the drag coefficient from MESH1 due to the increased length in the axial direction.

The Newtonian results obtained using MESH4 are presented in Figure 5.5. These results are normalized using $\mu V/R$ as before. The pressure drops linearly from the front stagnation point where it reaches its dimensionless maximum value (1.592) to the rear stagnation point where it reaches the minimum value (-1.592). After the rear stagnation point the pressure shows a quadratic increase

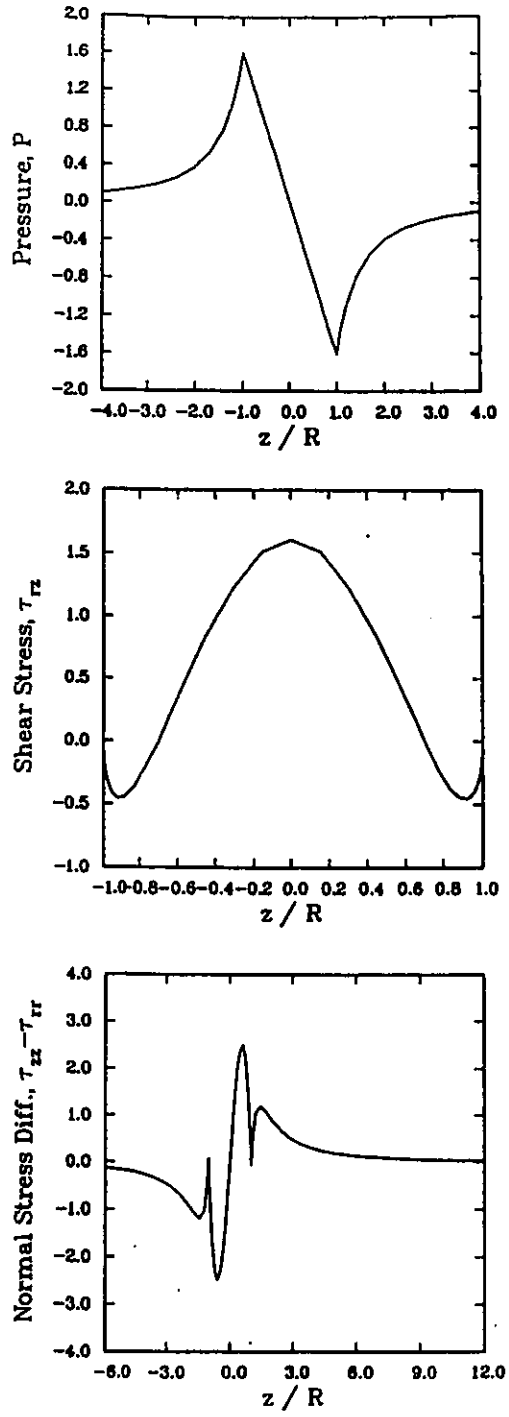

Figure 5.5: Newtonian results for pressure, shear stress and normal stress difference distributions along the axis of symmetry and on the sphere surface using MESH4 ($R_c/R = 50:1$).

to reach a value of zero. The shear stress shows a symmetric distribution with respect to z=0 line, and a maximum shear stress value (1.602) is achieved at r=R and z=0, as expected. The first normal stress difference N_1 shows an antisymmetric behaviour with respect to z=0 line. These results compare qualitatively with the results obtained for the 2:1 diameter ratio in Chapter 4.

5.4 Fluid M1 Flowing past a Sphere in a Tube (50:1 Diameter Ratio)

We now embark upon flow simulations of test fluid M1 flowing past spheres contained in a large cylinder (50R), as done experimentally by Tirtaatmadja et al. (1990). In the present study, the elasticity level will be characterized by a surface-average shear rate $\dot{\gamma}_a$ defined by

$$\dot{\gamma}_a = \frac{V}{R} \tag{5.2}$$

where V is the terminal velocity and R is the radius of the sphere. Note that $\dot{\gamma}_a$ is a convenient representation of flow rate in the absence of a single relaxation time.

The second normal stress difference N_2 was found experimentally to have a value between -10 to -20% of the first normal stress difference N_1 (Chirinos et al., 1990; Binding et al., 1990). For our numerical simulations we have chosen N_2/N_1=-1/9 or θ=-0.1.

MESH4 was selected for the purpose of the numerical simulations. This mesh has 520 elements, 1653 nodes and 3873 unknown DOF for the velocities and pressures. Lengths of 50R have been chosen as entry and exit of the domain

to guarantee the imposition of fully-developed velocity profiles away from the sphere and the total relaxation of stresses, especially for high $\dot{\gamma}_a$ values.

5.4.1 Results and Discussion

The simulations were initiated for the 50:1 diameter ratio as usual from the Newtonian creeping flow solution (S_R =Ws=0), and the terminal fluid velocity V was increased to reach higher flow rates and thus elasticity levels. Again, all lengths were scaled by R, all velocities by V and all pressures by μ_oV/R. The value of the constant viscosity μ_o as predicted by the K-BKZ model is 2.65 Pa.s, while the value of the corresponding Maxwellian relaxation time λ_0 is 0.142 s. The Weissenberg number is then calculated as $\lambda_0\dot{\gamma}_a$.

A comparative picture of the flow field between the Newtonian solution (Ws=0) and M1-fluid solution at Ws=0.3 ($\dot{\gamma}_a$=2.1 s^{-1}) is presented in Figure 5.6. The contour values have been normalized between the maximum value (denoted by a solid circle) and the minimum value (void circle) and drawn every 0.1 intervals, except for the streamlines where the dimensionless values are given on the graph. It is seen that the kinematics as represented by streamlines is hardly affected by viscoelasticity but the pressures and stresses show a different behaviour from the Newtonian solution. The symmetric Newtonian flow field becomes skewed behind the sphere. Most of these changes are prominent in the τ_{zz} component. Upstream of the front stagnation point the polymer is slightly stretched, whereas at the stagnation point itself the material is unstretched because all velocity components vanish owing to the no−slip boundary condition. Downstream of this stagnation region, the fluid begins to relax as it is convected

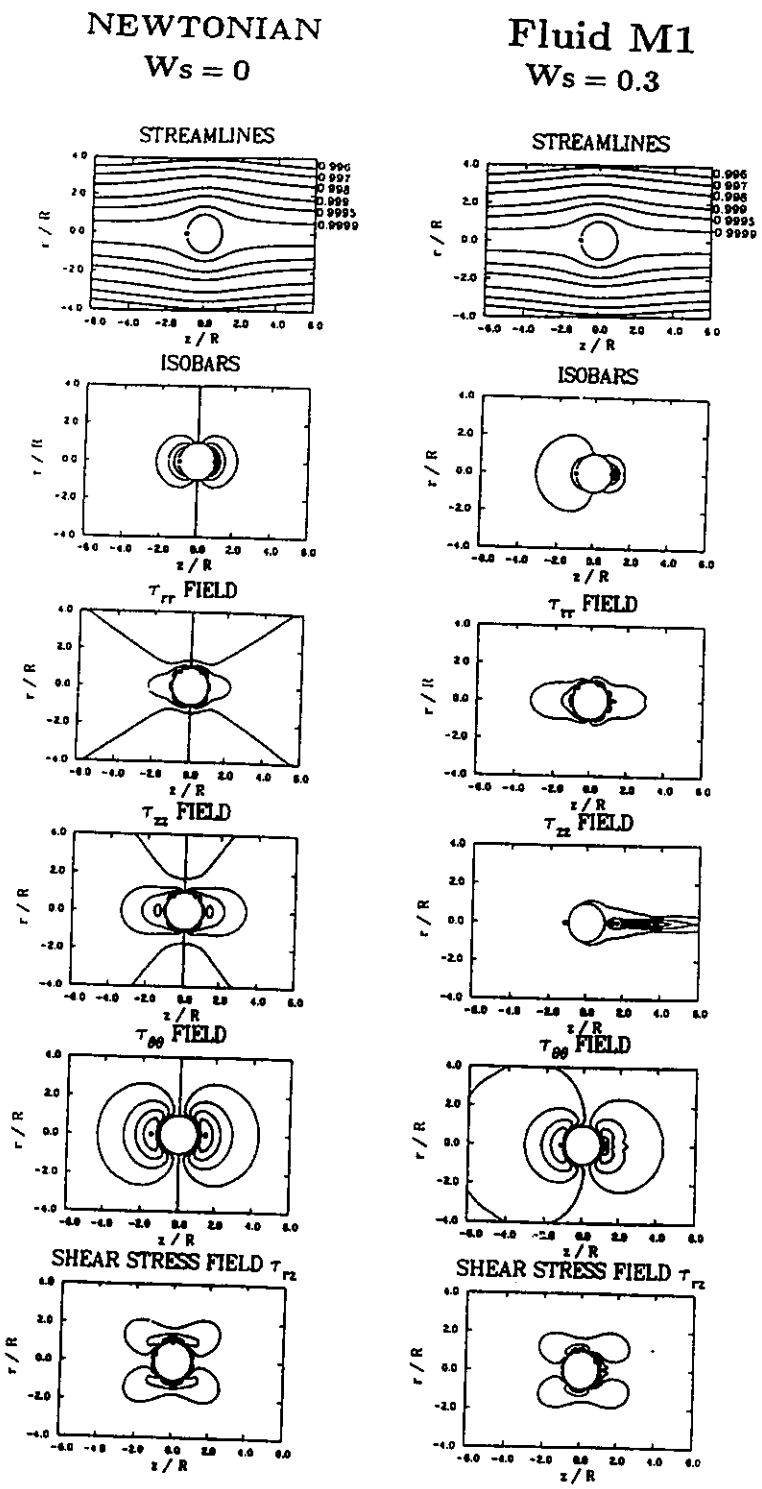

Figure 5.6: Comparative picture of flow fields for Newtonian and fluid M1 ($Ws = 0.3$, $\dot{\gamma}_a = 2.1\ s^{-1}$). ○ minimum value, ● maximum value.

around the sphere. Again at the rear stagnation point not much change occurs. However, a short distance from this region the fluid becomes highly deformed and extends far downstream before it becomes fully relaxed. These findings are also in qualitative agreement with those by Chilcott and Rallison (1988).

The maxima and minima are given numerically in Table 5.3. The pressures, shear stresses and first normal stress difference on the sphere surface and along the centerline behind the sphere are shown in Figure 5.7. As expected, the viscoelastic character of the fluid is aptly manifested in these graphs. The pressure distribution for the viscoelastic fluid becomes highly negative at the rear stagnation point to reach its minimum value given in Table 5.3. The shear stress (τ_{rz}) distribution indicates a shift towards the left to reach a maximum value faster than in the Newtonian case. At a short distance before the rear stagnation point, the shear stress (τ_{rz}) drops to a lower value than a short distance after the front stagnation point, thus changing the symmetric behaviour of the Newtonian case. The normal stress difference increases tremendously shortly after the rear stagnation point for the viscoelastic fluid and shows an exponential decay towards the exit after reaching a maximum point. This is the reason for the choice of a longer domain so that the normal stresses can be fully relaxed.

Convergence was good up to Ws=0.3 ($\dot{\gamma}_a$=2.1 s^{-1}), based on a constant relaxation time of λ_o=0.142 s as suggested by Tirtaatmadja et al. (1990). Convergence for values of $Ws > 0.3$ could not be achieved with our method. However, a detailed examination of the kinematics along the centerline behind the sphere, as done previously by Phan-Thien et al. (1991), revealed that the reason for

Table 5.3: Comparison between Newtonian maximum and minimum values for the pressures and stresses and corresponding values for fluid M1 at $Ws = 0.3$ (50:1 ratio).

Variable	Newtonian $Ws = 0$	Fluid M1 $Ws = 0.3$
P_{min}	-1.592	-5.574
P_{max}	1.592	1.575
$\tau_{rz,min}$	-0.445	-0.933
$\tau_{rz,max}$	1.602	1.883
$\tau_{rr,min}$	-1.245	-0.945
$\tau_{rr,max}$	1.245	1.741
$\tau_{zz,min}$	-1.238	-0.764
$\tau_{zz,max}$	1.238	14.095
$\tau_{\theta\theta,min}$	-0.397	-0.610
$\tau_{\theta\theta,max}$	0.397	0.463
$N_{1,min}$	-2.483	-2.413
$N_{1,max}$	2.483	14.386
Drag Coefficient, K	1.0626	1.0787

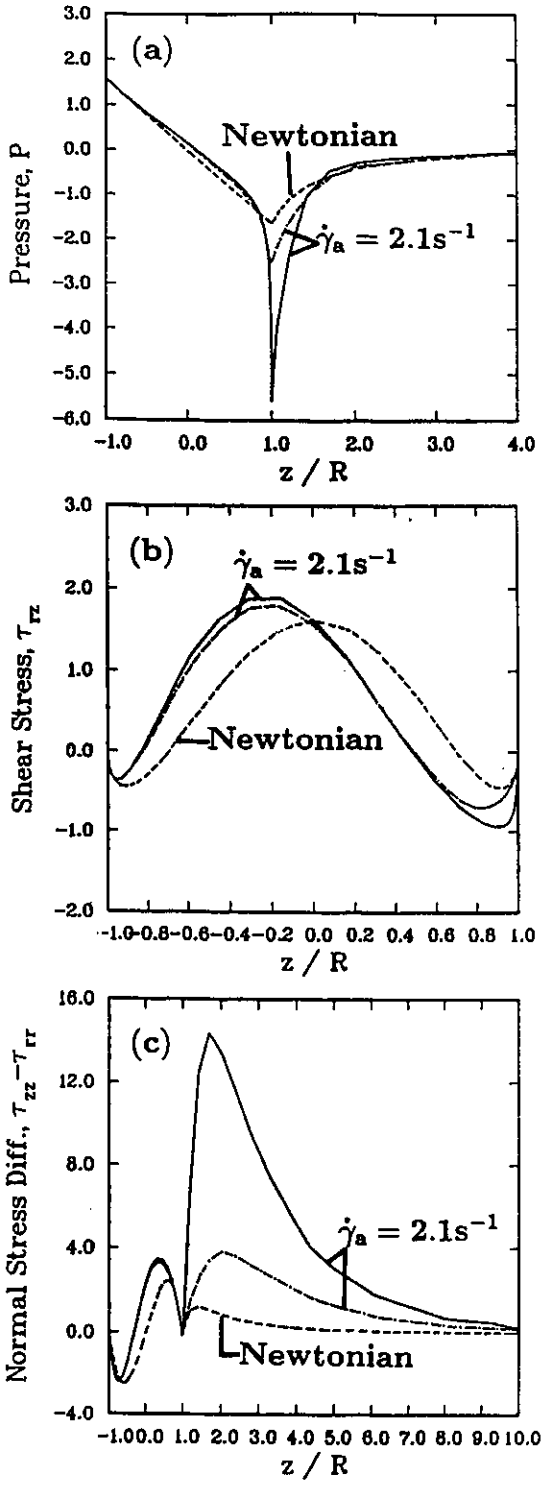

Figure 5.7: Comparison between a Newtonian fluid (dashed line) and fluid M1 flowing past a sphere in a cylinder (50:1 ratio) at $Ws = 0.3$ ($\dot{\gamma}_a = 2.1\ s^{-1}$). Distributions along the sphere surface and along the centerline behind the sphere for (a) pressure, (b) τ_{rz}, (c) $N_1 = \tau_{zz} - \tau_{rr}$. Solid lines correspond to converged solution at Ws=0.3, whereas broken lines are obtained by assuming Newtonian kinematics (no iterations performed).

divergence was due to a rapid increase of tensile stresses in the wake of the sphere. Assuming Newtonian behaviour at the immediate node after the rear stagnation point did not improve the convergence nor did it reduce the stress levels at the centerline. Clearly, the large values of the stresses yielded very large stress gradients which are impossible to resolve numerically by any reasonable numerical procedure.

At this point, it is worth noticing that the viscoelastic kinematics does not differ greatly from the Newtonian one for increasing flow rates. Therefore, it would be reasonable to assume a Newtonian velocity field and based on that calculate the viscoelastic stresses according to the K-BKZ model (Equation 2.12). Note that no iterations are performed, instead the stresses are directly calculated from the Newtonian velocities and velocity gradients. The results for the converged cases up to Ws=0.3 (see Figure 5.7) showed that this is a reasonable assumption, especially since the values of the stresses and pressure (hence the drag) on the sphere were not altered appreciably.

The results for the pressures are shown in Figure 5.8a. Note that most of the change in the pressure occurs at the stagnation point and shows a very steep slope in front and behind this point. At high $\dot{\gamma}_a$ values ($\dot{\gamma}_a = 9\ s^{-1}$ and $10\ s^{-1}$) the pressure shows an overshoot above zero, unlike the Newtonian case. The shear stresses around the sphere surface (Figure 5.8b) for different $\dot{\gamma}_a$ values by assuming Newtonian kinematics do not show a marked difference at high $\dot{\gamma}_a$ values ($\dot{\gamma}_a = 9\ s^{-1}$ and $10\ s^{-1}$). On the other hand the normal stress difference plotted along the centerline behind the sphere (Figure 5.8c) by assuming New-

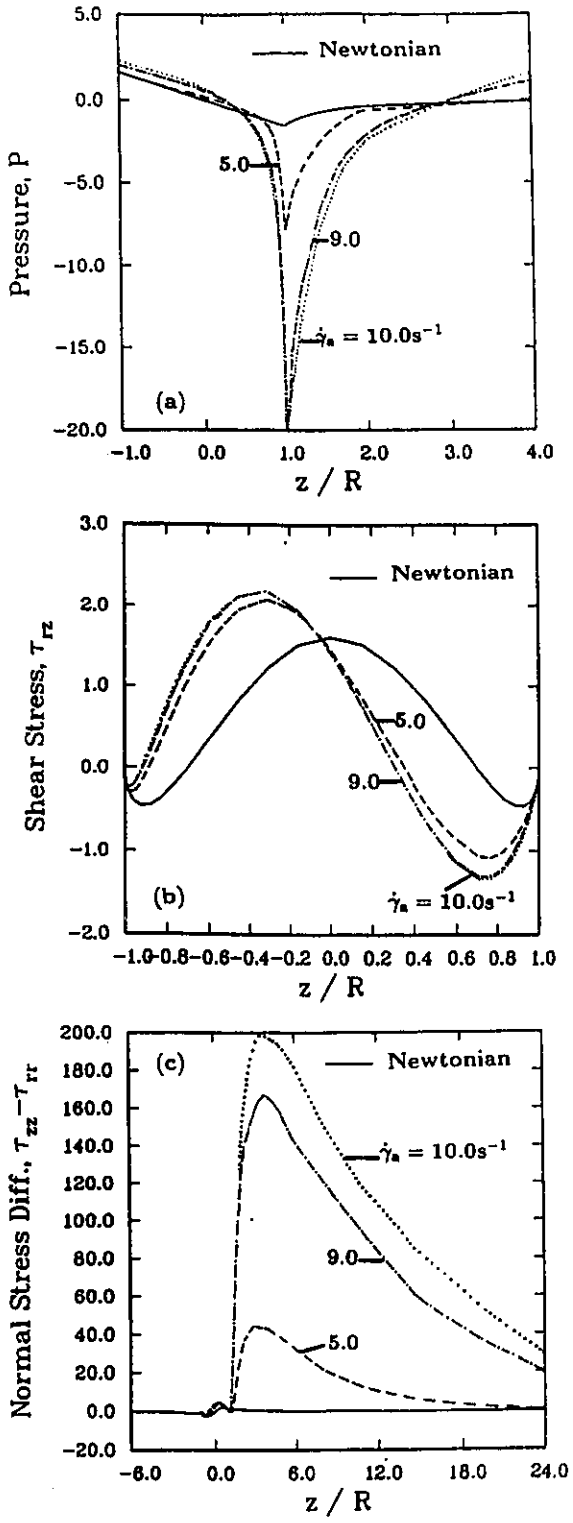

Figure 5.8: (a) Pressure (b) shear stress (c) normal stress distributions at the sphere surface and along the centerline at different surface-average shear rates assuming Newtonian kinematics.

tonian kinematics shows very high stress levels, and their relaxation takes quite some distance to achieve. These results are also in qualitative agreement with Figure 2 of Phan-Thien et al. (1991).

5.4.2 Drag Coefficient for M1 Fluid

Drag coefficient calculations were carried out for both the converged solutions (up to Ws=0.3 or $\dot{\gamma}_a = 2.1\ s^{-1}$) and the ones using the Newtonian kinematics. These results are presented in Table 5.4 and cover the whole range of experimental data collected by Tirtaatmadja et al. (1990).

The results obtained using the assumption of Newtonian kinematics are slightly lower than their converged counterparts (Figure 5.9) (maximum difference 3.04%) but the gap becomes narrower with decreasing $\dot{\gamma}_a$ values (difference of 0.89% at $\dot{\gamma}_a = 0.01\ s^{-1}$). The graph indicates a very slow decrease in drag coefficient for up to Ws=0.142 ($\dot{\gamma}_a = 1.0\ s^{-1}$) and then a rapid decrease for up to Ws=0.3 ($\dot{\gamma}_a = 2.1\ s^{-1}$) where it reaches a minimum value of 1.0456 which is 1.6% less than the Newtonian drag coefficient. This value is much higher than the 5% reduction from the Newtonian result reported by Tirtaatmadja et al. (1990). Past Ws=0.3 ($\dot{\gamma}_a = 2.1\ s^{-1}$) a rapid increase in the drag coefficient is obtained which is consistent with the experimental results of Tirtaatmadja et al. (1990). At Ws=1.42 ($\dot{\gamma}_a = 10\ s^{-1}$) as much as 50% increase from the Newtonian drag coefficient and 18% increase from the experimental result was observed at the same Ws number. Although the present results show a similar trend with the experimental results, the reason for the discrepancy in the magnitude is puzzling. As a conjecture, it is offered here that the occurrence

Table 5.4: Summary of drag coefficient results for different values of $\dot{\gamma}_a$. The results obtained by assuming Newtonian kinematics and their converged counterparts are denoted by K_N and K_{conv}, respectively.

$\dot{\gamma}_a$	Ws	K_N	K_{conv}
0.01	$1.42\text{x}10^{-3}$	1.0580	1.0675
0.05	$7.10\text{x}10^{-3}$	1.0579	1.0674
0.1	$1.42\text{x}10^{-2}$	1.0577	1.0673
0.2	$2.84\text{x}10^{-3}$	1.0573	1.0674
0.5	$7.10\text{x}10^{-2}$	1.0553	1.0678
1.0	$1.42\text{x}10^{-1}$	1.0508	1.0699
1.2	$1.70\text{x}10^{-1}$	1.0491	1.0711
1.4	$1.99\text{x}10^{-1}$	1.0477	1.0723
1.6	$2.27\text{x}10^{-1}$	1.0466	1.0733
1.8	$2.56\text{x}10^{-1}$	1.0459	1.0739
2.0	$2.84\text{x}10^{-1}$	1.0456	1.0723
2.1	$2.98\text{x}10^{-1}$	1.0456	1.0731
2.2	$3.12\text{x}10^{-1}$	1.0458	1.0786
2.5	$3.55\text{x}10^{-1}$	1.0479	
3.0	$4.26\text{x}10^{-1}$	1.0524	
4.0	$5.68\text{x}10^{-1}$	1.0759	
3.0	$4.26\text{x}10^{-1}$	1.0524	
4.0	$5.68\text{x}10^{-1}$	1.0759	
5.0	$7.10\text{x}10^{-1}$	1.1201	
6.0	$8.52\text{x}10^{-1}$	1.1855	
7.0	$9.94\text{x}10^{-1}$	1.2629	
9.0	$1.28\text{x}10^{0}$	1.4724	
10.0	$1.42\text{x}10^{0}$	1.5994	

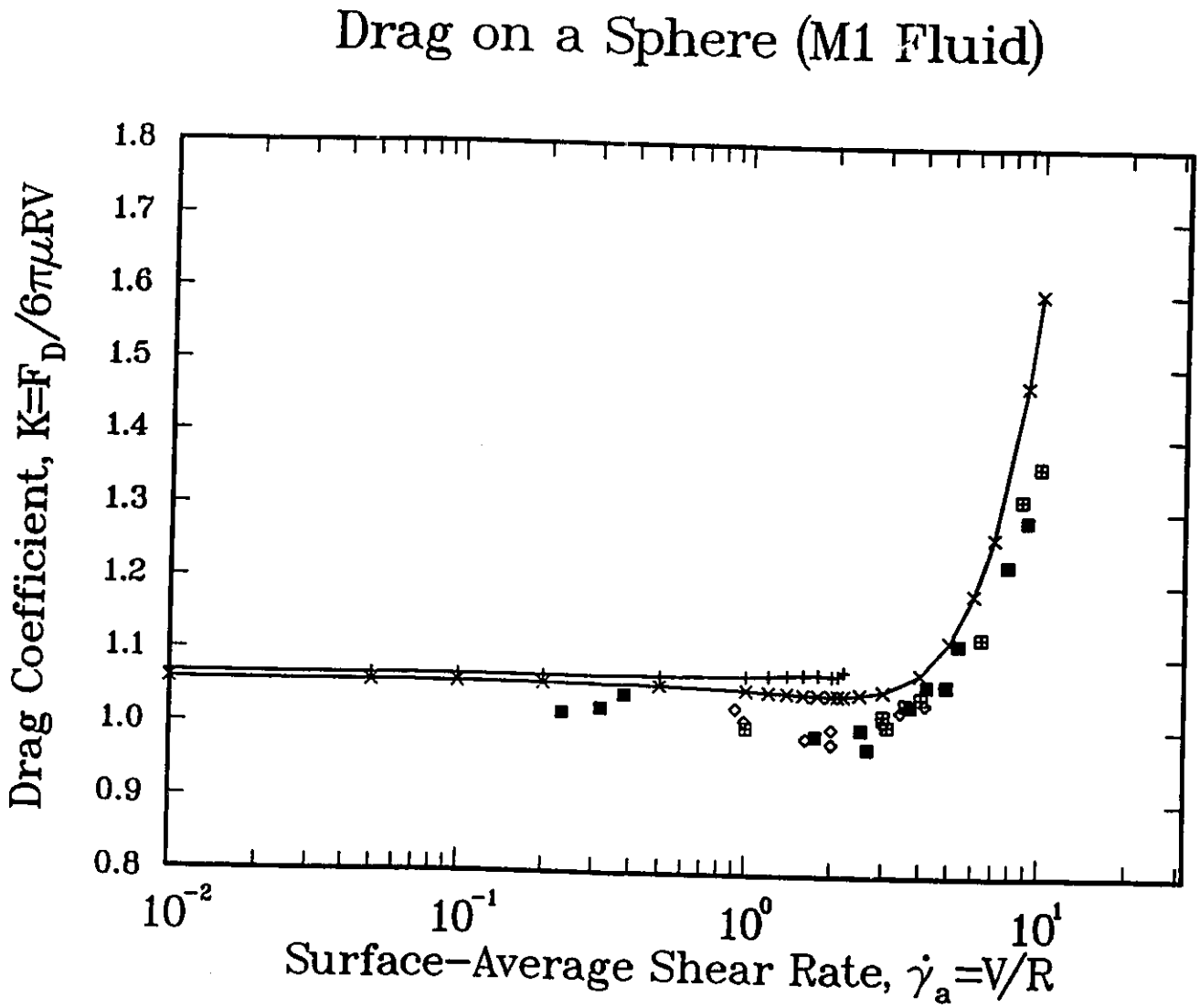

Figure 5.9: Drag coefficient results as a function of surface-average shear-rate for spheres translating in fluid M1: present results denoted by + (iterated) and × (assuming Newtonian kinematics); other symbols are experimental data by Tirtaatmadja et al. (1990).

of slip at the sphere surface may be responsible for that decrease. It has been observed both experimentally (Hatzikiriakos and Dealy, 1992) and numerically (Silliman and Scriven, 1980) that slip occurs at high flow rates and its effect is to reduce a drastic viscoelastic behaviour otherwise exhibited by assuming the stick-condition at solid walls. However, lack of any information of slip law for the M1 fluid, renders such investigation beyond the scope of this thesis.

The results obtained in this study show a different behaviour (see Figure 5.1) from the experimental results obtained by Chhabra et al. (1980) for a corn-syrup-based polyacrylamide solution which also has a constant viscosity (Boger fluid). This difference can be attributed to the variation in polymer constituents between the different solutions used. The increase in drag after Ws=0.3 ($\dot{\gamma}_a = 2.1\ s^{-1}$) for the present results indicates that the M1 fluid can be used as a friction enhancing substance beyond this value of Ws number.

5.5 Concluding Remarks

In this Chapter numerical simulations have been undertaken for flow around a sphere in an unbounded medium, which was approximated by a system of a containing cylinder with a 50:1 cylinder/sphere diameter ratio. Different finite element meshes were used to establish an accurate value for the drag coefficient of Newtonian fluids, which was found to be 1.0626. Using the densest mesh, simulations were undertaken for an experimental viscoelastic model fluid (M1), for which experimental drag results have appeared in the literature. The numerical simulations converged for a value of the surface-average shear rate $\dot{\gamma}_a < 2.1\ s^{-1}$,

corresponding to a dimensionless Weissenberg number of 0.3, while the drag remained virtually constant around the Newtonian value. The reason for the divergence was apparently due to the extremely high tensile stresses in the wake of the sphere. However, it was observed that the kinematics did not differ much from the Newtonian ones for all converged cases. As an approximation, the assumption of Newtonian kinematics was made, and the drag coefficient was thus calculated for the experimental range of $\dot{\gamma}_a$ values ($\dot{\gamma}_a \leq 10\ s^{-1}$). The drag coefficient was found to increase, in qualitative agreement with the experiments. However, the numerical values so obtained gave overestimates reaching 18% for $\dot{\gamma}_a = 10\ s^{-1}$ (Ws=1.42). It is conjectured that slip at the sphere wall may be responsible for the lower values found experimentally.

Chapter 6

Conclusions and Recommendations

The present work has dealt with the numerical simulation of viscoelastic materials exhibiting relaxation phenomena. A series of flows have been analyzed with the Finite Element Method (FEM). The models used are the Newtonian fluid, the Maxwell and Oldroyd-B integral models of linear viscoelasticity, and a special type of a K-BKZ type integral model of non-linear viscoelasticity, which is able to fit shear and elongational viscosity data and normal stress data as measured in shear flows.

Problems that have been solved are:

(1) Fully-developed, pressure-driven (Poiseuille) flow between parallel plates and in tubes.

(2) Flow around a sphere contained in a tube with a 2:1 diameter ratio (a benchmark problem).

(3) Unbounded flow around a sphere approximated by a 50:1 cylinder/sphere diameter ratio in a bid to simulate experimental results for the drag coef-

ficient obtained from a model viscoelastic polymeric liquid (fluid M1).

The major contributions of the present work are:

- A thorough and accurate determination of the drag coefficient and flow and stress fields in flows of Maxwell fluids around a sphere contained in a cylinder with a 2:1 diameter ratio. The results have been obtained for the range of a dimensionless Weissenberg number ($0<Ws<0.3$), for which convergence could be achieved. They showed a monotonic decrease of the drag coefficient with increasing Ws number, starting from the Newtonian value of 5.9522 and reaching 5.4935 for $Ws=0.3$. Verification with other results in the literature gave good agreement.

- The inclusion of a non-zero second normal stress difference in the calculations for the 2:1 ratio produced novel predictions and showed that the drag coefficient is further reduced as the Ws number increases.

- A thorough and accurate determination of the drag coefficient and flow and stress fields in flows of the model M1 fluid around a sphere contained in a cylinder with a 50:1 diameter ratio. The fluid has been modelled with the K-BKZ integral constitutive equation, which fits well experimental shear and elongational data. Converged results have been obtained up to $Ws=0.3$. They show a constant drag coefficient close to the Newtonian value of 1.0626, which is in agreement with the experimental findings for low Ws numbers. For values of $Ws>0.3$, simulations have been undertaken based on Newtonian kinematics. They show a rapid increase of the drag with Ws number, but overestimate the experimental data by as much as 18% for the highest Ws value of 1.42. However, the drag results

pass through a minimum around Ws=0.3, as also evidenced experimentally. The above findings suggest that slip may be occurring at moderate to high elasticity levels (or equivalently, Ws numbers), which has as a result the reduction of the drag coefficient calculated on the sphere surface.

The main recommendations for future work are:

- Inclusion of slip to account for the failure of polymeric liquids to stick to solid walls at high flow rates (or equivalently, high Ws numbers).
- Numerical simulations for other polymeric liquids, which show either an increase or a decrease in drag with Ws, so that a definitive picture can emerge regarding these phenomena.

From the numerical point of view, it would be important to carry out the following developments:

- Include a Streamline-Upwind/Petrov-Galerkin (SU/PG) scheme for the integration of the viscoelastic stresses to overcome problems of convergence beyond Ws=0.3. This development can follow the basic steps implemented by Heng (1987) in his inclusion of SU/PG schemes for the energy equation.
- Include some acceleration scheme to improve convergence of the iterative process.
- Develop an automated grid generation scheme to avoid tedious grid data preparation.
- Extend the program's ability to handle three-dimensional flows.

Bibliography

[1] Abdali,S., *"Numerical Simulation of Viscoplastic Material Flow through Extrusion Dies"*, M.A.Sc. Thesis, Dept. Chem. Eng., Univ. of Ottawa, Ottawa, ON (1992).

[2] Acharya, A., R.A. Mashelkar and J. Ulbrecht, *"Flow of Inelastic and Viscoelastic Fluids past a Sphere I. Drag Coefficient in Creeping and Boundary Layer Flows"*, Rheol. Acta, **15**, 454-470 (1976).

[3] Adachi, K., N. Yoshioka and K. Sakai, *"An Investigation of Non-Newtonian Flow past a Sphere"*, J. Non-Newt. Fluid Mech., **3**, 107-125 (1978).

[4] Astarita, G., *"Variational Principles and Entropy Production in Creeping Flow of Non-Newtonian Fluids"*, J. Non-Newt. Fluid Mech., **2**, 343-351 (1977).

[5] Ballenger, T.F., I.J. Chen, J.W. Crowder, G.E. Hagler, D.C. Bogue and J.L. White, *"Polymer Melt Flow Instabilities in Extrusion: Investigation of the Mechanism and Material and Geometric Variables"*, Trans. Soc. Rheol., **15**, 195-215 (1971).

[6] Ben-Sabar, E. and B. Caswell, *"A Stable Finite Element Simmulation of Convective Transport"*, Int. J. Num. Meth. Eng., **14**, 545-565 (1979).

[7] Bernstein B., E.A. Kearsley and L.J. Zapas, *"A Study of Stress Relaxation with Finite Strain"*, Trans. Soc. Rheol., **7**, 391-410 (1963).

[8] Binding, D.M., D.M. Jones and K. Walters, *"The Shear and Extensional Flow Properties of M1"*, J. Non-Newt. Fluid Mech., **35**, 121-135 (1990).

[9] Bird, R., W.E. Stewart and E.N. Lightfoot, *"Transport Phenomena"*, John Wiley & Sons, New York (1960).

[10] Bisgaard, C., *"Velocity Fields around Spheres and Bubbles Investigated by Laser-Doppler Anemometer"*, J. Non-Newt. Fluid Mech., **12**, 283-302 (1983).

[11] Broadbent, B. and B. Mena, *"Slow Flow for an Elastico-Viscous Fluid past Cylinders and Spheres"*, Chem. Eng. J., **8**, 11-19 (1974).

[12] Bush, M.B., *"The Application of Boundary Value Methods to Some Fluid Mechanics Problems"*, Ph.D. Thesis, University of Sydney, Sydney, Australia (1983).

[13] Bush, M.B., R.I. Tanner and N. Phan-Thien, *"A Boundary Element Investigation of Extrudate Swell"*, J. Non-Newt. Fluid Mech., **18**, 143-162 (1985).

[14] Carew, E.O. and P. Townsend, *"Non-Newtonian Flow past a Sphere in a Long Cylindrical Tube"*, Rheol. Acta, **27**, 125-129 (1988).

[15] Caswell, B. and W.H. Schwarz, *"The Creeping Motion of a Non-Newtonian Fluid past a Sphere"*, J. Fluid Mech., **13**, 417-426 (1962).

[16] Caswell, B., 4th Inter. Workshop on Non-Newt. Flows, Lake Morey, VM, USA (1983).

[17] Chhabra, R.P., P.H.T. Uhlherr and D.V. Boger, *"The Influence of Fluid Elasticity on the Drag Coefficient for Creeping Flow around a Sphere"*, J. Non-Newt. Fluid Mech., **6**, 187-199 (1980).

[18] Chirinos, M.L., P. Crain, A.S. Lodge, J.L. Schrag and J. Yaritz, *"Measurements of $N_1 - N_2$ and η in Steady Shear Flow and η', η'', and Birefringence in Small-Strain Oscillatory Shear for the Polyisobutylene Solution M1"*, J. Non-Newt. Fluid Mech., **35**, 105-119 (1990).

[19] Cho, Y.I. and J.P. Hartnett, *"Drag Coefficients of a Slowly Moving Sphere in Non-Newtonian Fluids"*, J. Non-Newt. Fluid Mech., **12**, 243-247 (1983).

[20] Chai, M.S. and L.Y. Yeow, *"Modelling of Fluid M1 Using Multiple - Relaxation - Time Constitutive Equations"*, J. Non-Newt. Fluid Mech., **35**, 459-470 (1990).

[21] Chilcott, M.D. and J.M. Rallison, *" Creeping Flow of Dilute Polymer Solutions past Cylinders and Spheres"*, J. Non-Newt. Fluid Mech., **29**, 381-432 (1988).

[22] Clift, R., J.R. Grace and M.E. Weber, *"Bubbles, Drops and Particles"*, Academic Press, New York (1978).

[23] Crochet, M.J., *"The Flow of Maxwell Fluid around a Sphere"*, Finite Elements in Fluids, Vol. 4 (Eds. R.H. Gallagher, D.H. Norrie, J.T. Oden and O.C. Zienkiewicz), Wiley, New York, 573-597 (1982).

[24] Crochet, M.J., A.R. Davies and K. Walters, *"Numerical Simulation of Non-Newtonian Flow"*, Elsevier, Amsterdam (1984).

[25] Crochet, M.J., *"Forward to the Proceedings of the Fourth Workshop on Numerical Methods in Viscoelastic Flow"*, J. Non-Newt. Fluid Mech., **20**, 1-9 (1986a).

[26] Crochet, M.J., *"Numerical Simulation of Highly Viscoelastic Flows"*, Proc. 10th Int. Cong. on Rheology, Sydney, Australia 1.19 (1988).

[27] Crochet, M.J., *"Numerical Simulation of Viscoelastic Flow: A Review"*, Rubber Chemistry and Technology, **62**, 426-455 (1989).

[28] Crochet, M.J. and V. Legat, *"The Consistent Streamline - Upwind / Petrov - Galerkin Method for Viscoelastic Flow Revisited"*, J. Non-Newt. Fluid Mech., **42**, 283-299 (1992).

[29] Curle, N. and H.J. Davies, *"Modern Fluid Mechanics, Vol. 1: Incompressible Flow"*, D. Van Nostrand Company Ltd., London (1968).

[30] Dairenieh, I.S. and A.J. McHugh, *"Viscoelastic Fluid Flow past a Submerged Spheroidal Body"*, J. Non-Newt. Fluid Mech., **19**, 85-111 (1985).

[31] Debbaut, B., J.M. Marchall and M.J. Crochet, *"Numerical Simulation of Highly Viscoelastic Flows through an Abrupt Contraction"*, J. Non-Newt. Fluid Mech., **29**, 119-146 (1988).

[32] Delvaux, V. and M.J. Crochet, *"Numerical Prediction of Anomalous Transport Properties in Viscoelastic Flow"*, J. Non-Newt. Fluid Mech., **37**, 297-315 (1990).

[33] Denn, M.M. and G. Marrucci, *"Effect of a Relaxation Time Spectrum on Mechanics"*, J. Non-Newt. Fluid Mech., **2**, 159-167 (1977).

[34] Denn, M.M., *"Extensional Flows: Experimental and Theory"*, in The Mechanics of Viscoelastic Fluids, AMD Vol. 22 (Ed. R.S. Rivlin), ASME, New York, NY, 101-125 (1977).

[35] Finlayson, B.A., *"The Method of Weighted Residuals and Variational Principles"*, Academic Press, New York (1972).

[36] Gallagher, R.H. *"Finite Element Analysis: Fundamentals"*, Prentice Hall, New Jersey (1975).

[37] Gartling, D.K., *"Report from Sandia Laboratories"*, Alberquerque, New Mexico, Sand. 77-1333 (1978).

[38] Giesekus, M., *"The Simultaneous Translation and Rotation of a Sphere in a Viscoelastic Fluid"*, Rheol. Acta, **3**, 59-71 (1963).

[39] Happel, J. and H. Brenner, *"Low Reynolds Number Hydrodynamics"*, Prentice-Hall, Engelwood, NJ (1965).

[40] Happel J. and H. Brenner, *"Low Reynolds Number Hydrodynamics"*, Noordhoff, Leiden (1973).

[41] Hassager, O. and C. Bisgaard, *"A Lagrangian Finite Element Method for the Simulation of Flow of Non-Newtonian Liquids"*, J. Non-Newt. Fluid Mech., **12**, 153-164 (1983).

[42] Harlen, O.G., *"High-Deborah Number Flow of a Dilute Polymer Solution past a Sphere Falling along the Axis of a Cylindrical Tube"*, J. Non-Newt. Fluid Mech., **37**, 157-173 (1990).

[43] Hatzikiriakos S.V. and J.M. Dealy, *"Role of Slip and Fracture in the Oscillating Flow of HDPE in a Capillary"*, J. Rheol., **36**, 845-884 (1992).

[44] Hill, R. and G. Power, *"Extremum Principles for Slow Viscous Flow and the Approximate Calculation of Drag"*, Quart. J. Mech. Appl. Math., **9**, 313-319 (1956).

[45] Huebner, K.M. and E.A. Thornton, *"The Finite Element Method for Engineers"*, Wiley, New York (1982).

[46] Kaye, A., College of Aeronautics, Cranfield, Note No. 134 (1962).

[47] Lamb, H., *"Hydrodynamics"*, Dover, New York (1945).

[48] Laun H.M., *"Stresses and Recoverable Strains of Stretched Polymer Melts and their Prediction by Means of a Simple Integral Consitutive equations"*, Rheology, Vol. A: Fluids, (Eds. G. Astarita, G. Marrucci, L. Nicolais), Plenum Press, New York, 419 (1980).

[49] Laun, H.M. and R. Hingmann, *"Rheological Characterization of the Fluid M1 and of its Components"*, J. Non-Newt. Fluid Mech., **35**, 137-157 (1990).

[50] Leslie, F.M., *"The Slow Flow of a Viscoelastic Liquid past a Sphere"*, Q. J. Mech. Appl. Math., **14**, 36-48 (1961).

[51] Lodge, A.S., *"Elastic Liquids"*, Academic Press, New York (1964).

[52] Lodge, A.S., *"Body Tensor Fields in Continuum Mechanics"*, Academic Press, New York (1974).

[53] Luo, X.-L., *"Finite Streamline Element Simulation of Non - Newtonian Flow"*, Ph.D. Thesis, University of Sydney, Australia (1987).

[54] Luo, X.-L. and E. Mitsoulis, *"An Efficient Algorithm for Strain History Tracking in Finite Element Computations of Non-Newtonian Fluids with Integral Constitutive Equations"*, Int. J. Num. Meth. Fluids, **25**, 1015-1031 (1990).

[55] Luo, X.-L. and E. Mitsoulis, *"A Numerical Study of the Effect of Elongational Viscosity on Vortex Growth in Contraction Flows of Polyethylene Melts"*, J. Rheol., **34**, 309-342 (1990).

[56] Luo, X.-L. and E. Mitsoulis, *"Memory Phenomena in Extrudate Swell Simulations from Annular Dies"*, J. Rheol., **33**, 1307-1327 (1989).

[57] Luo, X.-L. and R.I. Tanner, *"Finite Element Simulation of Long and Short Circular Die Extrusion Experiments Using Integral Models"*, Int. J. Num. Meth. Eng., **25**, 9-22 (1988).

[58] Luo, X.-L. and R.I. Tanner, *"A Decoupled Finite Element Streamline - Upwind Scheme for Viscoelastic Flow Problems"*, J. Non-Newt. Fluid Mech., **31**, 143-162 (1989).

[59] Luo, X.-L. and R.I. Tanner, *"A Streamline Element Scheme for Solving Viscoelastic Flow Problems. Part I. Differential Constitutive Equations"*, J. Non-Newt. Fluid Mech., **21**, 179-199 (1986).

[60] Luo, X.-L. and R.I. Tanner, *"A Streamline Element Scheme for Solving Viscoelastic Flow Problems. Part II. Integral Constitutive Models"*, J. Non-Newt. Fluid Mech., **22**, 61-89 (1986).

[61] Manero, O. and B. Mena, *"On the Slow Flow of Viscoelastic Liquids past a Circular Cylinder"*, J. Non-Newt. Fluid Mech., **9**, 379-387 (1981).

[62] Mena, B., O. Manero and L.G. Leal, *"The Influence of Rheological Properties on the Slow Flow past Spheres"*, J. Non-Newt. Fluid Mech., **26**, 247-275 (1987).

[63] Mitsoulis E., *"Numerical Simulation of Viscoelastic Fluids"*, in Encyclopedia of Fluid Mechanics, Vol.**9**, Polymer Flow Engineering (Ed. N.P. Cheremisinoff), Gulf Publ. Co., Houston, 649-704 (1990).

[64] Münstedt H., *"The Elongational Behaviour of Various Polymer Melts"*, Rheology, Vol. A: Fluids, (Eds. G. Astarita, G. Marrucci, L. Nicolais). Plenum Press, New York, 413 (1980).

[65] Nguyen, D.A. and T. Sridhar, *"Preparation and Some Properties of Fluid M1 and its Constituents"*, J. Non-Newt. Fluid Mech., **35**, 93-104 (1990).

[66] Oden, J.T., *"Finite Elements for Non-Linear Continua"*, McGraw-Hill, New York (1972).

[67] Orbey, N. and J.M Dealy, *"Isothermal Swell of Extrudate from Annular Dies; Effects of Die Geometry, Flow Rate, and Resin Characteristics"*, Polym. Eng. Sci., **24**, 511-518 (1984).

[68] Papanastasiou, A.C., L.E. Scriven and C.W. Macosko, *"An Integral Constitutive Equation for Mixed Flows: Viscoelastic Characterization"*, J. Rheol., **27**, 387-410 (1983).

[69] Papanastasiou, A., *"Coating Flows and Processing of Viscoelastic Liquids: Fluid Mechanics, Rheology and Computer-Aided Analysis"*, Ph.D. Thesis, University of Minnesota, MN (1984).

[70] Park, H.J. and E. Mitsoulis, *"Numerical Simulation of Circular Entry Flows of Fluid M1 Using an Integral Constitutive Equation"*, J. Non-Newt. Fluid Mech., **42**, 301-314 (1992).

[71] Phan-Thien, N. and R. I. Tanner, *"A New Constitutive Equation Derived From Network Theory"*, J. Non-Newt. Fluid Mech., **2**, 353-365 (1977).

[72] Phan-Thien, N., R. Zheng and R.I. Tanner, *"Flow along the Centerline behind a Sphere in a Uniform Stream"*, J. Non-Newt. Fluid Mech., **41**, 151-170 (1991).

[73] Sigli, D. and M. Coutanceau, *"Effect of Finite Boundaries on the Flow of Laminar Isothermal Flow of a Viscoelastic Fluid around a Spherical Obstacle"*, J. Non-Newt. Fluid Mech., **2**, 1-21 (1977).

[74] Silliman, W.J. and L.E. Scriven, *"Separating Flow Near a Static Contact Line"*, J. Comp. Phys., **34**, 287-298 (1980).

[75] Sridhar, T., R.K. Gupta, D.V. Boger and R.J. Binnington, *"Steady Spinning of the Oldroyd-B Fluid: II. Experimental Results"*, J. Non-Newt. Fluid Mech., **21**, 115-126 (1986).

[76] Stokes, C.G., Trans. Cambridge Phil. Soc., **9**, 8 (1850).

[77] Sugeng, F. and R.I. Tanner, *"The Drag on Spheres in Viscoelastic Fluids with Significant Wall Effects"*, J. Non-Newt. Fluid Mech., **20**, 281-292 (1986).

[78] Tanner, R.I., *"Engineering Rheology"*, Oxford University Press, Oxford (1988).

[79] Tanner, R.I., *"Upper and Lower Bounds for Inelastic Flows Using BEM and FEM"*, J. Non-Newt. Fluid Mech., **38**, 101-106 (1990).

[80] Tanner R.I., *"Theoretical and Applied Rheology"*, Vol. 1, Proceedings of the XI th International Congress on Rheology, Brussels, Belgium, August 17-21, 1991 (Eds. P. Moldenaers and R. Keunings), Elsevier, Amsterdam (1991).

[81] Tiefenbruck, G. and L.G. Leal, *" A Numerical Study of the Motion of a Viscoelastic Fluid past Rigid Spheres and Spherical Bubbles"*, J. Non-Newt. Fluid Mech., **10**, 115-155 (1982).

[82] Tirtaatmadja V., P.H.T. Uhlherr and T. Sridhar,*"Creeping Motion of Spheres in Fluid M1"*, J. Non-Newt. Fluid Mech., **35**, 327-337 (1990).

[83] Vlachopoulos, J., *"Should You Use Finite Difference or Finite Element Method"*, Proc. 35th ANTEC, Soc. Plast. Eng., Montreal, Quebec, **23**, 519-520 (1977).

[84] Walters, K., *"Rheometry: Industrial Applications"*, Wiley, New York (1980).

[85] Wesson, R.D. and A.C. Papanastasiou, *"Flow Singularities and Slip Velocity in Plane Extrudate Swell Computations"*, J. Non-Newt. Fluid Mech., **26**, 277-295 (1988).

[86] Zheng, R., N. Phan-Thien and R.I. Tanner, *"The Flow past a Sphere in a Cylindrical Tube: Effects of Inertia, Shear-Thinning and Elasticity"*, J. Non-Newt. Fluid Mech., **30**, 499-510 (1991).

[87] Zheng, R., N. Phan-Thien and R.I. Tanner, *"On the Flow Past a Sphere in a Cylindrical Tube: Limiting Weissenberg Number"*, J. Non-Newt. Fluid Mech., **36**, 27-49 (1990).

[88] Zienkiewicz, O.C. *"The Finite Element Method in Engineering Science"*, 3rd ed., McGraw-Hill, London (1980).

Appendix A

Derivation of the Maxwell Model in Simple Shear Flows

In order to derive the expression for the Cauchy-Green tensor and its inverse, the Finger strain tensor, it is ideal to describe the location of a particle in an Eulerian frame of reference.

Consider a fluid particle whose position at the present time t is given by $\bar{x}(t)$ (see Figure A1). The fluid motion is described by the vector relation

$$\bar{x}(t') = \bar{\chi}\left(\bar{x}(t), t, t'\right) \tag{A.1}$$

Equation (A.1) gives the particle position $\bar{x}(t')$ at historical time t' ranging between $-\infty$ and t. The relative deformation gradient $\bar{\bar{F}}_t(t)$ and the Cauchy-Green strain tensor $\bar{\bar{C}}_t$ are given by

$$\bar{\bar{F}}_t(t') = \frac{\partial \bar{\chi}}{\partial \bar{x}} \tag{A.2}$$

$$\bar{\bar{C}}_t(t') = \bar{\bar{F}}_t^T(t').\bar{\bar{F}}_t(t') \tag{A.3}$$

In these definitions, the deformations are measured relative to the fluid configuration at present time t.

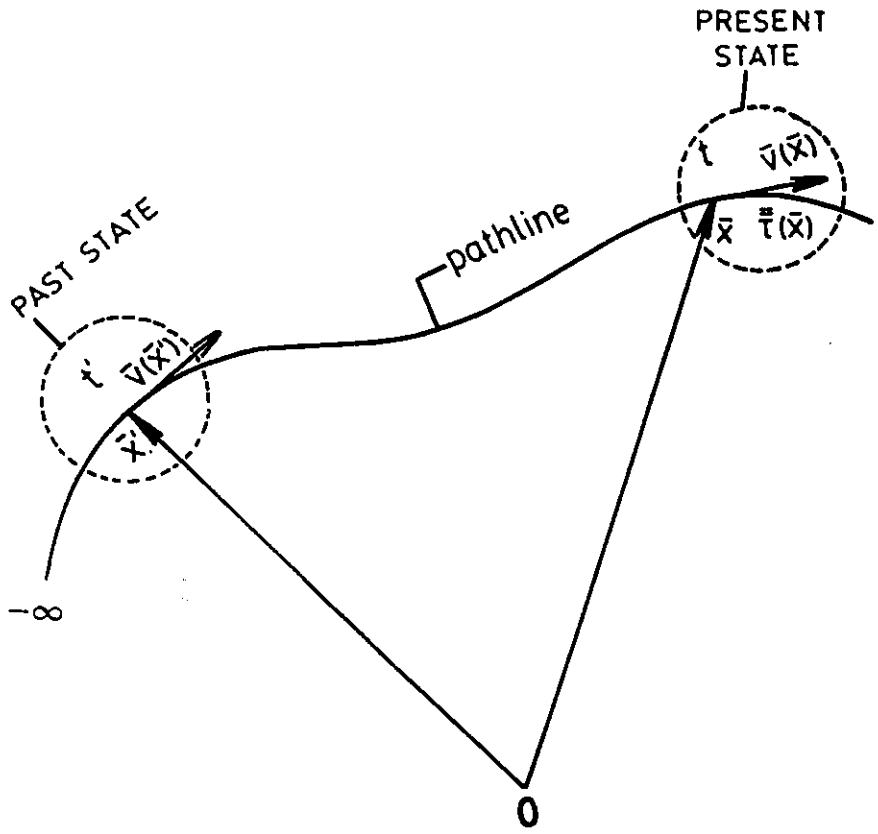

Figure A.1: The fluid *particle* that is presently at $\bar{x}$ occupied all positions $\bar{x}'$ along its pathline at earlier times t'. All past states are deformed relative to the present state.

For simple shear flow (axisymmetric case),

$$v_r = \frac{dr}{dt'} = 0 \tag{A.4}$$

$$v_\theta = \frac{d\theta}{dt'} = 0 \tag{A.5}$$

$$v_z = \frac{dz}{dt'} \tag{A.6}$$

The following initial conditions are assumed at $t' = t$

$$r = r_t \tag{A.7}$$

$$\theta = \theta_t \tag{A.8}$$

$$z = z_t \tag{A.9}$$

$$\dot{\gamma} = \frac{dv_z}{dr} \tag{A.10}$$

$$v_z = \dot{\gamma} r_t \tag{A.11}$$

$$\frac{dz}{dt'} = \dot{\gamma} r_t \tag{A.12}$$

Integrating Equations (A.4-A.6)

$$r = r_t \tag{A.13}$$

$$\theta = \theta_t \tag{A.14}$$

$$\int_{z_t}^{z} dz = \int_{t}^{t'} \dot{\gamma} r_t dt' \tag{A.15}$$

$$\begin{aligned} z - z_t &= \dot{\gamma} r_t (t' - t) \\ z &= z_t + \dot{\gamma} r_t (t' - t) \end{aligned} \tag{A.16}$$

The deformation tensor $\bar{\bar{F}}_t(t')$ can be written as follows:

$$\bar{\bar{F}}_t(t') = \begin{pmatrix} \frac{\partial r}{\partial r_t} & \frac{\partial r}{\partial \theta_t} & \frac{\partial r}{\partial z_t} \\ \frac{\partial \theta}{\partial r_t} & \frac{\partial \theta}{\partial \theta_t} & \frac{\partial \theta}{\partial z_t} \\ \frac{\partial z}{\partial r_t} & \frac{\partial z}{\partial \theta_t} & \frac{\partial z}{\partial z_t} \end{pmatrix} \tag{A.17}$$

Evaluating the derivatives, the matrix becomes

$$\bar{\bar{F}}_t(t') = \begin{pmatrix} 1 & 0 & 0 \\ 0 & 1 & 0 \\ -s\dot{\gamma} & 0 & 1 \end{pmatrix} \tag{A.18}$$

Using the relationship given by Equation (A.3), $\bar{\bar{C}}_t(t')$ becomes

$$\bar{\bar{C}}_t(t') = \begin{pmatrix} 1+(s\dot{\gamma})^2 & 0 & -s\dot{\gamma} \\ 0 & 1 & 0 \\ -s\dot{\gamma} & 0 & 1 \end{pmatrix} \tag{A.19}$$

The inverse of the Cauchy-Green tensor $\bar{\bar{C}}_t^{-1}(t')$, which is called the Finger strain tensor, is given by

$$\bar{\bar{C}}_t^{-1}(t') = \frac{1}{det\bar{\bar{C}}_t(t')} Adj\ \bar{\bar{C}}_t(t') \tag{A.20}$$

The determinant of the Cauchy-Green tensor, $det\ \bar{\bar{C}}_t(t')$, is unity. Evaluating the adjoint of the Cauchy-Green tensor and substituting into Equation (A.20) yields

$$\bar{\bar{C}}_t^{-1}(t') = \begin{pmatrix} 1 & 0 & -s\dot{\gamma} \\ 0 & 1 & 0 \\ -s\dot{\gamma} & 0 & 1+(s\dot{\gamma})^2 \end{pmatrix} \tag{A.21}$$

The identity matrix, $\bar{\bar{I}}$ is given by

$$\bar{\bar{I}}_t(t') = \begin{pmatrix} 1 & 0 & 0 \\ 0 & 1 & 0 \\ 0 & 0 & 1 \end{pmatrix} \tag{A.22}$$

since $s = t - t'$,

$$dt' = -ds$$

Thus, inserting $\bar{\bar{C}}_t(t')$, $\bar{\bar{C}}_t^{-1}(t')$, $\bar{\bar{I}}$ and dt' in the Maxwell model Equation (2.8) and changing the limits of integration, the following expressions are obtained:

$$\tau_{rr} = \left(\frac{\theta}{1-\theta}\right)\frac{\mu}{\lambda^2}\int_0^\infty s^2 e^{-s/\lambda}\, ds \tag{A.23}$$

$$\tau_{zz} = \left(\frac{1}{1-\theta}\right)\frac{\mu}{\lambda^2}\int_0^\infty s^2 e^{-s/\lambda}\, ds \tag{A.24}$$

$$\tau_{rz} = \tau_{zr} = \frac{\mu\dot{\gamma}}{\lambda}\int_0^\infty s e^{-s/\lambda}\, ds \tag{A.25}$$

and

$$\tau_{r\theta} = \tau_{\theta r} = \tau_{\theta z} = \tau_{z\theta} = \tau_{\theta\theta} = 0 \tag{A.26}$$

The above expressions for τ_{rr}, τ_{zz} and τ_{rz} are easily integrated using the method of integration by parts and in doing so the following expressions are

obtained:

$$\tau_{rr} = 2\left(\frac{\theta}{1-\theta}\right)\mu\lambda\dot{\gamma}^2 \tag{A.27}$$

$$\tau_{zz} = 2\left(\frac{1}{1-\theta}\right)\mu\lambda\dot{\gamma}^2 \tag{A.28}$$

$$\tau_{rz} = \tau_{zr} = \mu\dot{\gamma} \tag{A.29}$$

Appendix B

Calculation of the Drag Coefficient (K)

To obtain the analytical expression for the drag D_∞ (Equation 4.2), one has to obtain the expressions for the pressure and shear stress distributions at the surface of the sphere. These expressions are then integrated over the sphere surface to obtain Equation (4.2) by neglecting gravity forces (see Bird et al., 1960).

For our numerical calculations of the drag force, the normal and tangential components of the total force acting on a sphere were considered separately. Let us consider the very slow flow of an incompressible fluid about a solid sphere, as shown in Figure B.1. The drag force F_D was evaluated numerically by integrating the tractions over the sphere surface as follows:

For the normal force (F_N), the pressure force normal to the surface has a component in the flow direction, which is given by

$$-P\ cos\beta \qquad (B.1a)$$

In addition, there is a normal force (τ_{rr}) in the radial direction due to the fluid motion. This force contributes to the drag force through its component in the

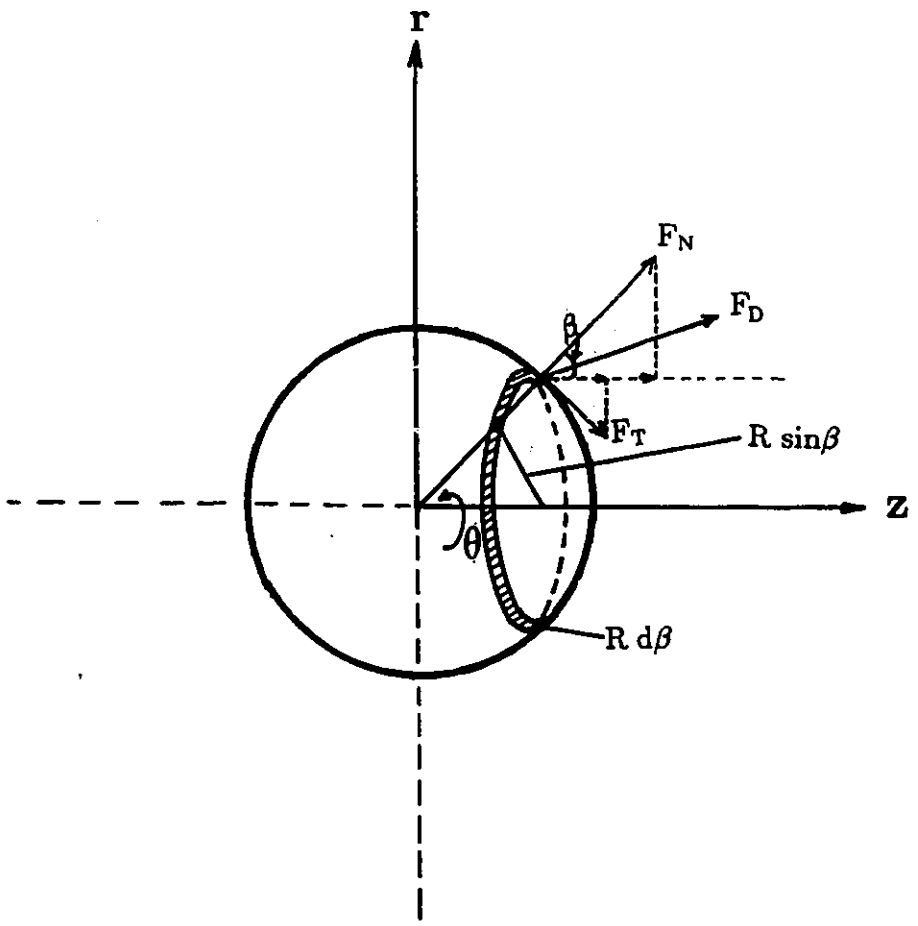

Figure B.1: Coordinate system used in describing the flow of a fluid around a rigid sphere.

flow direction. This component force is given by

$$-\tau_{rr}\ cos\beta \qquad (B.1b)$$

Equations (B.1a and b) constitute the normal force, F_N, which can be expressed as

$$dF_N = -\left[(P + \tau_{rr})cos\beta\right]\ dS \qquad (B.1c)$$

In spherical coordinates, the element dS may be taken as the area of the elementary ring the plane of which is normal to the axis of symmetry, *i.e.* $dS = 2\pi R^2 sin\beta\ d\beta$ (Curle and Davies, 1968). Thus, Equation (B.1c) can be written as

$$F_N = 2\pi \int_0^{\pi} -\left[(P + \tau_{rr})cos\beta\right] R^2 sin\beta\ d\beta \qquad (B.1d)$$

In cylindrical coordinates, $z = Rcos\beta$ and $dz = -Rsin\beta\ d\beta$, and substituting for $d\beta$ in Equation (B.1d) and changing the limits of integration, Equation (B.1d) becomes

$$F_N = -2\pi \int_{-1}^{1} \left[P + \tau_{rr}\right]\ z dz \qquad (B.1e)$$

The tangential force (F_T) can be evaluated by resolving the shear stress component (τ_{rz}) in the direction of flow

$$dF_T = \tau_{rz} sin\beta\ dS \qquad (B.2a)$$

which by following a similar analysis gives

$$F_T = 2\pi \int_0^{\pi} \tau_{rz} sin\beta R^2 sin\beta\ d\beta \qquad (B.2b)$$

Substituting for $d\beta$ and changing the limits of integration Equation (B.2b) becomes

$$F_T = -2\pi \int_{-1}^{1} \tau_{rz} R sin\beta \; dz \qquad (B.2c)$$

Combining Equations (B.1e) and (B.2c), the total drag force F_D becomes

$$F_D = -2\pi \int_{-1}^{1} [(P + \tau_{rr})z + (\tau_{rz} R sin\beta)] \; dz \qquad (B.3)$$

The values of P, τ_{rr}, τ_{rz} and the coordinates z, $Rsin\beta$ were readily available from the NACHOS program. Equation (B.3) was thus integrated numerically using the trapezoidal rule.